



LAWRENCE  
LIVERMORE  
NATIONAL  
LABORATORY

LLNL-TH-408879

# Spectroscopic Investigations of Highly Charged Ions using X-Ray Calorimeter Spectrometers

D. B. Thorn

November 19, 2008

## **Disclaimer**

---

This document was prepared as an account of work sponsored by an agency of the United States government. Neither the United States government nor Lawrence Livermore National Security, LLC, nor any of their employees makes any warranty, expressed or implied, or assumes any legal liability or responsibility for the accuracy, completeness, or usefulness of any information, apparatus, product, or process disclosed, or represents that its use would not infringe privately owned rights. Reference herein to any specific commercial product, process, or service by trade name, trademark, manufacturer, or otherwise does not necessarily constitute or imply its endorsement, recommendation, or favoring by the United States government or Lawrence Livermore National Security, LLC. The views and opinions of authors expressed herein do not necessarily state or reflect those of the United States government or Lawrence Livermore National Security, LLC, and shall not be used for advertising or product endorsement purposes.

This work performed under the auspices of the U.S. Department of Energy by Lawrence Livermore National Laboratory under Contract DE-AC52-07NA27344.

Spectroscopic Investigations of Highly Charged Ions using X-Ray Calorimeter  
Spectrometers

by

DANIEL BRISTOL THORN  
B.A. (University of California at Berkeley) 2003

DISSERTATION

Submitted in partial satisfaction of the requirements for the degree of

DOCTOR OF PHILOSOPHY

in

Applied Science

in the

OFFICE OF GRADUATE STUDIES

of the

UNIVERSITY OF CALIFORNIA

DAVIS

Approved:

---

---

---

Committee in Charge

2008

**Spectroscopic Investigations of Highly Charged Ions using X-Ray  
Calorimeter Spectrometers**

Copyright 2008

by

Daniel Bristol Thorn

Daniel Bristol Thorn

December 2008

Applied Science

Spectroscopic Investigations of Highly Charged Ions using X-Ray Calorimeter  
Spectrometers

**Abstract**

Spectroscopy of K-shell transitions in highly charged heavy ions, like hydrogenlike uranium, has the potential to yield information about quantum electrodynamics (QED) in extremely strong nuclear fields as well as tests of the standard model, specifically parity violation in atomic systems. These measurements would represent the ‘holy grail’ in high-Z atomic spectroscopy. However, the current state-of-the-art detection schemes used for recording the K-shell spectra from highly charged heavy ions does not yet have the resolving power to be able to attain this goal. As such, to push the field of high-Z spectroscopy forward, new detectors must be found.

Recently, x-ray calorimeter spectrometers have been developed that promise to make such measurements. In an effort to make the first steps towards attaining the ‘holy grail’, measurements have been performed with two x-ray calorimeter spectrometers (the XRS/EBIT and the ECS) designed and built at Goddard Space Flight Center in Greenbelt, MD. The calorimeter spectrometers have been used to record the K-shell spectra of highly charged ions produced in the SuperEBIT electron beam ion trap at Lawrence Livermore National Laboratory in Livermore, CA.

Measurements performed with the XRS/EBIT calorimeter array found that the theoretical description of well-above threshold electron-impact excitation cross sections for hydrogenlike iron and nickel ions are correct. Furthermore, the first high-resolution spectrum of hydrogenlike through carbonlike praseodymium ions was recorded with a calorimeter. In addition, the new high-energy array on the EBIT Calorimeter Spectrometer (ECS) was used to resolve the K-shell x-ray emission spectrum of highly charged xenon ions, where a 40 ppm measurement of the energy of the K-shell resonance transition in heliumlike xenon was achieved. This is the highest precision result, ever, for an element with such high atomic number. In addition, a first-of-its-kind measurement of the effect of the generalized Breit interaction (GBI) on electron-impact excitation cross sections was performed. This measurement found that for theoretical electron-impact excitation cross sections to fit with experimental data the GBI needs to be taken into account.

To my mother who has guided me, nurtured me, and given me the support to be able to live and be free. Without her I would not have made it this far. This is for you...

# Contents

<b>List of Figures</b>	<b>ix</b>
<b>List of Tables</b>	<b>xi</b>
<b>I Introductory Material</b>	<b>1</b>
<b>1 Introduction</b>	<b>2</b>
<b>2 Electron-Ion Collisions</b>	<b>8</b>
2.1 Electron Beam Ion Traps . . . . .	8
2.2 Photon Emission in SuperEBIT . . . . .	9
2.2.1 Polarization of X rays from EBIT . . . . .	14
2.3 Modification of EIE Cross Section Due to QED . . . . .	16
2.4 Summary . . . . .	20
<b>3 X ray Calorimeter Spectrometers</b>	<b>21</b>
3.1 Basics . . . . .	21
3.1.1 Energy Resolution . . . . .	22
3.1.2 Thermalization . . . . .	24
3.2 NASA/GSFC Type Thermistor Detectors . . . . .	25
3.2.1 Thermistor Circuit . . . . .	25
3.2.2 Thermistor Design . . . . .	28
3.2.3 Pulse Height Determination . . . . .	29
3.3 XRS/EBIT x-ray spectrometer . . . . .	34
3.4 Stacked pixel and Resolution studies . . . . .	39
3.4.1 Resolution Study . . . . .	39
3.5 Test of a High Quantum Efficiency Calorimeter Spectrometer . . . . .	44
3.6 ECS . . . . .	47
3.6.1 Design . . . . .	48
3.7 Quantum Efficiency . . . . .	51



<b>II</b>	<b>Measurements</b>	<b>58</b>
<b>4</b>	<b>Measurement of Electron-Impact Excitation Cross Sections at High Electron Impact Energies for Hydrogenlike Iron and Nickel Ions</b>	<b>59</b>
4.1	Introduction . . . . .	59
4.2	Experiment . . . . .	61
4.3	Conclusion . . . . .	65
<b>5</b>	<b>The First Results of High-Z K-shell Spectra Recorded with Calorimeters</b>	<b>66</b>
5.1	Praseodymium with Bismuth Absorbers . . . . .	66
5.1.1	Transition Energies . . . . .	71
5.1.2	Discussion . . . . .	73
5.2	Praseodymium with Thin HgTe pixels . . . . .	73
5.2.1	Measurement of K-shell Spectra from High-Z Highly Charged Ions .	75
5.2.2	Experiment . . . . .	76
5.2.3	Transition Energies . . . . .	77
5.3	Summary and Conclusion . . . . .	79
<b>6</b>	<b>Transition Energy Measurement of Hydrogenlike and Heliumlike Xenon with the ECS</b>	<b>82</b>
6.1	Introduction . . . . .	82
6.2	Experiment . . . . .	83
6.3	Calibration . . . . .	84
6.4	Power shift . . . . .	89
6.5	Transition Energies of Hydrogenlike Xenon . . . . .	96
6.6	Transition Energies of Heliumlike Xenon . . . . .	96
6.7	Transition Energies from Lower Charge States . . . . .	101
6.8	Summary . . . . .	102
<b>7</b>	<b>Generalized Breit Interaction and Absolute K-shell Electron-Impact Excitation Cross Sections in Highly Charged Xenon Ions</b>	<b>103</b>
7.1	Test of the Generalized Breit Interaction with Highly Charged Xenon Ions .	105
7.1.1	Introduction . . . . .	105
7.1.2	Experiment . . . . .	106
7.1.3	Measurement . . . . .	108
7.1.4	Conclusion . . . . .	115
7.2	Absolute Electron-Impact Cross Sections of K-shell Transitions in Highly Charged Xenon Ions . . . . .	115
7.2.1	Introduction . . . . .	115
7.2.2	Measurement . . . . .	116
7.2.3	Discussion . . . . .	123
7.3	Conclusion . . . . .	125
<b>8</b>	<b>Summary and Future Work</b>	<b>127</b>
	<b>Bibliography</b>	<b>130</b>

A List of K-shell Transitions from Highly Charged Ions Used in this Thesis	143
B QED and Feynman Calculus	145

# List of Figures

2.1	Schematic for the direct excitation process . . . . .	11
2.2	Schematic for the direct excitation with cascades process . . . . .	12
2.3	Schematic for the radiative recombination (RR) process . . . . .	13
3.1	Schematic of a basic calorimeter. . . . .	22
3.2	Basic schematic of thermistor circuit . . . . .	26
3.3	Picture of XRS/EBIT array in detector assembly. . . . .	35
3.4	Picture of XRS/EBIT style pixel . . . . .	36
3.5	Spectrum of $^{241}\text{Am}$ recorded with '4 stacked' pixel . . . . .	40
3.6	Calculated pulse height response for 8 $\mu\text{m}$ thick and 50 $\mu\text{m}$ thick HgTe absorbers	42
3.7	Prediction of resolution attainable with different thickness of HgTe absorbers at 60 mK detector temperature . . . . .	43
3.8	Magnified picture of test array . . . . .	46
3.9	Picture of finished ECS array . . . . .	49
3.10	Magnified picture of finished ECS array . . . . .	52
3.11	Plot of Quantum Efficiency for Photons from 10 keV to 150 keV . . . . .	55
3.12	Plot of Quantum Efficiency for 114 $\mu\text{m}$ of HgTe for photons from 20 keV to 145 keV . . . . .	57
4.1	Spectrum recorded with the IGLET for nickel at an electron beam energy of 85 keV . . . . .	62
4.2	K-shell spectrum of nickel at an electron beam energy of 85 keV . . . . .	62
4.3	Experimental electron-impact excitation cross sections for the Lyman- $\alpha_1$ line in hydrogenlike iron and nickel . . . . .	64
5.1	The quantum efficiency of a 30 $\mu\text{m}$ bismuth absorber . . . . .	68
5.2	K-shell spectrum of highly charged Pr ions obtained with the IGLET-X de- tector. . . . .	69
5.3	The first high-resolution spectrum of heliumlike through berylliumlike praseodymium . . . . .	70
5.4	Quantum microcalorimeter spectrum of hydrogenlike through carbonlike praseodymium taken at an electron beam energy of 127 keV . . . . .	78

6.1	Quantum microcalorimeter spectrum of hydrogenlike through boronlike xenon taken at an electron beam energy of 114 keV . . . . .	85
6.2	ECS spectrum of $^{133}\text{Ba}$ and $^{241}\text{Am}$ over 9 days . . . . .	87
6.3	Time resolved spectrum from the ECS . . . . .	88
6.4	The shift in centroid of the calibration peaks for the low and high count rate settings . . . . .	91
6.5	The power shift coefficient of the Cs $K\alpha$ calibration lines as function of power . . . . .	93
6.6	The FWHM resolution of the ECS as a function of incident power . . . . .	94
6.7	The power shift coefficient of the Cs $K\alpha$ calibration lines as a function of power for powers under 9 keV/sec/pixel . . . . .	95
6.8	The difference in the experimental transition energy and the theoretical transition energy is plotted for each transition . . . . .	100
7.1	Spectrum of xenon taken with the ECS at an electron beam energy of 39 keV . . . . .	107
7.2	K-shell spectrum of xenon taken with the ECS at an electron beam energy of 39 keV . . . . .	108
7.3	Microcalorimeter spectrum of L-shell RR radiation taken at an electron beam energy of 39 keV. . . . .	110
7.4	Plot of Quantum Efficiency for the ECS vs photon energy . . . . .	118
7.5	Plot of the experimental and theoretical values of EIE cross sections for K-shell transitions in heliumlike through berylliumlike xenon . . . . .	125
B.1	Feynman diagram for the scattering process of two free electrons . . . . .	146

# List of Tables

3.1	Table of measured FWHM energy resolutions on the test detector. . . . .	47
4.1	Experimental cross sections for electron-impact-excitation of the Lyman- $\alpha_1$ line in hydrogenlike iron and nickel ions . . . . .	65
5.1	Measured transition energies of heliumlike through lithiumlike praseodymium	72
5.2	Table of measured transition energies for K-shell praseodymium at an electron beam energy of 127 keV . . . . .	81
6.1	List of lines used in the determination of the energy scale . . . . .	89
6.2	Experimental and theoretical K-shell transition energies for hydrogenlike xenon.	97
6.3	Experimental and theoretical transition energies of heliumlike xenon. . . . .	99
6.4	Experimental and theoretical transition energy values for select lithiumlike and berylliumlike spectral lines. . . . .	101
7.1	Calculated atomic data for selected K-shell spectral lines for heliumlike thorough berylliumlike xenon at an electron beam energy of 39 keV . . . . .	111
7.2	Total and differential cross sections calculated for heliumlike through carbonlike xenon . . . . .	112
7.3	Charge balance of xenon ions in SuperEBIT at an electron beam energy of 39 keV. . . . .	113
7.4	Table of measured and predicted ratio of intensities of selected transitions in heliumlike and lithiumlike xenon . . . . .	114
7.5	Measured and calculated electron impact-excitation cross sections, in units of barn, for the resonance and intercombination transitions in heliumlike xenon at a beam energy of 39 keV. . . . .	120
7.6	Cross-section ratio for heliumlike charge states w and y. Ratio is based on experimentally determined cross sections. The uncertainty of 0.06 is the quadrature sum of the statistical error and the uncertainty from removing the contribution of line r from the blend with line y. . . . .	121
7.7	Measured and calculated electron impact-excitation cross section, in units of barn, for the forbidden transition in heliumlike xenon at a beam energy of 39 keV. . . . .	122

7.8	Measured and calculated electron impact-excitation cross section, in units of barn, for the resonance transition in lithiumlike xenon at a beam energy of 39 keV. . . . .	123
7.9	Measured and calculated electron impact-excitation cross sections, in units of barn, for the resonance and intercombination transition in berylliumlike xenon at a beam energy of 39 keV. . . . .	124
A.1	List of transition used in this dissertation. . . . .	144

## Acknowledgments

I first and foremost want to thank Peter Beiersdorfer for all the support he has given me for the past eight years. Without his guidance, advocacy, patience and command of the English language, I would not have the opportunity to write this dissertation. He has been a friend and mentor and I am truly grateful for everything he has done for me. I also want to thank Ann Orel, my advisor at UC Davis, for her continued moral, educational and financial support of my work at LLNL, especially when the lab was privatized and I was denied the ability to have health insurance.

I had the unwavering support of my family who were always amazed that I was able to keep my life together and continue working towards my goal and I want to thank them for that. My mother has been the single most important piece in my life and without her I would not have made it. I also want to thank Mark for his many years of putting up with me and showing me the way towards logical reasoning and for talking actively about politics and the world. I also want to thank my father for giving me his wonderment of science and his mechanical skills. And my grandmother who has always been behind me, and given me a sense of history. My good friends Steve and Beth Curtis, as well as John Conrad, have been instrumental in helping me unwind and feeding me beer and food, which are necessary things to finishing a dissertation! I also want to thank my future wife Alexandra for keeping me focused and for giving me love and support.

Michael Conner, who was my freshman physics professor at DVC, first recommended that I go to LLNL in the summer of 2000 and started me on this journey and I thank him for that. I also want to thank various scientists at the EBIT facility, Keith Wong,

Steve Utter, Klaus Widmann, Hui Chen, and Mark May, who took me under their wings when I was a raw teenager and laid the foundation of my physics knowlege. Greg Brown, who was a PhD student when I first arrived, taught me the most. I value his friendship and his guidance and I am very thankful for his support and patience with me as I was bouncing ideas off him.

I also want to thank the wonderful people at Goddard Space Flight Center, Rich Kelley, Caroline Kilbourne, F. Scott Porter, John Gygax, and Jonathan King. Without them none of this would be possible.

Ed Magee and Phil Dantonio were instrumental in maintaining and keeping EBIT running. Without their help and support I would not have been able to do the measurements in this thesis. Ed in particular was instrumental in machining many pieces for me and his expert skills made my life much easier. Phil, provided amazing computer and electrical support and could always be counted on to be one step ahead. It was a great pleasure to work with them both!

I also want to thank the ‘Viking Contingent’ Joel Clementson and Miriam Frankel for whom sharing an office was fun. Also, Mike Schimdt for his 1 year he spent here, and the continued friendship we have together as well as being instrumental in me meeting my future wife.

I certainly need to thank my lunchtime crew, Dan Hey, Prav Patel, Sebastien LePape, Andrew McPhee, Sophia Chen, Cliff Chen, and Tammy Ma for the fun I’ve had over the years. I want to thank Dan Hey for providing me with calculations and the friendship we’ve had since we were both in Micheael Conner’s class.



This work was performed under the auspices of the U. S. Department of Energy by Lawrence Livermore National Laboratory under Contract DE-C52-07NA27344 and was supported by NASA grants to LLNL and GSFC.

## Part I

# Introductory Material

# Chapter 1

## Introduction

The advent of the century of physics (the 20th century) has been inexorably linked to atomic spectroscopy. Around the turn of the century (1900) Planck investigated black-body radiation, and found that its spectrum could be described by assuming that the radiation was quantized. Bohr and Rutherford gave us the picture of the nuclear atom we think of today, and the work of Schrödinger, Bohr, Pauli, Heisenberg and Dirac helped to shape our theoretical understanding of atomic spectra. With these discoveries the theory of quantum mechanics was born and ushered in a new area of understanding the physical world around us. However, quantum mechanics, and thus this new age, would not have been, if not for experimental advances in the precision of atomic spectroscopy, as it was theoretical fits to experimental data that helped to fuel the quantum mechanical revolution<sup>1</sup>

With the advent of the formalism of quantum electrodynamics (QED), which won Feynman, Schwinger and Tomonaga the 1965 Nobel Prize in Physics, much work went into

---

<sup>1</sup>For more information please look in any introductory Quantum Mechanics text book. My favorite is “Quantum Mechanics (2nd Edition)” by B.H. Bransden and C.J. Joachain.

measuring QED effects where ever they could be found. The best known of these are the 2s-2p lamb shift in hydrogen [1, 2] and the value of the g-factor for the electron [3]. The g-factor measurement, in particular, has verified QED to levels of parts per trillion. QED is a perturbative radiative correction theory<sup>2</sup> that depends on the strength of the electric field that the particle is in. As the strength of the electric field increases, so do higher order QED effects. The average value of the electric field in atoms that 1s electrons ‘see’ is steeply dependent on the atomic number Z. For hydrogen, the value is roughly  $10^9$  V/cm, for uranium that value exceeds  $10^{15}$  V/cm.

Because of this steep Z dependance on the electric field, the magnitude of the 1s lamb shift scales as  $Z^4$ , whereas the energy of K-shell atomic transitions scale as  $Z^2$ . Thus, spectroscopic investigations of high-Z elements are perfectly suited for testing bound state quantum electrodynamics (QED) in the strong field of a heavy nucleus. Of particular interest are the K-shell transitions of hydrogenlike and heliumlike ions, as they are the simplest systems (thus easiest to calculate), and show the largest QED effects both on energy level shifts as well as changes in electron scattering cross sections.

The first measurements of K-shell transition energies from highly charged ions were performed with low-Z ions like argon and sulfur [4, 5, 6, 7], as the technical aspects of producing highly charged high-Z ions limited the charge state that was achievable. These measurements showed no discrepancy with theories of the time. However, with the advent of high energy accelerator based storage ring facilities like the Bevalac at LBL in Berkeley, CA, GANIL in France, the ESR at GSI in Germany, and the SuperEBIT electron beam ion

---

<sup>2</sup>QED is added in a perturbative way to other theories (like ‘classical’ relativistic quantum mechanics) by including effects associated with the emission and absorption of photons.

trap in Livermore, CA, the world of bare uranium, and thus K-shell spectroscopy of high-Z ions, was opened up.

In low-Z to high-Z hydrogenlike and heliumlike ions, QED shifts to the energy of 1s levels have been studied extensively [8, 9, 10, 11, 12, 13, 4, 5, 6, 7]. These measurements have confirmed that the theoretical treatment of 1st order QED in hydrogenlike and heliumlike ions is correct. However, attention has now shifted towards testing 2nd order QED calculations. In hydrogenlike uranium, if the 2nd order QED shift (‘2-loop lamb shift’) is included in the calculation of the energy levels, the predicted effect to the ground state energy level is roughly 1 eV or 10 ppm [14, 15].

Heliumlike ions, in particular, are stepping stones to developing multi-electron QED theories<sup>3</sup>. In addition, the heliumlike system is a candidate in several proposed atomic parity violation experiments [16, 17, 18]. But unlike with the hydrogenlike case, there exists several different ways in which to calculate the energy levels of the heliumlike system, and thus it is up to experiment to lead the way. Furthermore, the scattering process of a free electron off of a bound K-shell electron is affected by QED, by the so called generalized Breit interaction, which results in changes to the cross section for electron-impact excitation. This effect is more pronounced in multielectron ions.

Since there has only been one measurement that has inferred a value for the ‘2-loop lamb shift’ [19] in the ground state of hydrogenlike uranium from a measurement of lithiumlike uranium, a direct measurement of the K-shell transitions from the 2p level to the 1s level in hydrogenlike uranium with an accuracy of 1 eV or better, would represent the ‘holy grail’ in high-Z spectroscopy. However, the current state-of-the-art for measuring K-shell

---

<sup>3</sup>As to describe 3 electrons the theory used had better work well for the two electron system first

spectra from highly charged ions, employs solid state detectors. Solid state detectors, such as high-purity germanium detectors (HPGe detectors), collect charge that is accumulated when an electron is absorbed. They have a fundamental limit on the full half maximum resolution they can achieve. For germanium detectors the resolving power,  $E/\Delta E$ , for photons from K-shell transitions in high-Z ions is on the order of 100.

In case the of heliumlike ions, the resolving power,  $E/\Delta E$ , of roughly 100 precludes taking into account line blends between the singlet,  $(1s_{1/2}2p_{3/2})_1 \rightarrow (1s_{1/2}^2)_0$ , and triplet,  $(1s_{1/2}2p_{3/2})_2 \rightarrow (1s_{1/2}^2)_0$ , transitions, which can affect the line energies measured as well as make it impossible to measure QED effects to the cross section for electron-impact excitation. Furthermore, in measurements where the goal is the determination of the energy of the Lyman- $\alpha_1$  spectral line in hydrogenlike uranium, the present experimental uncertainty of 4.6 eV [11] is limited by the resolving power,  $E/\Delta E$ , of the Ge detector used. If that resolving power is increased by a factor of five, then, the experimental accuracy will increase to the 1 eV level, which would allow for a direct experimental test of two loop QED calculations. Thus to make progress in increasing the precision of atomic spectroscopy, new detectors need to be developed.

In a new development, quantum microcalorimeters have appeared [20]. Quantum microcalorimeters are devices that measure the energy of x-ray photons by measuring the temperature rise in a material when it has absorbed the energy of a photon. The event-to-event fluctuations that limit the resolution in solid state ionization detectors are not present in calorimeters because they operate in an equilibrium condition where the non-thermal excitations are negligible compared to the signal produced. Originally, they were

developed for x-ray measurements below 10 keV. Although they have been successfully used on rockets [21], in the lab [22] and in orbit [23] to measure the K-shell emission from carbon to iron ions, they did not provide (by far) the resolving power afforded by standard crystal spectrometers in this energy range. However, for K-shell spectroscopy of high-Z ions, which are difficult to produce, the use of crystal spectrometers has been unworkable due to low throughput so that high-purity Ge (HPGe) detectors have been the only option. Quantum microcalorimeters are thought to be superior to HPGe detectors for x rays above 10 keV, as they promise to have a much higher resolving power (a factor of 10 or higher), provided arrays can be built with suitable quantum efficiency (QE).

This dissertation is concerned with measurements of K-shell spectra from highly charged ions in an electron beam ion trap. The measurements presented herein use quantum microcalorimeters to resolve the K-shell spectra of highly charged ions, which leads to measurements of electron-impact excitation as well as transition energies for a variety of elements, charge states, and transitions. The dissertation is structured into two parts. The first part, which includes this introduction (Chapter 1), presents a review of the excitation mechanisms in an electron beam ion trap along with an introduction to the generalized Breit interaction (Chapter 2). Then, an introduction and description of thermistor type calorimeter detectors is presented along with the design and performance of two GSFC built calorimeters (Chapter 3). The second part of the dissertation is concerned with the measurements using the calorimeters described in Chapter 3. First a measurement of the electron-impact excitation cross sections for hydrogenlike iron and nickel is presented (Chapter 4). This measurement uses a calorimeter to resolve the K-shell spectra and a Ge detector

to observe the radiative recombination spectrum. Chapter 5 presents the first measurements of calorimeters designed to measure high-energy x rays. Chapter 6 presents a measurement of the transition energies of the K-shell spectrum of highly charged xenon ions, where a  $\sim 40$  ppm measurement of the singlet line in the heliumlike system, along with a factor of five improvement in the precision of the measurement of the hydrogenlike system is presented. The measurements are compared to theory and are able to distinguish between some of the theories for calculating the transition energies in the two electron system. Finally, Chapter 7 presents a measurement of the generalized Breit interaction and absolute electron-impact excitation cross sections for heliumlike through berylliumlike xenon. This measurement shows that the treatment of the GBI is valid and is important to include in calculations of EIE cross sections.



## Chapter 2

# Electron-Ion Collisions

Electron beam ion traps (EBITs) are used for testing atomic structure [19], electron-ion interaction codes [24], and compiling atomic data for use in the plasma physics community, whether in astrophysics [22, 24] or fusion science [25]. Tests of atomic structure codes are concerned with the position of spectral lines, whereas tests of electron-ion collision codes (cross section measurements) are interested in how probable a particular interaction is and thus how intense a given spectral line is. To understand the measurements in this dissertation, the basics of EBITs and of the spectral line emission processes are needed.

### 2.1 Electron Beam Ion Traps

Electron beam ion traps produce and excite ions through subsequent collisions with energetic electrons [26]. An EBIT is comprised of an electron gun that emits the electrons, a drift tube region with a 3 T magnetic field that compresses the electron beam, and then a collector that collects the electrons. The ions are trapped in the drift tube

region in the radial direction by the electron beam, and in the axial direction by a set of 3 electrodes biased in such a way as to make a potential well.

Ions are introduced into the trap either via a Metal Vacuum Vapor Arc (MeVVA) or a neutral gas/element injection system. If ions are injected into the trap region, they are injected from the collector region and travel down the electron beam until they are trapped by the axial potential of the drift tube region. Neutral gases are injected perpendicular to the beam, and become trapped once they have been ionized by the electron beam. The axial trap is usually on the order of 100-500 V and the radial trapping is on the order of 10 V.

SuperEBIT is the high-energy electron beam ion trap at LLNL [27]. It can produce 200 keV electron beams and was the first trap in the world to produce trapped bare uranium [28]. The spectral line emission from SuperEBIT is viewed perpendicular to the beam direction. This dissertation deals with ions produced trapped and excited by SuperEBIT.

## 2.2 Photon Emission in SuperEBIT

In an EBIT, spectral lines are usually produced when an electron from the electron beam interacts with an ion. The rate,  $R$ , of photon emission emitted from electron-ion interactions per unit volume in an EBIT is,

$$R = n_e n_i v_e \sigma, \tag{2.1}$$

where  $n_e$  is the density of electrons in the beam,  $n_i$  is the density of ions,  $v_e$  is the velocity of the electrons in the beam, and  $\sigma$  is the cross section for the process that makes the spectral

line<sup>1</sup>. The processes for producing K-shell spectral line emission in an EBIT relevant to this dissertation are electron impact excitation, radiative recombination (or radiative electron capture), charge exchange, and innershell ionization.

### Photon Emission by Electron-Impact Excitation

Electron-impact excitation (EIE) is the dominate spectral line emission process in EBITs when the energy of the electron beam is above the EIE threshold. A spectral line is produced by the EIE process when an electron, from the electron beam, inelasticity scatters off a bound electron in an ion and excites the bound electron to a higher lying atomic level, where in turn, the excited electron will radiatively decay back to the ground state. This process is referred to as direct excitation (DE). A schematic of the DE process is shown in Fig. 2.1. The DE process will produce a K-shell transition when the electron that is excited is from the 1s atomic level.

K-shell spectral line emission can also be produced by the process of ‘cascading’. Cascading is a process by which an electron, which has been excited to a high atomic level ( $n \geq 3$ ), decays to the ground state via a series of radiative transitions, and thus ‘cascades’ down the atomic levels. The schematic for the way in which the process of cascading produces K-shell spectral line emission, is shown in Fig. 2.2.

The intensity of K-shell line emission from cascades depends on the EIE cross section for excitation to the higher lying atomic levels, and requires knowledge of all of the radiative rates for all possible transitions that can happen. For example, if a 1s electron in a heliumlike ion is excited to the  $1s3p_{1/2}$  level, it can decay to the  $n=2$  level or decay directly

---

<sup>1</sup>For ion-neutral collisions resulting in photon emission substitute the density of electrons with the density of neutrals in the trap and the velocity of the electrons with the ion-neutral collision velocity.

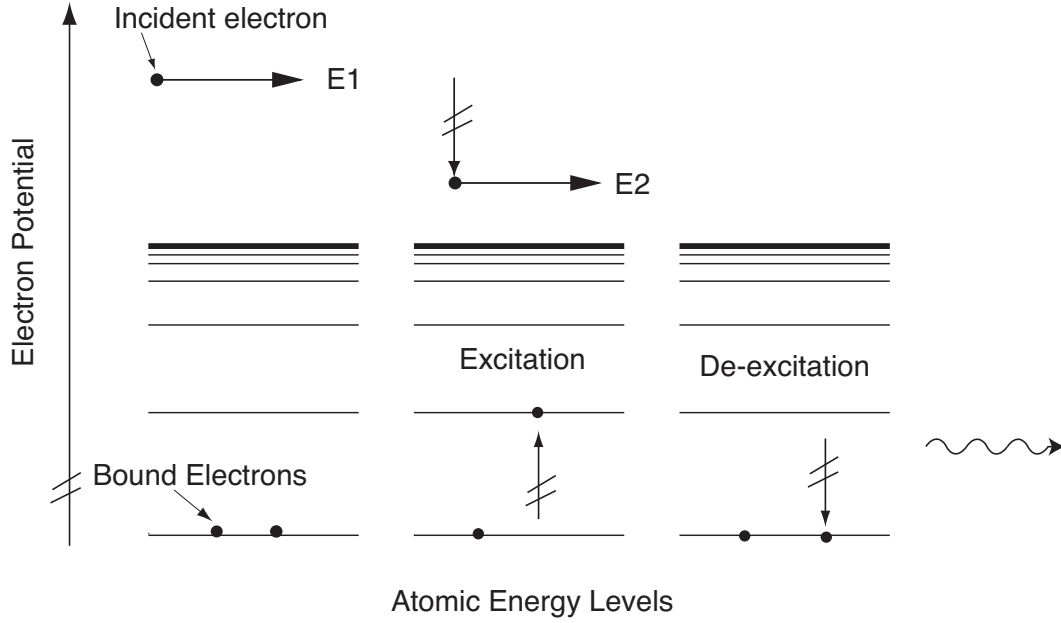


Figure 2.1: Schematic for the direct excitation process. The incident electron collides with an ion and excites a bound electron to a higher atomic level. The excited electron, then, radiatively decays to the bound state. This represents the case of a heliumlike ion, as there are two electrons in the ground state. Levels are not to scale.

to the ground state. For most applications the affect of cascades from higher lying levels to the intensity of a K-shell transition is calculated in a collisional radiative model.

### Radiative Recombination and Charge Exchange

Besides EIE emission, photon emission can be produced via radiative recombination (RR). Radiative recombination in EBIT is the process where a free electron from the electron beam is captured by a trapped ion, and emits a photon equal in energy to the binding energy of the atomic level the electron is captured into, plus the kinetic energy of the free electron. An RR spectral feature, then, is higher in energy than the energy of the electron beam by the binding energy of the atomic level the electron is captured into. The schematic for RR is shown in Fig. 2.3.

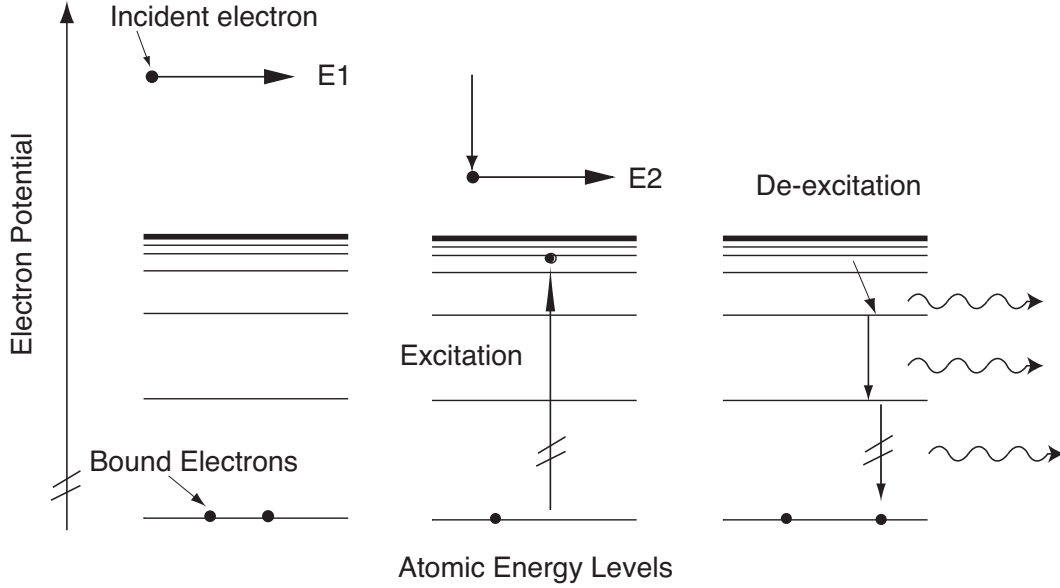


Figure 2.2: Schematic for the direct excitation with cascades process. The incident electron collides with an ion and excites a bound electron to high lying atomic level. The excited electron, then, radiatively decays to the ground state through a series of intermediate atomic levels. Each time the electron decays it emits a photon. The upper state of a  $n=2$  to  $n=1$  transition can be fed by this process. Levels are not to scale.

When bare and hydrogenlike ions are present in the trap, the RR process can produce K-shell spectral lines. This happens when the electron is captured into a  $n=2$  or higher atomic level and then decays down to the ground state. This will produce K-shell spectral lines of hydrogenlike and heliumlike charge states only. This is because for lithiumlike and lower charge states, the K-shell is filled when the electron is captured and thus the electron can only decay as far as the  $n=2$  shell.

The intensity of the K-shell spectral line emission from RR is dependent on the RR cross section for capture into a high lying level. In low- $Z$  ions, the cross section for RR is over 1000 times smaller than the K-shell EIE cross sections at the same energy. However, for high- $Z$  ions, the cross sections for RR start to be comparable to the cross sections for K-shell EIE, because RR cross sections scale as  $Z^{-2}$ , whereas EIE cross sections scale as

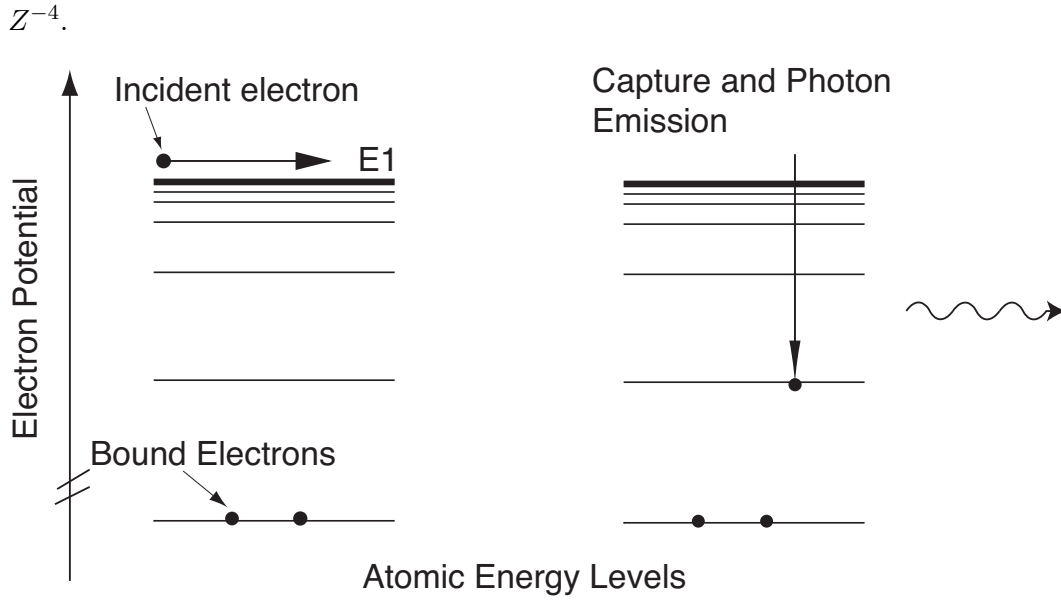


Figure 2.3: Schematic for the radiative recombination (RR) process. The incident electron is captured by the ion into an atomic level. The photon that is emitted has the energy of the electron beam plus the binding energy of the atomic level captured into. The process also reduces the charge state by one. Levels are not to scale.

Charge exchange recombination is similar to radiative recombination, except instead of the ion capturing an electron from the electron beam, the ion captures the electron from a neutral gas molecule/atom present in the trap. The electron is captured into a high lying level (usually greater than  $n=10$  for high- $Z$  ions) and then will cascade down and can produce spectral lines. However, as with RR, K-shell spectral lines from charge exchange recombination can only be produced when bare and hydrogenlike ions are present in the trap.

In low- $Z$  ions, charge exchange has a relatively small rate compared to the EIE process. The cross section for the charge exchange process can be estimated as the ion charge times  $10^{-15} \text{ cm}^2$ . In higher- $Z$  ions of the same charge state, the cross section for electron capture will become larger (as the ion charge state will increase), but the EIE cross

section will go down because of the  $Z$  scaling. Thus at high- $Z$  ions, the charge exchange rate can be comparable to the EIE rate<sup>2</sup>.

### Innershell Ionization

When the energy of the electron beam is high enough to remove a  $1s$  electron, x-ray emission can be produced by the innershell ionization process. Innershell ionization can produce K-shell spectral lines by ionizing a  $1s$  electron in lithiumlike and lower charge states. The ion that has been ionized, is left in the excited state of the next higher charge state and will either radiatively decay to the ground state, or it will undergo Auger decay. An example is the innershell ionization of a  $1s$  electron in the lithiumlike electronic ground state configuration of  $1s^22s$  to produce the state  $1s2s$ . The  $1s2s$  electronic configuration, is the upper level of the  $1s2s$  to  $1s^2$  transition in the heliumlike charge state and so innershell ionization can be responsible for producing photons.

#### 2.2.1 Polarization of X rays from EBIT

The intensities of spectral lines can be used to determine the cross section for a physical process. Spectrometers used to record spectral line emission on EBIT are arranged perpendicular to the beam direction and thus, if there is any anisotropic emission of spectral lines, this must be taken into account, if the total cross section is to be measured.

Spectral line emission from EBIT can be polarized and emitted anisotropically. This is because the magnetic sublevels of the upper level in the transition are populated unevenly due to the directionality that the presence of the electron beam produces. For

---

<sup>2</sup>However in many cases the density of neutral gas in the trap region determines the charge exchange rate.

electric dipole transitions (E1) produced by EIE, the relation between the intensity observed at  $90^\circ$ ,  $I(90^\circ)$ , and the average intensity averaged over  $4\pi$  is [29],

$$I(90^\circ) = \frac{3}{3-P} \langle I \rangle, \quad (2.2)$$

where  $P$  is the linear polarization of the spectral line, defined as,

$$P = \frac{I_{\parallel} - I_{\perp}}{I_{\parallel} + I_{\perp}}. \quad (2.3)$$

For K-shell transitions, the polarization of an electric dipole transition is related to the populations of the various magnetic sublevels,  $m_j$ . For instance, take the example of the Lyman- $\alpha_1$  transition in a hydrogenlike ion ( $2p_{3/2} \rightarrow 1s$ ). There are four different  $m_j$  values,  $m_j = \pm 1/2$  and  $m_j = \pm 3/2$ , and because the  $m_j = \pm j$  sublevels are populated evenly, the polarization,  $P$ , is expressed as the ratio of the populations of the various magnetic sublevels,

$$P = \frac{3(N_{1/2} - N_{3/2})}{3N_{3/2} + 5N_{1/2}}, \quad (2.4)$$

where  $N_{3/2}$  is the population of the  $m_j = 3/2$  magnetic sublevel and  $N_{1/2}$  is the population of the  $m_j = 1/2$  magnetic sublevel as calculated in distorted wave calculations [30]. For transitions emanating from  $J = 1/2$  upper levels (such as the Lyman- $\alpha_2$  transition), the radiation is unpolarized. Polarization measurements have been performed on SuperEBIT and have found agreement with theory to the 20 % level [31].



## 2.3 Modification of EIE Cross Section Due to QED

Often measurements of line intensities in EBITs are done to test EIE cross section calculations. EIE cross sections are usually calculated with the distorted wave approximation method of Zhang et al. [30]. This method has been proven to be good to better than 20 % [32] for K-shell transitions in  $Z=26$  and lower- $Z$  ions. However, no data exist to test theory for K-shell transitions from high- $Z$  ions where a quantum electrodynamical effect is predicted to modify the EIE cross section. This effect is called the generalized Breit interaction (GBI).

The GBI is a generalized form of George Breit's equation for the magnetic and retardation effects associated with two bound electrons in the central field of an atom. Historically, Guant first described the magnetic interaction between the two Dirac currents (electrons) found in the heliumlike system [33]. His description was successful at describing the spectrum of helium. This effect can be written<sup>3</sup>,

$$H_G = -(\alpha/r_{12})\vec{\alpha}_1 \cdot \vec{\alpha}_2, \quad (2.5)$$

where  $\alpha$  is the fine-structure constant,  $r_{12}$  is the inter-electron distance and  $\vec{\alpha}_{1,2}$  are the Dirac matrices. This equation is added to the Coulomb potential part of the Hamiltonian for the helium atom, and accurately describes the spectrum seen from helium.

Breit, spurred on by his intention to include retardation effects for two electrons, wrote down another term that needed to be included [35, 36, 37]. The new Hamiltonian can be written,

---

<sup>3</sup>as taken in the form described in Mann and Johnson [34]

$$H_B = -(\alpha/r_{12})(\vec{\alpha}_1 \cdot \vec{\alpha}_2 + \vec{\alpha}_1 \cdot \vec{n} \vec{\alpha}_2 \cdot \vec{n}), \quad (2.6)$$

where  $\vec{n}$  is a unit vector along the direction  $r_{12}$ . Although Breit's included the addition of the retardation term, like Guant, Breit's result successfully reproduced the fine spectrum of helium. This is because the magnetic interaction term is an order of magnitude larger than the retardation term according to Mann and Johnson [34].

Around the same time Christian Møller started investigating the scattering process of two electrons off each other in an early attempt at a quantum electrodynamical theory. He was guided by the correspondence principle and Born's perturbative scattering theory. In Born's theory, scattered particles undergo transitions to 'other' states by way of a perturbative excitation by the incident particle [38]. Møller's equation [39] can be written as<sup>4</sup>,

$$M = -(2/r_{12})(1 - \vec{\alpha}_1 \cdot \vec{\alpha}_2)e^{i\omega r_{12}}, \quad (2.7)$$

where  $\omega$  is the energy of the scattering process,  $\alpha$  is the fine-structure constant,  $r_{12}$  is the inter-electron distance and  $\vec{\alpha}_{1,2}$  are the Dirac matrices.

Although Møller derived his result for free-free interactions the result is the same for bound-free interactions, which are the types of interactions present in an EBIT, the Møller equation can be derived in the framework of QED by looking at the Feynman diagram for two electrons scattering off each other and working in the Lorenz gauge. However if the

---

<sup>4</sup>This equation is taken from Fontes et al [40] based on Møller's paper from 1932 [39]. In that paper  $\omega$  is the wavenumber of the exchanged virtual photon since we now see Møller scattering in the framework of QED, although Møller did not use that type of language.

Coulomb gauge is used, the so-called generalized Breit interaction is obtained. The GBI takes the form [40],

$$H_{GBI} = -2(\vec{\alpha}_1 \cdot \vec{\alpha}_2) \frac{e^{i\omega r_{12}}}{r_{12}} + 2(\vec{\alpha}_1 \cdot \vec{\nabla})(\vec{\alpha}_2 \cdot \vec{\nabla}) \frac{e^{i\omega r_{12}} - 1}{\omega^2 r_{12}}, \quad (2.8)$$

where  $\omega$  is the energy of the scattering process,  $\alpha$  is the fine-structure constant,  $r_{12}$  is the inter-electron distance and  $\vec{\alpha}_{1,2}$  are the Dirac matrices. For the limit of  $\omega$  going to zero the Breit interaction is found ( $H_B$ ). For local potentials, such as are employed in the Dirac-Hartree-Fock method of solving the potential in multielectron atoms, the Møller equation and the GBI are identical because of gauge invariance<sup>5</sup>.

A conceptual way to understand the GBI is as follows. In electrodynamics an electron has a charge, and if it moves, it produces a current which in turn produces a magnetic field. If there is another current source, there is a force between the two currents, and thus with two moving electrons there will be a force between the electrons. The magnitude of the magnetic interaction compared to the Coulomb interaction is given by  $v/c$ , where  $v$  is the speed of the particle and  $c$  is the speed of light. When the velocity of the electron is close to the speed of light, then the magnetic interaction starts to become more important. Thus the GBI is strongest when the electrons are traveling fast relative to each other as that is when the magnetic interaction is strongest.

In electron-impact ionization, the effect of adding the GBI to calculations is to increase the ionization cross sections. A measurement of the electron-impact ionization cross section of hydrogenlike uranium ions [28], showed that the cross sections calculated in the method of Zhang and Sampson [41] were too low by almost a factor of 2. These

---

<sup>5</sup>Please see Appendix B for a derivation of the Møller equation using the Feynman Calculus.

calculations were made without inclusion of the GBI into the calculation. Later Fontes et al. [42] did calculations of the electron-impact ionization cross sections including the GBI and found agreement with the data. This is the first and only measurement where the GBI has been proven to be needed to fit theory with experiment.

For K-shell transitions, ionization and excitation are very similar processes. The energy required to go from  $n=1$  to the continuum or to  $n=2$  is large, and the energy difference between the continuum and the  $n=2$  level is smaller than the difference between the  $n=2$  level and the  $n=1$  level. In some cases, the effect of adding the GBI to a calculation of an EIE cross section decreases the electron-impact excitation cross section. In other cases the opposite is observed. In the heliumlike charge state the EIE cross section that produces the  $1s2p_{3/2}$  to  $1s^2$  transition is decreased when the GBI is included, but is increased for the  $1s2p_{1/2}$  to  $1s^2$  transition [40]. This effect has never been measured or experimentally verified.

Recently, the Japanese EBIT group published the results of an experiment where they compared their measured values for dielectronic recombination cross sections to calculated values that include the GBI [43]. They found that to fit theory with experiment the GBI had to be included. However, because DR resonances are solely dependent on the Auger and radiative decay rates, both of which are dependent on the interaction of 2 bound electron states, the measurement of the GBI that they report is not the free-bound GBI effect of Fontes et al., but rather a well known effect first described by Mann and Johnson [34] (in which they referred to the equation as the generalized Breit interaction) in which the Breit interaction, described in 1929, shifts the energy levels.

## 2.4 Summary

Electron beam ion traps are used to study the atomic spectral line emission from highly charged ions. The dominate spectral line emission process is the EIE process. Experiments have confirmed the validity of calculations of electron-impact excitation of K-shell transitions for the distorted wave method for lower-Z ions, but no data exist for elements above iron ( $Z=26$ ). There is a predicted QED affect (that is largest on high-Z ions) that may need to be added when calculating EIE cross sections. However, this effect, the generalized Breit interaction, has never been measured in the EIE process.

## Chapter 3

# X ray Calorimeter Spectrometers

This chapter will describe the principle of x-ray calorimeter spectrometers and the design and operation of two such calorimeter spectrometers built by the Goddard Space Flight Center calorimeter group and used at EBIT for measurements of highly charged ions.

### 3.1 Basics

An x-ray calorimeter spectrometer is a device which measures energy, in the form of heat, from an absorbed photon. The idea behind x-ray calorimetry is that a photon interacts with a material (called the absorber) and is absorbed. The absorbed photon, then, heats up the absorber, and by measuring the change in the heat of the absorber an estimate of the energy of the photon can be made. Figure 3.1 shows the schematic of a basic design of a calorimeter. The absorber has a heat capacity,  $C$ , and is attached through a weak thermal link,  $G$ , to a heat bath at a temperature  $T_0$ . When a photon is absorbed in the absorber material, the temperature that the thermometer which is attached to the

absorber measures is given by,

$$T(t) = \frac{E_\gamma}{C} e^{-t/\tau_0}, \quad (3.1)$$

where  $E_\gamma$  is the energy of the incoming photon,  $C$  is the heat capacity of the absorber,  $\tau_0$  is the time constant for energy to leave the absorber through the weak thermal link given by  $C/G$ , and  $G$  is the conductance of heat through the weak thermal link to the heat bath.

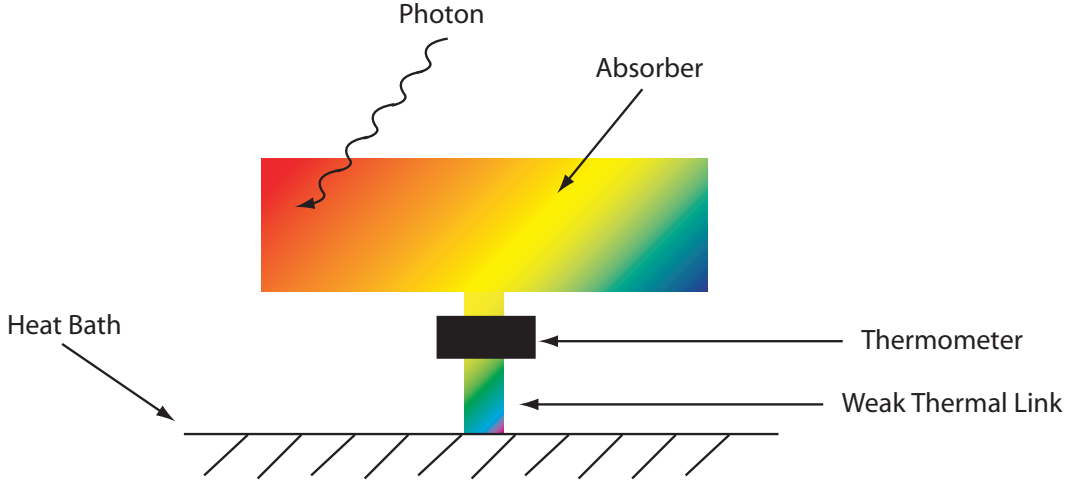


Figure 3.1: Schematic of a basic calorimeter.

### 3.1.1 Energy Resolution

In solid state detectors, the FWHM energy resolution that can be obtained is limited by the random exchange of electrons into the conduction band gap. A similar process is behind the main limitation of FWHM energy resolution in x-ray calorimeter spectrometers. The thermal bath, to which the calorimeter is attached, can exchange phonons and these

phonons can raise or lower the temperature of the device in what is known as thermodynamic fluctuations (TDFs). This can be thought of as a Poisson fluctuation in the number of phonons with energy  $k_b T$ . The TDFs are found to cause a spontaneous energy/heat fluctuation of the detector  $\Delta U$  [44],

$$\Delta U = \sqrt{k_B T^2 C}, \quad (3.2)$$

where  $T$  the temperature,  $k_B$  is Boltzman's constant, and  $C$  is the heat capacity at the temperature  $T$ . Thus the smaller the heat capacity and temperature the smaller the TDFs and the FWHM energy resolution.

To reduce the heat capacity (and thus the noise source from the TDF), using a small amount of absorber material is desired, as the more material there is the larger the heat capacity will be. Heat capacity is also a function of the temperature. In the low temperature regime, and assuming only phonons, the heat capacity  $C$  scales as  $T^3$ . Thus, the lowest heat capacity is achieved at very low temperatures. For this reason, the temperatures that calorimeters operate at are 50 - 100 mK.

From equation 3.2, then, it is possible to obtain an order of magnitude estimate of the size of the thermodynamic fluctuations and thus the limit of FWHM for calorimeters. Using a heat capacity of 1 pJ (which is what is assumed for a 100  $\mu\text{m}$  thick HgTe absorber<sup>1</sup>) and a detector temperature of 100 mK, it is found that the fluctuations should be a few eV. Thus, the upper limit of resolving power,  $E/\Delta E$ , for a 100  $\mu\text{m}$  HgTe absorber calorimeter detector is over 10000 for a 60 keV photon. For comparison, solid state detectors like high

---

<sup>1</sup>The thickness of 100  $\mu\text{m}$  for a HgTe absorber gives around 30 % quantum efficiency for 60 keV photons



purity germanium detectors, have resolving powers on the order of 100 for 60 keV photons.

### 3.1.2 Thermalization

The primary way in which x-ray photons under 100 keV deposit energy into the absorber material is by photoionization. Photoionization is where an incident photon is absorbed by a bound electron in an atom, which in turn leaves the atom. The electron ejected from the atom has the energy of the incident photon minus the binding energy of the atomic level it was in. This creates a ‘hot’ photoelectron<sup>2</sup>. The ‘hot’ photoelectron will collide with other electrons, and these electrons will, in turn, hit other electrons, and a shower of electrons will be produced. As the number of electrons in the shower increases, the average energy of each electron will drop, as each time an electron collides with another electron the average energy of the pair of electrons will be reduced. Phonons in the absorber start to couple to the electrons when the average energy of the electrons in the absorber is on the order of a few eV. Once the electrons couple to the phonons in the system, the absorber heats up.

The simple formula for the time dependent temperature response of a photon absorbed in a calorimeter is based on the assumption that the energy of the photon is thermalized instantly in the absorber. This is not the case as the thermalization time is finite. If the absorber thermalizes the photons on the time scale of the detector time constant,  $\tau_0$ , then the energy in the absorber will start to flow to the heat bath before the entire absorber heats up. This causes a situation in which the peak temperature deviation

---

<sup>2</sup>‘hot’ is used here as the energy of the electron will be much higher than the average energy of the electrons in the material. For instance if the electron is given 1 keV in energy that is over 4 orders of magnitude larger than electrons at room temperature.

from the thermal bath is not proportional to the photon energy and complicates the problem. This is not an ideal situation and is to be avoided.

The ideal calorimeter, then, would thermalize the absorbed photon quickly and have a small heat capacity so that the thermodynamic fluctuations are low and the resolving power,  $E/\Delta E$ , of the detector is high. Mercury telluride, HgTe, has been found to be a good material to be use as an absorber for a calorimeter, since it has a low heat capacity as well as good thermalization characteristics [45].

## 3.2 NASA/GSFC Type Thermistor Detectors

To measure the temperature of the absorber the calorimeter has to have a thermometer. The types of thermometers that are used on calorimeter spectrometers described in this dissertation are thermistor based systems. A thermistor is a resistor with a well known resistance vs temperature curve. By running a current across the thermistor a voltage drop is measured and the resistance is found. Since the resistance vs temperature curve is known, measuring the voltage drop across the resistor is the same as measuring the temperature.

### 3.2.1 Thermistor Circuit

To measure the voltage drop across the thermistor, a current flows through the thermistor. This current is kept constant by biasing, with a voltage, the thermistor through a ‘load’ resistor that has a larger resistance then the thermistor itself. This creates a situation in which the current flowing in the system is, to zeroth order, dependent on only

the load resistor. A basic circuit diagram for the thermistor readout is shown in 3.2. The thermistor is connected to a JFET source follower, which is used to match the impedance of the thermistor to an analog processing system that amplifies the signal and prepares it to be digitized.

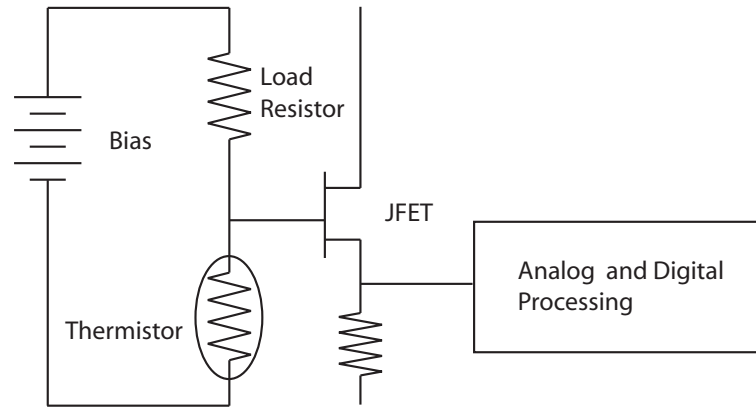


Figure 3.2: Basic schematic of thermistor circuit. Signal from thermistor goes through the JFET and then to the analog and digital processing units. Figure is adapted from [46].

A JFET, or junction gate field-effect transistor, is a transistor with two inputs and one output. The inputs are named the ‘source’ and ‘gate’ and the output is named the ‘drain’. Current flows through the ‘source’ and exits through the ‘drain’. The current that flows through the JFET is modulated by input voltage to the ‘gate’. A JFET, can be thought of as being similar to a flexible water hose. The amount of water through the hose can be controlled by squeezing it and reducing its cross section. The JFET modulates the current flowing through itself by increasing the resistance from the ‘source’ to the ‘drain’ by way of increasing, or decreasing, the electric field across the current carrying region.

The current running through the thermistor, used to measure the temperature, produces heat, which causes the thermistor to heat up, which, in turn, causes a shift in

the voltage drop across the thermistor. This sets up a feedback loop in which the current used to measure the heat of the thermometer heats up the thermometer, which in turn affects the measurement of the temperature of the absorber. Thus, the bias (or amount of current flowing through the thermistor) has an effect on the signal output. This bias can either reduce the output voltage (negative feedback), or boost the signal (positive feedback). Positive feedback is obtained when the load resistor is smaller than the thermistor resistance and is useful when the noise from the amplifier is too ‘loud’ and thus it is desirable to have a ‘louder’ signal. Negative feedback happens when the load resistor is larger than the thermistor, and is useful for creating a bias stability region. A bias stability region is a range of values in the value of the bias whereby the response of the output signal to a small perturbation in the bias is smooth and perturbations in the bias will not effect the output signal.

Negative feedback is useful as in some situations there is a large difference in the energies of the photons being detected. An example is the K-shell and L-shell spectra of xenon. The energy of K-shell x-ray emission from xenon is at around 30 keV as opposed to the L-shell x-ray emission at 5 keV. In this situation the temperature rise from an absorbed K-shell photon is larger (by a significant fraction) than the temperature rise from an absorbed L-shell photon and will cause the detector to be put much farther out of temperature equilibrium and, thus, to take more time to return to equilibrium. The amount of time that the system needs to return to equilibrium by the weak thermal link is related to the time constant for the system (C/G). Negative feedback increases the speed by which heat is dissipated from the absorber by converting heat energy into electrical energy and

dumping it into the electricity running through the thermistor. This allows the detector to increase the number of counts it can receive before it is effected by pileup. In addition the effect that negative feedback has on the detector is to cause it to have a more linear response to photon energy<sup>3</sup>.

### 3.2.2 Thermistor Design

The thermistors used in calorimeters in this dissertation are manufactured by doping silicon with phosphorus and boron to produce a small amount of impurity sites [46, 47]. The doped semiconductors conduct electrons in the low temperature regime by variable range hoping (VRH) [48]. Variable range hopping is a process by which electrons hop from one impurity site to another by way of phonon assisted tunneling. The electron can hop from dopant sites of variable distance, as the Coulomb force effectively smears out the energy levels of the dopant atoms. A ‘hop’, then, is made by emission or absorption of the proper energy phonon. For VRH, the resistance as a function of temperature is given by [48],

$$R(T) = R_0 \exp \left( \sqrt{\frac{T_0}{T}} \right), \quad (3.3)$$

where  $T$  is the temperature of the semiconductor,  $T_0$  is a term that can be controlled by the dopant properties (depth, amount, and dopant), and  $R_0$  is a term that is controlled by the geometry of the thermistor region (distance between electrical connections and aspect ratio of the doped area). To match the thermistor resistance to the resistance of the JFET

---

<sup>3</sup>A linear response in photon energy means a linear increase in photon energy will cause a linear increase in pulse height.

and have a lower resistance than the  $90\text{ M}\Omega$  load resistor, the thermistor should have a resistance of  $\sim 10\text{ M}\Omega$ . To achieve this an optimization of the size of thermistor and dopant strength versus FWHM energy resolution needs to take place, as the size of the thermistor (and thus the amount of dopant atoms needed to create it) can adversely effect the FWHM energy resolution. From this optimization, it was found that the value of  $T_0$  should be around 5-6 K and the thermistor size be roughly  $200 \times 200 \times 0.5\text{ }\mu\text{m}$  [47, 49].

### 3.2.3 Pulse Height Determination

The determination of the pulse height of the voltage pulse resultant from an absorbed x-ray photon by the digital signal processor is made in the frequency domain (by Fourier transforming the voltage pulse) rather than the time domain. This is because of the noise in the calorimeter system. The noise can either be electrical in nature like amplifier noise, or thermodynamical in nature like the TDF noise. All of these noise sources add together on the voltage pulse and in the time domain make it difficult to find the pulse height of the pulse because the noise in each time bin is correlated with each other time bin. However in the frequency domain, the contribution to the signal from the noise is easier to deal with as the noise from each frequency bin is not correlated with each other bin [50].

The noise sources in the system are the TDF noise, the Johnson noise (electrical noise from resistors),  $1/f$  noise (from the thermistor<sup>4</sup>), noise from the JFETs, amplifier noise, and outside noise sources such as 60 Hz electrical noise from the power outlets [51, 50].

---

<sup>4</sup>The noise term comes from a non-ideal behavior related to deviation from the variable range hopping conduction model. For more information please see Stahle et al. [49]

## Frequency Domain

In the frequency domain the shape of the voltage pulse resultant from an absorbed x-ray event is essentially flat in frequency over some range and then drops as  $1/f$  above a frequency  $f_c$ . The bulk of the power in the pulse is contained in frequencies below a cutoff frequency defined by,  $f_c = G/(2\pi C)$ , where  $C$  is the heat capacity of the calorimeter (absorber and thermistor) and  $G$  is the thermal conductance of the weak thermal link. This cutoff frequency is defined as 1 over  $2\pi$  times the characteristic time for the weak thermal link to remove energy from the calorimeter.

The thermodynamic fluctuations, as defined in section 3.1.1, have the same functional form as the voltage pulse from an absorbed x-ray event [50]. Each frequency bin, then, gives an estimate as to the pulse height of the voltage pulse. Since the TDF noise term and the voltage pulse have the same functional form, the signal-to-noise ratio is the same in all frequency bins. By averaging  $n$  number of frequency bins, the signal-to-noise ratio will improve by  $\sqrt{n}$ . If the number of bins is extended to  $2\pi f_c$ , the error in the determination of the energy of the incident photon will be equal to the value of the TDF,  $\sqrt{k_b T^2 C}$ . Going to an arbitrarily high number of frequency bins allows the pulse height to be determined to a high level of accuracy [50]. However, if the signal falls faster than  $1/f$ , or if the signal-to-noise ratio is reduced from the ideal case described above, as is the case if there are other sources of noise with a different functional form, then, adding more frequency bins does little to increase the accuracy of the determination of the pulse height. In real terms, then, the FWHM energy resolution of a calorimeter that can be realized is proportional to the size of the thermodynamic fluctuations as well as to how many frequency bins have a

good signal-to-noise ratio. Thus to make a high-resolution calorimeter spectrometer, it is desirable to maximize the number of frequency bins included in the determination of the pulse height in the frequency domain and minimize the thermodynamic fluctuations.

Because the determination of the pulse height (to a high accuracy) depends on the amount of frequency bins included in the analysis as well as on the functional form of the noise in the system, a filtering technique is applied to find the optimal pulse height of the voltage pulse and thus the energy of the photon.

### **Optimal Filter and Pulse Height Detection**

To find the pulse height of the voltage pulse, and thus determine the energy of the photon, the pulse is compared with an ‘optimal filtering template’. This ‘optimal filtering template’ is found by assuming that all of the voltage pulses from the photon absorption process have the same shape [52]. In the time domain, then, a voltage pulse has the functional form,

$$A \times S(t), \tag{3.4}$$

where A is the amplitude (and thus related to the energy of the photons) and S(t) is the pulse shape. The pulse height estimate then is found by doing a least squares fitting in which the difference between the data,  $D(t)$ , and the model of the pulse height S(t) is minimized [52]. In the frequency domain the expression is,

$$\chi^2 = \sum \frac{[D(f) - H \times S(f)]^2}{N^2(f)}, \tag{3.5}$$



where  $D(f)$  is the Fourier transform of the voltage pulse,  $H$  is the pulse height,  $S^*(f)$  is the pulse that has been Fourier transformed into the frequency domain, and  $N^2(f)$  is the power spectrum of the average noise. From this  $H$  is found to be, by setting the derivative to zero, [52],

$$H = \sum \frac{[D(f) \times S^*(f)]}{N^2(f)}, \quad (3.6)$$

and transformed back to the time domain [52],

$$H = \sum D(t) \times F(t), \quad (3.7)$$

where  $F(t)$  is the optimal filtering template, and is given by the inverse Fourier transform  $S^*(f)/N^2(f)$ . To find the pulse height of a voltage pulse resultant from an x-ray being absorbed in the calorimeter, the optimal filtering template must be found.

The optimal filtering template requires the pulse shape and the average noise spectrum to be known. To find the pulse shape, the average pulse is found by averaging together something on the order of 100 separate voltage pulses from x-ray absorption events. The average noise spectrum is found by taking the Fourier transform of the signal (integrated over a set time like 30 sec) from the thermistor, when no photons are being absorbed by the detector, and then averaging these together.

At the beginning of each measurement it is customary to make a new template for the calorimeter spectrometer. This is important, as the determination of the pulse height is dependent on the noise, and the outside electrical noise (such as a new electrical device located near the spectrometer) can change and thus cause the template to be invalid. Also,

the pulse shape is somewhat dependent on the energy of the incident photon energy, and as such to gain the best FWHM energy resolution, the average pulse should be created from photons of similar energy.

The CDP applies the optimal filter via a convolution in the time domain. The length of the filter determines the quality of the pulse height determination. For the high energy pixels on the ECS<sup>5</sup>, the length of the filter is  $\sim 400$  ms. Every pulse that arrives in the CDP is tagged with the time of the x-ray event and a flag that differentiates the quality of the pulse height estimation. If pulses arriving in the detector are separated by a time of 400 ms or more, then the full optimal filter is applied and the pulse is determined to be a ‘high-res’ pulse. If the pulses come into the CDP in a time shorter than 400 ms, then a shortened filter is applied and the pulses are either given ‘mid-res’ or ‘low-res’ tags. The FWHM of the ‘mid-res’ and ‘low-res’ pulses is much worse than the ‘high-res’ events. As such in most experiments, only ‘high-res’ events are used. If there are tags for pixels other than ‘high-res’, it indicates pile-up of counts in the detector. For the Suzaku X-ray Observatory, a calculation of the expected fraction of each pulse tag was done [23]. For a filter length of 166 ms, it was found that at 5 counts/sec/pixel only 20 % of the counts will be ‘high-res’ and the rest will be ‘mid-res’ and ‘low-res’. For a filter length of 400 ms, then a count rate of 2 counts/sec/pixel will produce only 20 % ‘high-res’ events.

If there is a significant amount of pile-up of counts (as indicated by a reduction in the fraction of ‘high-res’ events), a shift in the measured pulse height of a spectral line and a degradation in the FWHM resolution will be seen. It is important, then, that if a measurement is taken at two different count rates that this shift be taken into account.

---

<sup>5</sup>see section 3.6

### 3.3 XRS/EBIT x-ray spectrometer

The XRS/EBIT x-ray spectrometer is a microcalorimeter designed and built at NASA/GSFC [53]. The calorimeter's original design was for use in space observing astrophysical sources. The first quantum microcalorimeter was put aboard the Astro-E satellite mission launched from Japan in 2000 [54]. The rocket however exploded before it got into orbit and the mission was delayed. In 2000 GSFC loaned the LLNL EBIT group a flight spare of the calorimeter. The success of the calorimeter was immediate [22]. In 2003, a second generation calorimeter was built, which included several design improvements. The first calorimeter had a resolution of roughly 10 eV at a photon energy of 6 keV, whilst the second calorimeter, dubbed the XRS/EBIT<sup>6</sup>, has a resolution of 6 eV at a photon energy of 6 keV as well as a much more uniform Gaussian line shape [53].

The XRS/EBIT is an array of 36 independent thermistor based calorimeter detectors (which from now on will be referred to as pixels)<sup>7</sup> in which 32 have 624 x 624 x 8  $\mu\text{m}$  HgTe absorbers and four 624 x 624 x 30  $\mu\text{m}$  bismuth absorbers have been glued on. The 8  $\mu\text{m}$  thick HgTe absorbers give an energy resolution of around 6 eV at a photon energy of 6 keV while the bismuth absorbers give a resolution (for the best pixel) of 75 eV at a photon energy of 60 keV. The bismuth was placed on the array as a test to try and obtain a higher resolving power for high-energy photons than solid state detectors. A picture of the XRS/EBIT array is shown in Fig. 3.3. The XRS/EBIT is housed in a laboratory version of the XRS detector assembly [55]. The HgTe absorbers were grown by Texas Instruments on

---

<sup>6</sup>The name of that instrument for the satellite Astro-E, was the XRS (or X-Ray Spectrometer). The version located at EBIT has been given the name XRS/EBIT to denote that it is not the original instrument.

<sup>7</sup>The array is a square 6 x 6 array in terms of positions for pixels. However, there are only enough electronic signal processing channels for 32 pixels to be read out at one time. The extra pixels then serve as spares that can be wired into the electronics in case of failures with other pixels.

CdZnTe wafers using Molecular Beam Epitaxy [49], and the bismuth absorbers were grown at GSFC using vapor deposition.

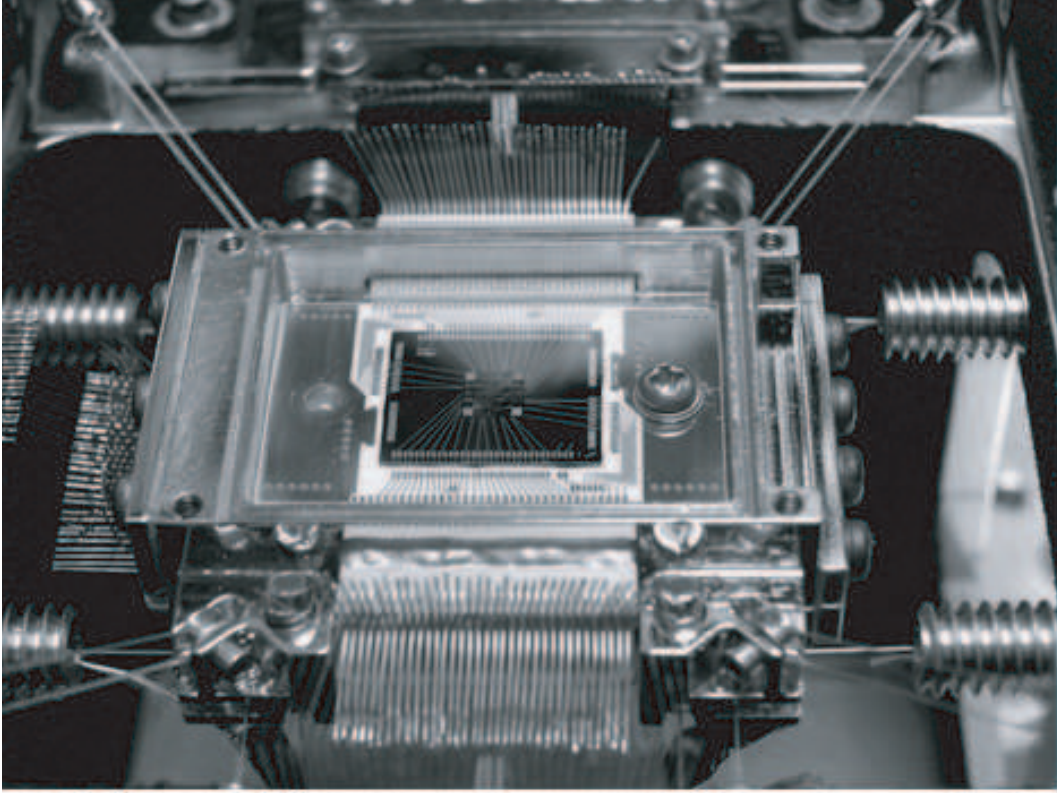


Figure 3.3: Picture of XRS/EBIT array in detector assembly.

The XRS/EBIT detector uses doped silicon thermistors to readout the temperature (and thus determine the energy of incident photons). The absorbers are thermally connected to the thermistor through a  $10\text{ }\mu\text{m}$  high SU-8 epoxy tube in which epoxy is applied to the absorber and then attached to the SU-8 [53]. The SU-8 allows phonons to travel to the thermistor but does not allow for electrons from the absorber to travel to the thermistor. This helps to increase the resolution of the device, as well as to create a more uniform line shape. The previous calorimeter design (the one that was delivered to LLNL

in 2000) had the absorbers attached directly to the thermistor, and as such, electrons could travel directly into the thermistor and disrupt the conduction mechanism.

A picture of an XRS/EBIT style thermistor pixel is shown in Fig. 3.4. The thin silicon supports provide the weak thermal link to the heat bath and the tabs with the raised SU-8 are on the side. The leads to the pixels are made by degenerately doping the silicon with phosphorus until it is conductive. The thermistor region is in the middle of the pixel with the two degenerately doped leads extending down opposite sides of the thermistor.

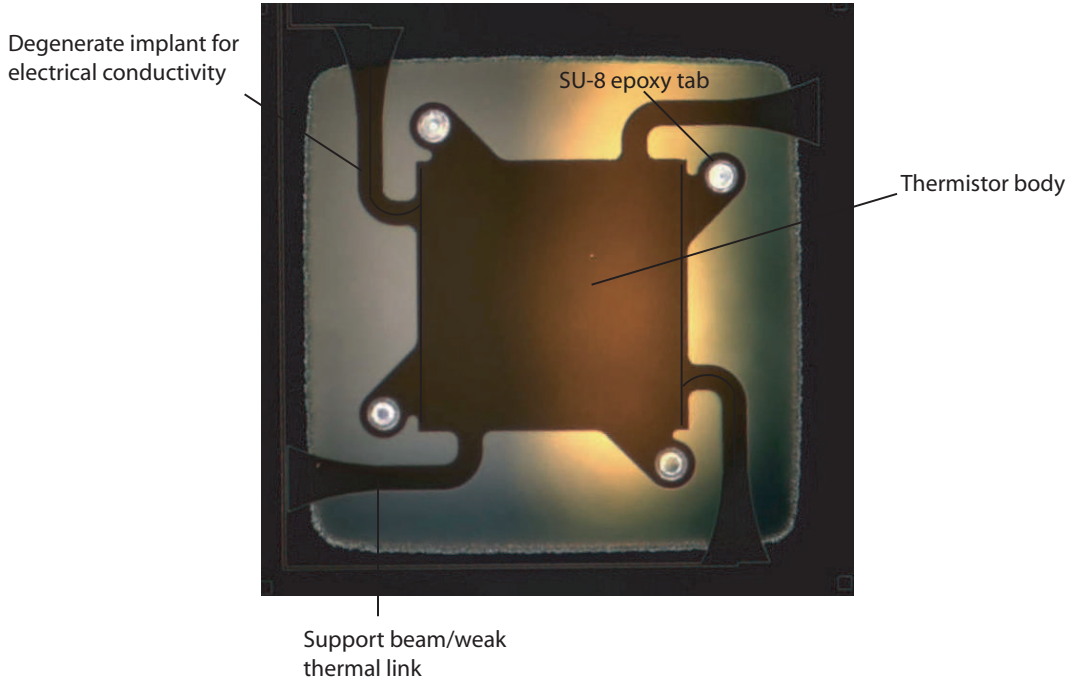


Figure 3.4: Picture of XRS/EBIT style pixel. Electrical wires have been visually enhanced to aid visibility. Support beams double as the weak thermal link to the heat bath. SU-8 epoxy tabs are used to connect the absorber to the pixel. The thermistor body is seen between the two electrical connections running on each side of the pixel.

The XRS/EBIT runs at a detector temperature of 60 mK by way of a system of a pumped LHe dewar and an adiabatic demagnetization refrigerator (ADR). The pumped LHe dewar is able to achieve a temperature of 1.5 K by way of pumped evaporative cooling,

which is when a pump is used to evacuate the LHe dewar. This creates a situation where the vapor pressure on top of the liquid helium is reduced, and the liquid is cooled by evaporative cooling. From a temperature of 1.5 K the ADR brings the array to a temperature of 60 mK. The ADR is described in detail in reference [55].

To allow the XRS/EBIT detector to run at a temperature of 60 mK, thermal shielding is provided by the laboratory version of the XRS detector assembly to shield the 300 K room temperature. The first thermal shielding stage is the liquid nitrogen (LN2) stage. This reduces the temperature down to 77 K. The second thermal shielding stage is then the liquid helium (LHe) stage. This reduces the temperature down to 4.2 K (1.5 K when pumped). The LN2 needs to be refilled twice a day and the LHe needs to be refilled every two days. Thus the XRS/EBIT is man hour intensive to keep cold (and thus to run).

The ADR contains is a ferric salt pill (chemical composition  $\text{FeNH}_4(\text{SO}_4)12 \text{ H}_2\text{O}$ ) that was grown at GSFC [55]. The ADR works by moving heat energy from the detector to the salt pill in the form of randomizing the magnetic moments in the salt pill. The ADR salt pill is surrounded by a large electromagnet, which ramps up to 9 A, and produces a several Tesla magnetic field. When the field is on, the magnetic moments in the salt pill align. The magnet then reduces the magnetic field (by reducing the current in the magnet wires) by a small and controlled amount (with feedback from a thermometer) and the magnetic moments are no longer forced to be aligned. As it does that, the energy that is in form of heat in the detector goes into increasing the entropy in the salt pill by de-aligning the magnetic moments of the ferric salt, and the whole system is cooled. The magnet is ramped down until there is no current left, and the current running through the magnet must be

ramped up and the process started again. The hold time for the magnet to keep the detector at 60 mK is 12 hours. The process of regenerating the magnet takes roughly 90 minutes.

The detector region and the thermometers are kept at 60 mK, but the JFETs, which send the signal to the analog processor, are kept at 130 K to avoid too much noise (JFETs are very noisy when they are too cold). To avoid having the JFETs put a high heat load on the detector, the JFETs are thermally isolated. The load resistor has a value of 90 M $\Omega$ , and the thermistor at 60 mK has a value of roughly 10 M $\Omega$ , thus the detector is operated in the negative feedback regime.

A signal pulse from an absorbed x ray emanating from the thermistor, goes through the JFET and then moves into the analog processing unit called the Calorimeter Analog Processor or CAP. The CAP is responsible for taking out the DC bias (which is used to drive the current through the thermistor) by having a high pass filter in line with the signal where frequencies under 10 Hz are reduced in amplitude. The CAP amplifies the signal by 20,000 times, which produces pulse heights on the 1 V level. The pulses then go into the Calorimeter Digital Processor or CDP<sup>8</sup>. The CDP is where the template is applied and the pulse height determination is done. From there the pulse heights are sent to a data collection program and are recorded according to the time the x ray arrived as well as the pulse height of the photon in volts.

---

<sup>8</sup>Not a financial derivative!

### 3.4 Stacked pixel and Resolution studies

#### Four-Stack Absorber

One way to gain quantum efficiency (QE) is to make the absorber thicker, as an increase in the thickness of a material used for stopping photons increases the QE of the material. Since a large amount of HgTe was on hand at GSFC and HgTe is a well characterized material, a test of the energy resolution that could be obtained by using thicker HgTe absorbers was done (in comparison to the  $8\mu\text{m}$  thick HgTe pixels used on XRS/EBIT).

The test absorber, or ‘4 stack’ absorber, consisted of four  $8\mu\text{m}$  HgTe absorbers (of the same type used on the XRS/EBIT spectrometer) epoxied together and placed on an XRS/EBIT style thermistor. The spectrum obtained by exposing the absorber to a radioactive  $^{241}\text{Am}$  source is shown in Fig. 3.5.  $^{241}\text{Am}$  has a number of lines from 10 keV to 60 keV, but the strongest line is the line at 60 keV. The energy resolution of 45 eV at a photon energy of 60 keV was found for the ‘4 stack’ absorber pixel.

The energy resolution of the ‘4 stack’ absorber is roughly a factor of two improvement over the resolving power obtained with the bismuth pixels, and as such thick HgTe absorbers were thrust into the spotlight in the search for obtaining a high QE material for detecting high-energy photons.

#### 3.4.1 Resolution Study

With the promising results of the stacked absorber test, and as part of this dissertation, an effort to predict what the FWHM energy resolution of thicker HgTe pixels would



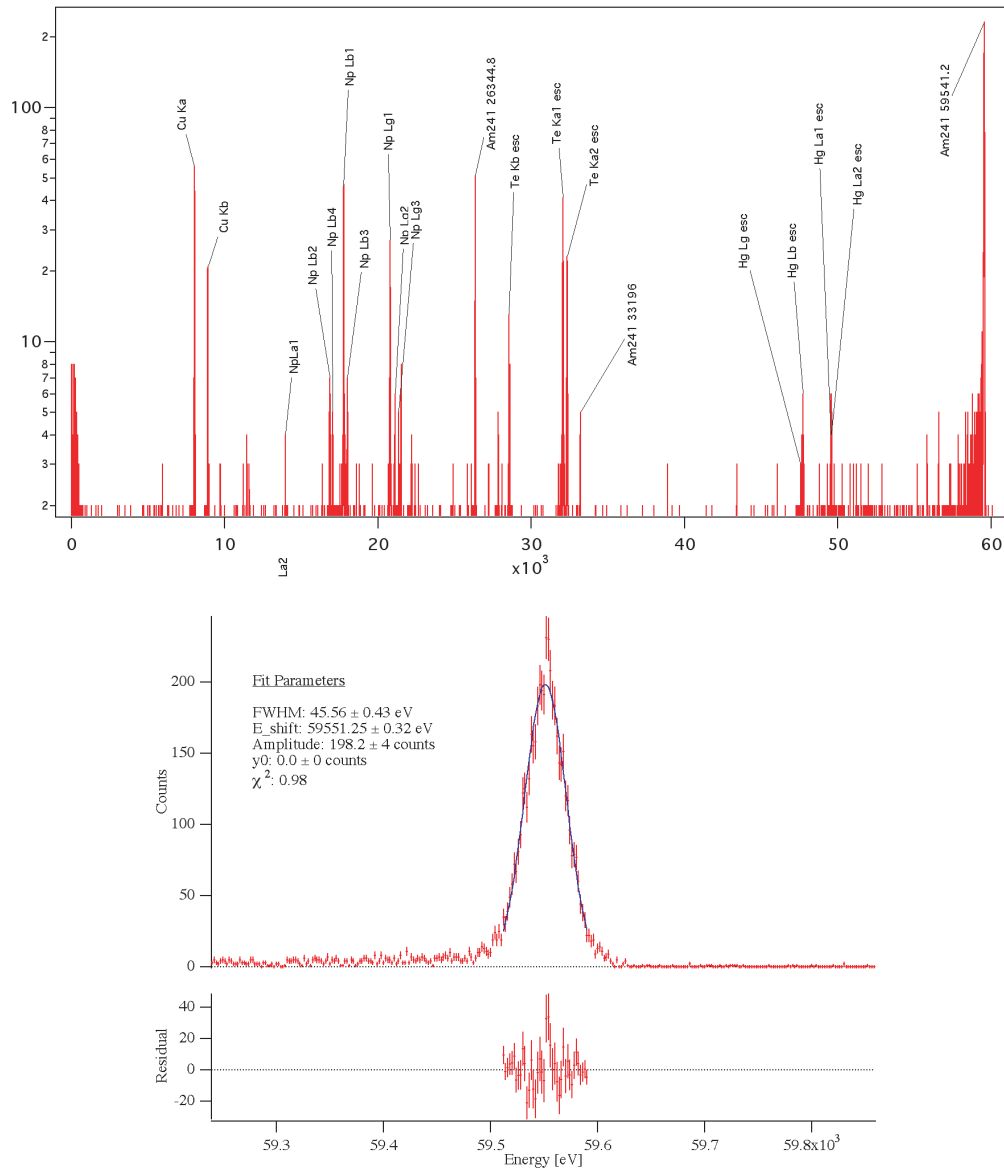


Figure 3.5: Top: Spectrum recorded with the ‘4 stacked’ pixel at 60 mK. Bottom: Fit to the 60 keV gamma ray from <sup>241</sup>Am. The fit shows 45 eV resolution at 60 mK.

be was modeled. The model was based on the method that the  $\mu$ Cal code uses to model voltage pulses from GSFC type calorimeters, which is described in detail in reference [56].

$\mu$ Cal was developed to model the response of the calorimeters designed at GSFC. It solves a set of coupled partial differential equations related to all sources of noise in the detector as well as to the transport of heat in the absorber-thermistor system. The code outputs the pulse height that would be expected for an arbitrary photon energy. In addition it estimates what the resolution would be at the incident photon energy.

The model developed for predicting the energy resolution of thick HgTe absorbers, includes photon energies up to 80 keV, thicknesses of HgTe from 8  $\mu$ m to 50  $\mu$ m , and operating temperatures of 60 mK to 90 mK. The result for the pulse heights predicted by the model for 8  $\mu$ m thick and 50  $\mu$ m thick HgTe absorber operated at a detector temperature of 60 mK is shown in Fig. 3.6. It was seen that an operating temperature of 60 mK produces the best energy resolution for 60 keV photons. This is expected as at lower temperatures, the heat capacity is lower and the FWHM energy resolution scales with the heat capacity. For the 8  $\mu$ m thick absorber the pulse height as a function of energy for photons above 20 keV starts to show significant non-linearity, whereas for the 50  $\mu$ m thick absorber, the non-linearity is barely visible. This is expected, as the thicker absorber has a higher heat capacity, and thus can handle larger photon energies before it gets too far out of equilibrium.

Figure 3.6 highlights the effect of the bias voltage. The bias voltage is the voltage that is applied to drive current through the thermistor. The higher the bias, the more current that runs through the thermistor. The more current that runs through the thermistor the more self-heating the thermistor experiences and the effect is to linearize and reduce

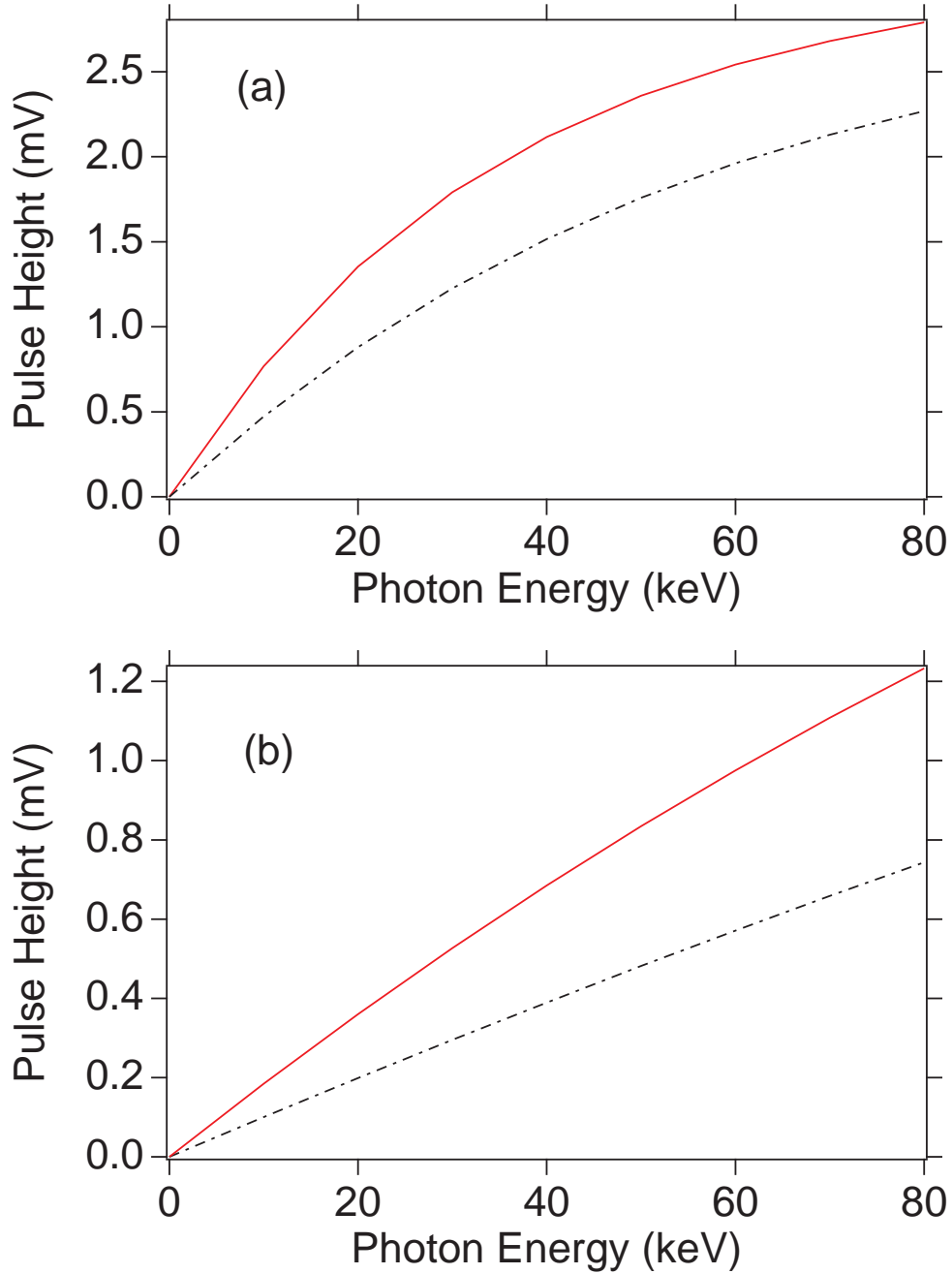


Figure 3.6: Calculated pulse height response for 8  $\mu\text{m}$  thick and 50  $\mu\text{m}$  thick HgTe absorbers. Graph (a) represents the predicted pulse heights for photons from 0 to 80 keV in energy absorbed by a 8  $\mu\text{m}$  HgTe absorber for bias voltages of 2 V and 5 V running at 60 mK. Graph (b) represents the predicted pulse heights for photons from 0 to 80 keV in energy absorbed by a 50  $\mu\text{m}$  HgTe absorber for bias voltages of 2 V and 5 V running at 60 mK. The bias voltages representing 5 V are shown as the dotted line and the solid line is for bias voltages of 2 V.

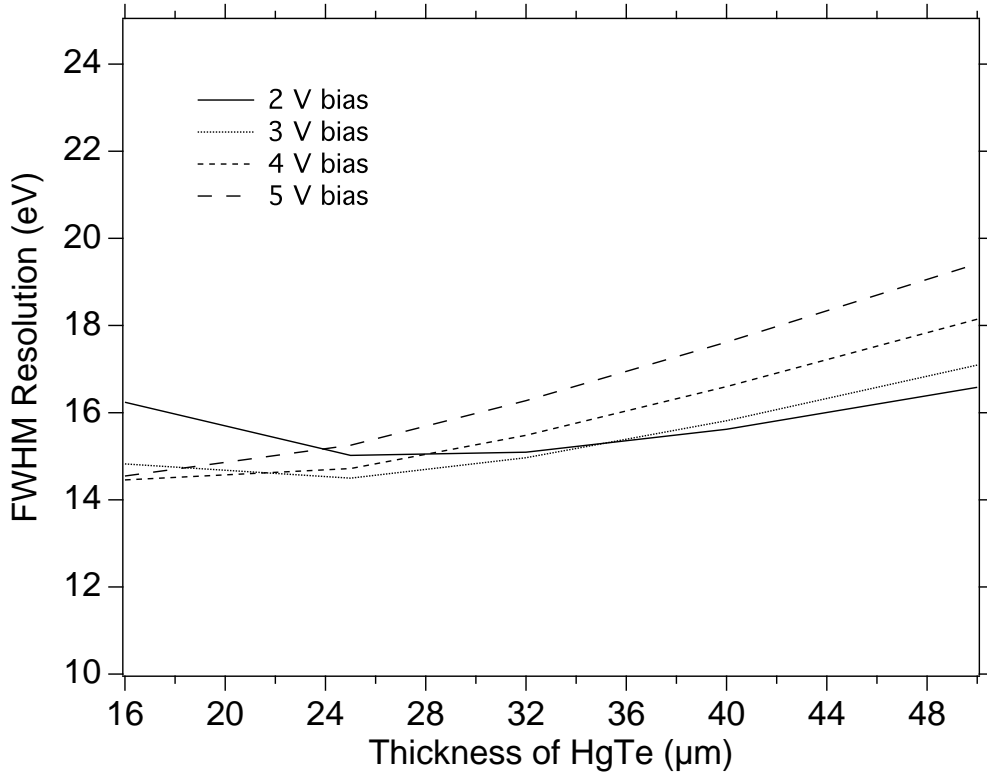


Figure 3.7: Prediction of resolution attainable with different thickness of HgTe absorbers at 60 mK detector temperature. Different color curves are for bias voltages of 2 - 5 V. For a thickness of 50  $\mu\text{m}$  of HgTe a resolution of around 20 eV is expected.

the overall pulse height. This is because the self heating adds a higher heat capacity to the detector (because of the temperature dependence of the heat capacity) and thus lowers the pulse height.

The result for the resolution for an operating temperature of 60 mK and 1-5 V bias is shown in Fig. 3.7. The study found that one could expect a FWHM energy resolution of 20 eV at 60 keV for a 50  $\mu\text{m}$  thick HgTe absorber, which is a wonderful result considering that Ge detectors yield around 400 eV or higher.

Because of the non-linearity in the response of the calorimeter to high-energy photons the resolution that  $\mu\text{Cal}$  predicted was multiplied by the derivative of the pulse

height response at the energy of 60 keV. This has the affect to add more uncertainty to the energy than would be expected at lower energies because at the higher photon energies, the response of the pulse height to a change in the photon energy is reduced. Even with the non-linearity estimate the model showed that we could expect never-before-heard-of resolving powers with fantastic QE for K-shell x-ray emission from high-Z ions.

To redesign a new calorimeter spectrometer that utilized thicker absorbers to gain high QE for high-energy photons, new sizes of the thermistor and values of the weak thermal link would need to be found. Since the process of redesigning the thermistors takes considerable amounts of time and money, as the thermistors must be manufactured on a large scale to test different compositions of thermistor doping and size, and that money or time was not available, it was decided that the current XRS style pixels would be retrofitted with thicker pixels, as the resolution study showed they can have unheard of energy resolution when compared to Ge detectors.

### **3.5 Test of a High Quantum Efficiency Calorimeter Spectrometer**

The resolution studies for HgTe absorbers found that it is reasonable to expect a full width half maximum resolution of 20 eV for thick HgTe absorbers. With this knowledge a measurement was done as part of the work for this dissertation, to test if the model was correct and if a thick HgTe absorber could give, in practice, a 20 eV FWHM energy resolution for high-energy photons.

During the development of the XRS satellite mission, there was a need to test

different doping characteristics for the thermistors. The GSFC team developed a platform for testing multiple types of thermistors at the same time. The technique involved using small ‘test dice’. The dice are single 1 mm x 1 mm silicon pieces onto which two XRS/EBIT style pixels have been manufactured. The test dice are then glued onto a board and wires are connected to the test dice. The board is then attached inside of the test dewar and the JFET and bias circuits are wired in. The number of electronics channels available in the test dewar system, which houses the cryogenics required to operate the detector at sub 100 mK temperatures, is 16 and thus 16 different pixels can be tested at once.

Using the test dice platform, a number of different thicknesses for the HgTe absorber was tested. A sheet of HgTe was manufactured from a several cm long by several cm wide by 500  $\mu\text{m}$  thick. From that sheet, pieces of HgTe that were 100 x 500 x 500  $\mu\text{m}$ , as well as pieces with the same 500 x 500  $\mu\text{m}$  cross sectional area but thicknesses of 200, 300, 400, and 500  $\mu\text{m}$ , were cut with a diamond tipped saw. The test dice were epoxied onto a PC board, which had 32 copper strips manufactured into it, and then the absorbers were epoxied onto the test dice. The copper strips provided an electrical conduit to connect the test dice to the detector electronics. A picture of the finished test array is shown in Fig. 3.8.

Because the XRS/EBIT thermistor pixels were only designed to handle 8  $\mu\text{m}$  thick HgTe, the increased weight of the absorber for absorbers over 100  $\mu\text{m}$  in thickness, proved too great for the pixels to support them as the silicon support structures buckled under the weight and the pixels broke. For this reason only one 200  $\mu\text{m}$  thick absorber pixel survived. This gave a realistic limit as to the size of the absorber that could be placed on the current

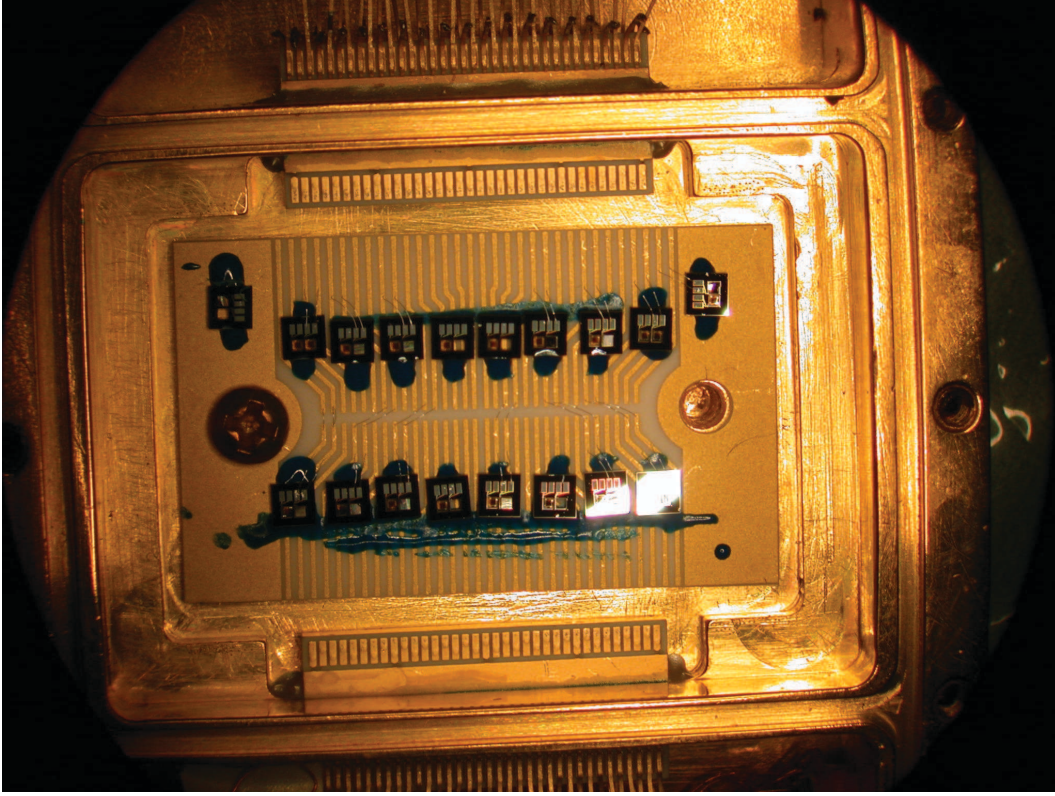


Figure 3.8: Magnified picture of test array. Each test die has two pixels. The absorbers are glued onto the test die. The wire bonds are from the test die pads to the PC board and finally to the detector assembly on top. Only 16 channels could be tested at one time in the test array.

design of the thermistor.

The PC board with the glued test dice was connected to the detector electronics and placed inside of a dewar system similar to that of the XRS/EBIT system. The test detector was run at a temperature of 50 mK by way of a pumped LHe dewar and an ADR similar to the one used in the XRS/EBIT spectrometer. A radioactive  $^{241}\text{Am}$  source was placed in front of the detector. The resolution of each of absorber in the test was determined by fitting the 60 keV  $\gamma$ -ray. Table 3.1 shows the results of resolutions that were measured for the various absorbers tested. Two of the 100  $\mu\text{m}$  thick HgTe pixels performed well and

Table of Thickness and Resolution	
Thickness ( $\mu\text{m}$ )	Resolution (eV)
8	5
32 (4 stack)	18
100	24
100	23
100	31
100	29
200	60

Table 3.1: Table of measured FWHM energy resolutions on the test detector.

gave FWHM energy resolutions of  $\sim 20$  eV. The worst FWHM energy resolution measured was from the 200  $\mu\text{m}$  thick pixel and the best was the control pixel, which was 8  $\mu\text{m}$  thick.

Because the test detector showed good results for the energy resolution for 60 keV photons, it was decided that a portion of a new calorimeter spectrometer that was going to be placed at EBIT be reserved for thick HgTe absorbers of 100  $\mu\text{m}$  in thickness.

### 3.6 ECS

The ECS or EBIT Calorimeter Spectrometer is a replacement for the XRS/EBIT calorimeter spectrometer. The ECS design is based on the XRS/EBIT and upgrades several parts of the XRS/EBIT. The main upgrades that the ECS has over the XRS/EBIT are a



longer run time (the ECS detector can stay at 50 mK longer than the XRS/EBIT), a longer lasting cryogen dewar (for the liquid helium and nitrogen), and thicker pixels to do high-energy x-ray work with.

### 3.6.1 Design

The ECS is an array of XRS/EBIT style thermistor based calorimeter pixels [57], in which half of the pixels have  $8 \times 624 \times 624 \mu\text{m}$  (thin) HgTe absorbers glued on the thermistors, and the other half<sup>9</sup> have  $114 \mu\text{m} \times 624 \mu\text{m} \times 500 \mu\text{m}$  (thick) HgTe absorbers glued on the thermistors<sup>10</sup>. The thick HgTe pixels are used for measuring x rays above 10 keV, as the quantum efficiency is higher than that of the  $8 \mu\text{m}$  thick absorbers (at 60 keV the QE for the thick pixels is  $\sim 30 \%$  and around a few % for the thin ones). The ECS (like the XRS/EBIT) is housed in a laboratory version of the XRS detector assembly [55] which includes the liquid helium and liquid nitrogen cryostats. The way in which the detector is readout as well as the operation of the ECS is the same as the XRS/EBIT. A picture of the array is shown in Fig. 3.9. The ECS operates at a temperature of 50 mK and is able to achieve a FWHM energy resolution of 4.5 eV at 6 keV for the thin ( $8 \mu\text{m}$ ) HgTe absorber pixels and  $\sim 30$  eV at 60 keV for thick ( $114 \mu\text{m}$ ) HgTe absorber pixels.

When compared to the XRS/EBIT, the two main improvements of the ECS stand out. The hold time of the ECS ADR magnet cycle is  $\sim 60$  hours at an operating temperature of 50 mK. This is considerably more than the XRS/EBIT ADR hold time of  $\sim 12$  hours at an operating temperature of 60 mK. The ECS cryogen dewar system (which holds the

---

<sup>9</sup>2 pixels were broken during manufacturing

<sup>10</sup>2 pixels have a cross sectional area of  $500 \mu\text{m}^2$

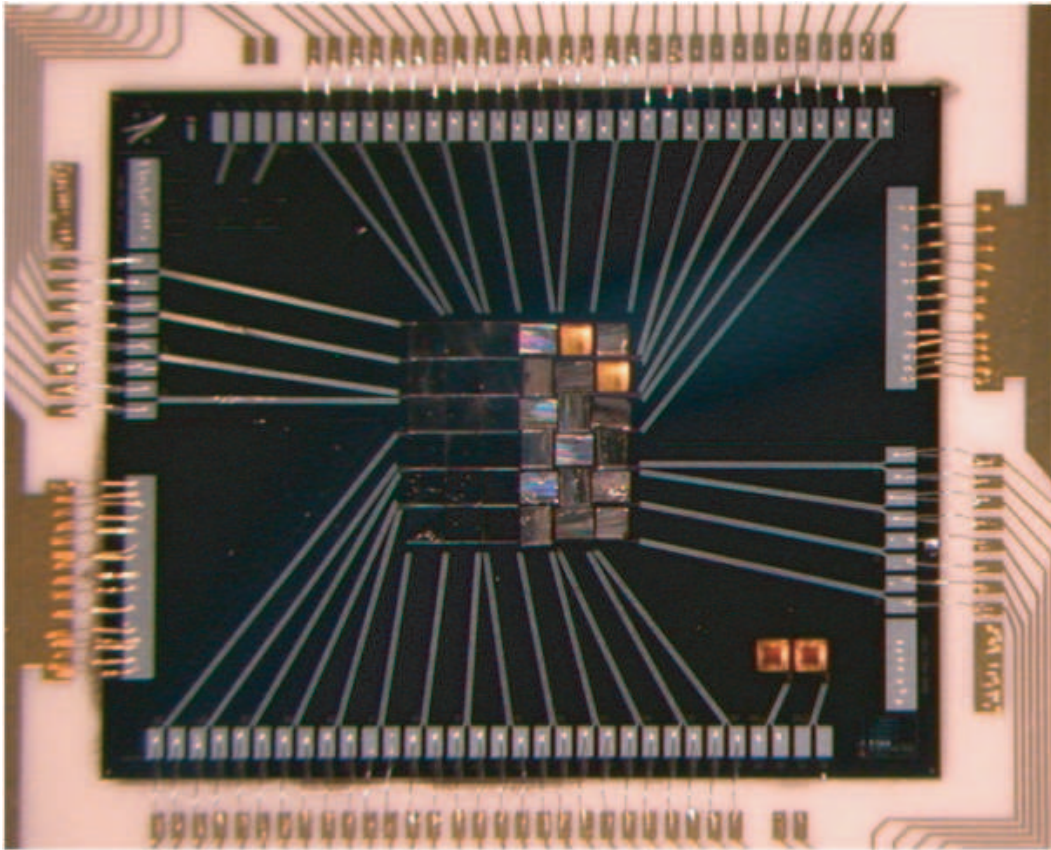


Figure 3.9: Picture of finished ECS array. High-energy pixels are to the right and low-energy pixels are to the left.

liquid helium and liquid nitrogen) is increased in size over system used on the XRS/EBIT detector. The increased size lengthens the time between refills of liquid helium (went to every two weeks on the ECS from every two days on the XRS/EBIT) and for liquid nitrogen (went from twice per day on the XRS/EBIT to every three days on the ECS).

The ADR (see section 3.3) in the ECS is able to maintain 50 mK for  $\sim 60$  hours, because of a larger salt pill and the lower starting temperature that the ADR cycle starts from. The salt pill is 50 % bigger in weight and as such there are 50 % more magnetic moments to soak up heat from the detector. For the XRS/EBIT detector, the ADR has to cool down to 60 mK from 1.5 K. The ECS only has to cool down from 350 mK which allows for more ADR magnet current to be used for maintaining the temperature of 50 mK.

The lower starting point for the ADR of 350 mK is achieved by the use of a  $^3\text{He}/^4\text{He}$  sorption pump. The basic principle of operation for the sorption pump, made by Chase Cryogenics, is that cooling is achieved by reducing the pressure on top of a container of liquid  $^3\text{He}$  by ‘pumping’ on it. The pump in the sorption pump is a piece of charcoal that absorbs helium gas when it is cold (cold is under 15 K).

The sorption pump is a system with two containers filled with helium gas. One of the containers is filled with  $^3\text{He}$  gas and the other is filled with  $^4\text{He}$  gas and in each container is a piece of charcoal. When warm, the charcoal does not absorb any helium gas and so at room temperature there is only gaseous helium contained in the pump system. The sorption pump is connected to the liquid helium dewar and so is cooled to 4.2 K (when at 4.2 K the helium gas will be absorbed into the charcoal piece). To operate the sorption pump, a heater which is attached to the piece of charcoal is turned on so that the helium gas is de-sorbed

out of the charcoal. At this point the  $^4\text{He}$  will condense. When the  $^4\text{He}$  has condensed the heater attached to the charcoal piece is turned off and the charcoal starts to absorb the  $^4\text{He}$  gas as it evaporates from the liquid  $^4\text{He}$ . The  $^4\text{He}$  will cool till roughly 850 mK. Once the sorption pump is below 2 K, a gas gap heat switch stops thermal conduction and the sorption pump is thermally isolated from the 4.2 K liquid helium dewar.  $^3\text{He}$  condenses at 1.2 K and once the pump system passes 1.2 K the  $^3\text{He}$  will condense. When the liquid  $^4\text{He}$  is exhausted, the heater for the  $^3\text{He}$  is turned off, and the temperature of the pump is then cooled down to 350 mK by evaporative cooling of the  $^3\text{He}$ . The sorption pump acts as the pre-cooler for the ADR and at some point during the sorption pump cooling process the ADR will start<sup>11</sup>.

The intended thickness of the thick pixels on the ECS was supposed to be 100  $\mu\text{m}$ . However, the manufacturing process which produced the thick absorbers was not as accurate as was hoped for, and a large discrepancy in terms of size of the absorbers was seen. Figure 3.10 shows a magnified view of the ECS array where it is possible to see the irregularities of the thick pixels. To find the thickness of the absorbers, absorbers were weighed and a cross sectional area of 500 x 624  $\mu\text{m}$  was assumed. Using the density of HgTe of 8.17 g/cm [58], an average thickness of  $114 \pm 9 \mu\text{m}$  was found.

### 3.7 Quantum Efficiency

For calorimeters, the quantum efficiency (QE) is the number of photons which deposit their energy in the absorber divided by the total number of photons incident on the

---

<sup>11</sup>The whole process is computer controlled and has been optimized (in terms of when each process starts) to yield the longest lasting 50 mK operation time.

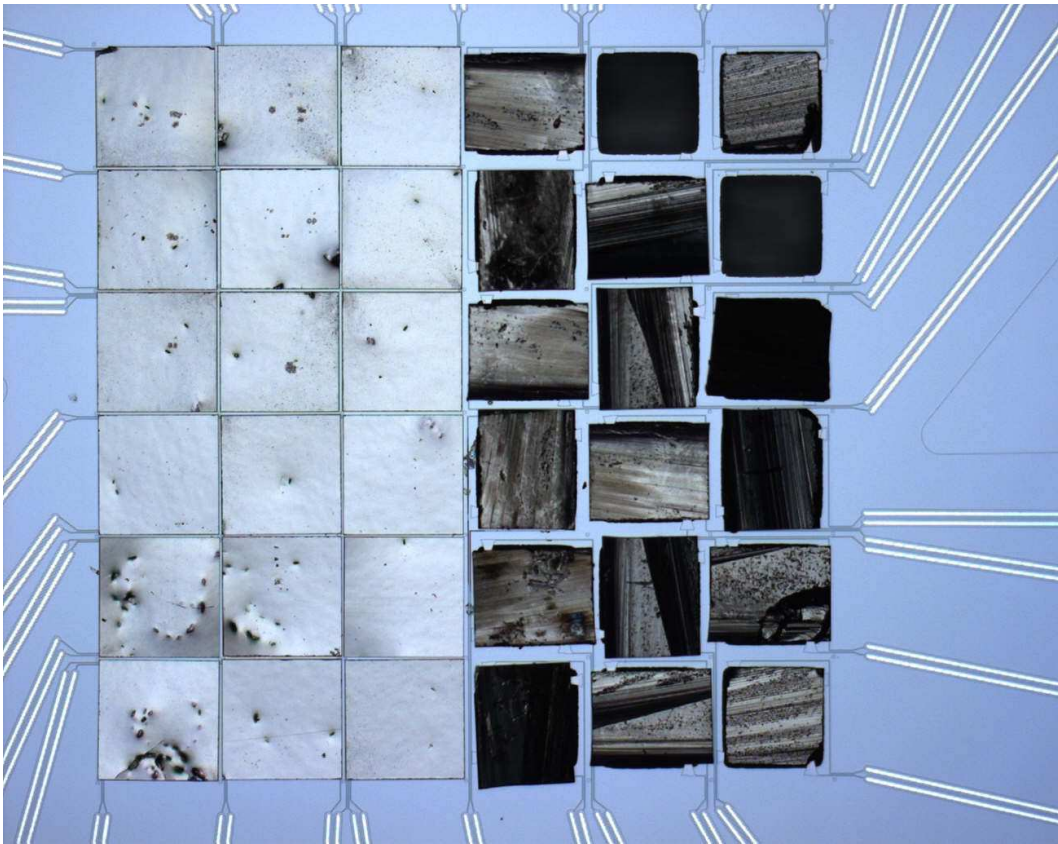


Figure 3.10: Magnified picture of finished ECS array. High-energy pixels are to the right and low-energy pixels are to the left.

absorber. The thicker the absorber the larger the QE. This is because the QE is dependent on the column density of electrons in the absorber. The cross section for photons to interact with matter decreases with increasing photon energy and as such it is harder to detect high-energy photons.

Experiments with photons and atoms have verified theoretical calculations of photoionization cross sections to an accuracy of roughly 3 %. Since absorption for photons under 100 keV is mostly due to the photoionization process, calculations of the QE (which are based on photoionization calculations) for energies under 100 keV are taken to be good to 3 %. As part of this dissertation the calculation of the QE for various absorbers was done.

The transmitted intensity of a beam of photons through a material of density,  $\rho$  (g/cm<sup>3</sup>), and thickness,  $d$ , is given by,

$$I = I_0 e^{-\mu \rho d}, \quad (3.8)$$

where  $\mu$  is the mass attenuation coefficient. For QE calculations, then, the absorbed intensity is  $1-I/I_0$ . The mass attenuation coefficient is related to the total atomic absorption cross section (dominated by the photoionization cross sections),  $\sigma_A$  (cm<sup>2</sup>/atom) by,

$$\mu = \frac{N_A}{A} \sigma_A, \quad (3.9)$$

where  $N_A$  is Avogadro's number and  $A$  is the atomic weight of the atom. For mixtures of materials the weighted average, according to atomic weight of the constituent atoms in the mixture, of the atomic cross sections is used.

The National Institute of Standards and Technology, NIST, provides a list of calculated attenuation coefficients to use in determining the QE of a material<sup>12</sup>. When using the mass attenuation coefficient (MAC) as calculated by NIST, the assumption is that if the incident photon interacts with matter in any way, the photon will not be transmitted and was thus absorbed. This is not quite the case as there are processes by which photons are not fully absorbed in a material. To account for possible energy loss processes, NIST also gives the mass energy-absorption coefficient. This coefficient is used in the same way as the MAC, but the value of the total absorption cross sections is lower as it takes into account any secondary photon emission processes (like a fluorescence photon) that cause energy to be lost from the absorbing material.

The main energy loss mechanism<sup>13</sup> that affects the absorption process is K-shell fluorescence emission. This happens when the photoelectron that is produced comes from the K-shell of an atom. The atom (where the photoelectron came from) is left with a K-shell vacancy, and one of the bound electrons lying in higher shells ( $n=2$  and above) will then radiatively decay to fill this vacancy. The photon that is produced can be high energy, as for Te the K-shell photon that is produced is on the order of 30 keV and for Hg it is on the order of 80 keV. If the photon does not interact with another atom in the absorber, then the energy of that photon has been lost. When this happens the calorimeter will only heat up to an energy of the incident photon energy minus the energy of the lost K-shell fluorescence photon<sup>14</sup>.

---

<sup>12</sup><http://physics.nist.gov/PhysRefData/XrayMassCoef/cover.html>

<sup>13</sup>Bremsstrahlung emission from high-energy photoelectrons can also cause energy loss. However, for photons under 100 keV this is not a big effect and is neglected here.

<sup>14</sup>This is called an escape peak.

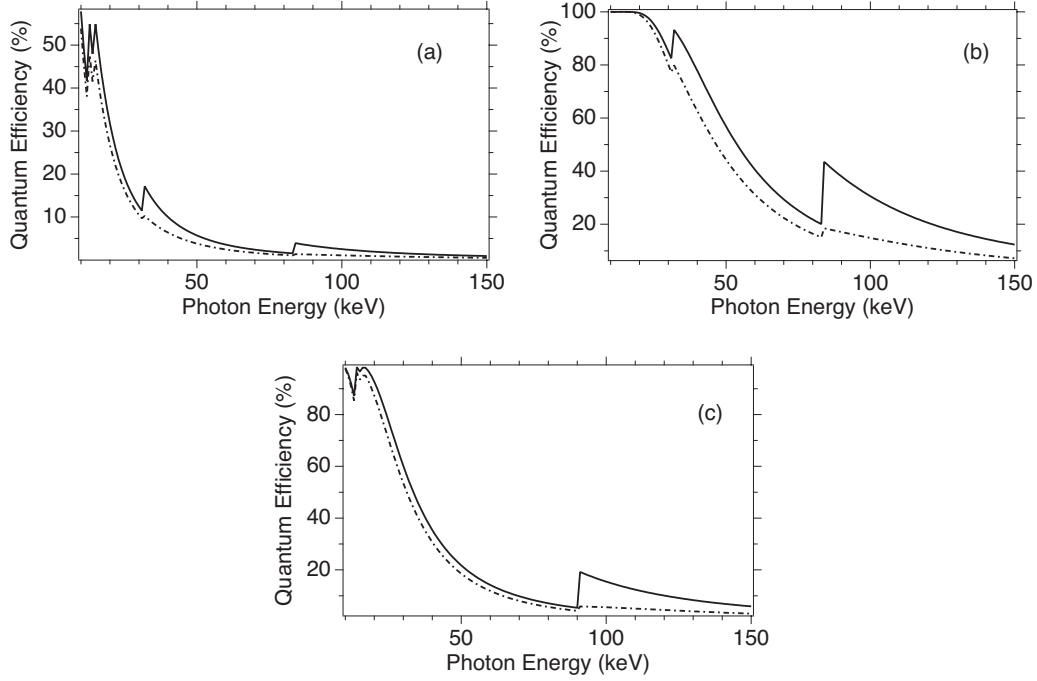


Figure 3.11: Plot of Quantum Efficiency for Photons from 10 keV to 150 keV. Solid line is calculation using MAC method and dashed-dotted line is calculation using MEAC method. Graph (a) is calculation of QE for a 8  $\mu\text{m}$  HgTe absorber. Graph (b) is calculation of QE for a 114  $\mu\text{m}$  HgTe absorber. Graph (c) is calculation of QE for a 30  $\mu\text{m}$  bismuth absorber.

The effect on the MEAC of florescence photons above the K-edges<sup>15</sup> for Te, Hg, Bi can be seen in the plots of the calculated quantum efficiency, shown in Fig. 3.11, for a 8  $\mu\text{m}$  thick HgTe absorber, a 114  $\mu\text{m}$  thick HgTe absorber, and a 30  $\mu\text{m}$  thick bismuth absorber. For the 30  $\mu\text{m}$  bismuth absorbers and the 8  $\mu\text{m}$  HgTe absorbers, in the photon energy band from 10 keV to 100 keV, use of both the MAC and MEAC coefficients yields similar results (except for energies above the emission of a florescence photon). However, above the K-edge of Te for the 8  $\mu\text{m}$  HgTe absorber and K-edge of bismuth for the 30  $\mu\text{m}$  thick bismuth absorber, the MEAC should be used exclusively, as the use of the MEAC is a better approximation.

<sup>15</sup>The K-edge is the binding energy of a K-shell electron.



For the 114  $\mu\text{m}$  HgTe absorber the QE calculated with the MAC, is roughly 20 % higher than the calculation of the QE using the MEAC once the energy of the incident photon has passed the K-edge of Te. This is due to the MEAC assuming all of the K-shell fluorescence photons are lost, whereas the MAC assumes none are lost. This is not a good approximation because the QE for a 30 keV photon (the energy of a Te K-shell x-ray photon) is around 80 %, and as such, it is expected that most of the fluorescence photons do not escape. However a certain fraction of fluorescence photons do escape the absorber, and thus, in the photon energy band from 30 keV to 80 keV, the calculation of the QE using the MAC overestimates the QE by a small margin and the calculation of the QE using the MEAC underestimates the absorption by a larger margin than the value obtained using the MAC.

To obtain a more accurate value for the QE for the 114  $\mu\text{m}$  HgTe absorber, than from using the method employing the MAC and MEAC, a calculation of the QE was done using a Monte Carlo photon transport code. The code used was the Integrated TIGER Series (ITS) [59]. ITS treats the incident photon, resultant photoelectron, and any resultant escape photons in a probabilistic way. If the incident photon creates a photoelectron, then the photoelectron is followed (by the code) through the material as it makes more electrons, and either is stopped and absorbed by the material, or leaves the material. The code also follows any fluorescence photon from the atom that was ionized and sees whether it leaves the material. Thus instead of either disregarding any secondary photon loss mechanisms like the calculation of the QE using the MAC does, or assuming all secondary photons leave the material like the calculation of the QE using the MEAC, it looks to see what actually

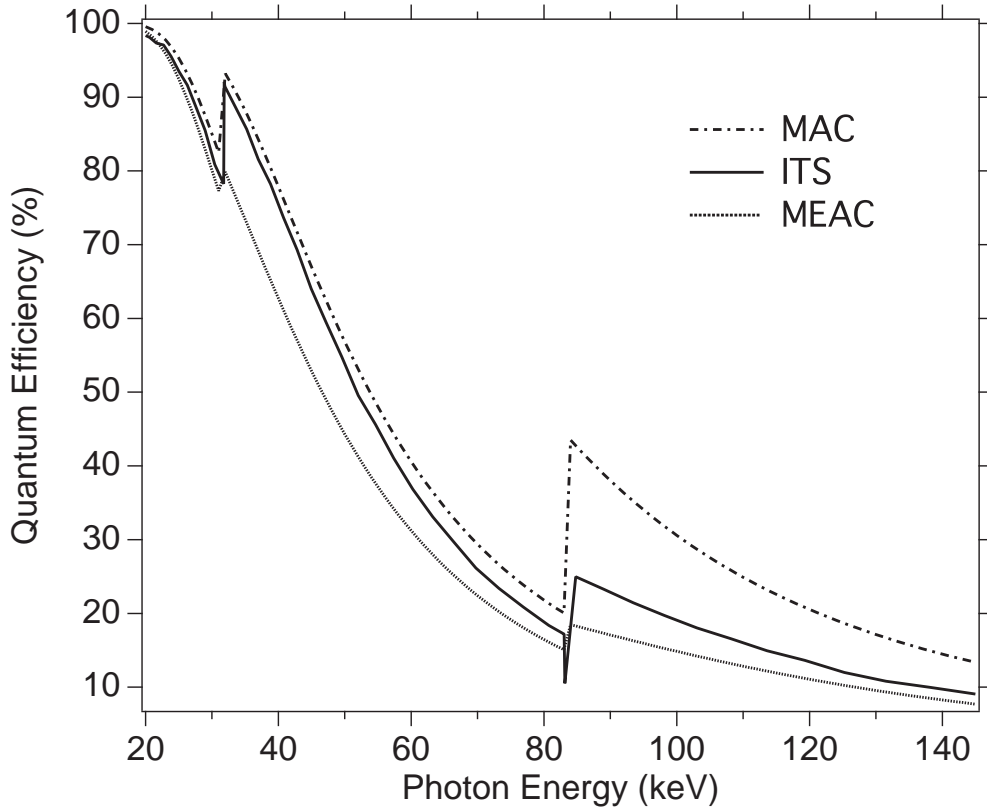


Figure 3.12: Plot of Quantum Efficiency for 114  $\mu\text{m}$  of HgTe for photons from 20 keV to 145 keV. Solid line is a calculation by the ITS code, the dashed-dotted line is a calculation using the MAC method, and the dotted line represents the calculation using the MEAC method. ITS result calculated by Daniel Hey [60].

happens and is therefore the most trusted way of calculating the QE of a material.

For a thickness of 114  $\mu\text{m}$  of HgTe the ITS code produces a QE curve similar to the QE calculated with the MAC at lower photons energies. At higher photon energies the ITS result starts to converge to the MEAC result. This is in line with predictions, as the QE calculated with the MEAC should be more accurate at higher photons energies than the QE calculated with the MAC. The result of the calculation is shown in Fig. 3.12, with the MAC and MEAC curves for comparison.

## Part II

# Measurements

## Chapter 4

# Measurement of Electron-Impact Excitation Cross Sections at High Electron Impact Energies for Hydrogenlike Iron and Nickel Ions

### 4.1 Introduction

Electron-impact excitation (EIE) cross sections of K-shell ions are used in interpreting the spectra from astrophysical and laboratory-produced high-temperature plasmas. Of special importance are K-shell cross sections of iron and nickel as they have relatively high elemental abundances in celestial sources as well as being present in many laboratory plasmas. In K-shell systems the cross section for EIE rises till roughly 3 times the threshold

energy. To construct a good model for high-Z K-shell emission from a high-temperature plasma, cross sections for electron energies up to 10 times threshold need to be included. Furthermore, for electron energies in excess of 100 keV relativistic effects are expected to play a role in the excitation process and modify the cross section [61]. Yet, for energies well above excitation threshold, no experimental data exist to benchmark and guide theory [32].

The emitted intensity of a direct excitation (DE) spectral line can be written as  $I = n_e n_i \langle v_e \sigma_{EIE} \rangle$ , where  $n_e$  is the density of electrons,  $n_i$  is the density of the ions,  $v_e$  is the velocity of the electrons, and  $\sigma_{EIE}$  is the electron-impact excitation cross section. The difficulty in making EIE measurements comes from the uncertainty in the knowledge of the density of the ions and electrons. However with a source that is mono-energetic there exists a way by which to remove the influence of the uncertain terms. That is by normalizing the direct excitation cross section to the cross section for radiative recombination since radiative recombination can be calculated to a much greater accuracy.

Radiative recombination (RR) is produced by the capture of an electron into a vacant atomic level. The photon that is produced has the energy of the binding energy of the atomic level plus the energy of the free electron. The mathematical expression for the intensity of a RR spectral feature has the same form as for EIE,  $I = n_e n_i \langle v_e \sigma_{RR} \rangle$ . Dividing the intensity of a given line from the EIE spectrum by that of a feature produced by RR forms a ratio of the two cross sections, and the terms with large uncertainties cancel out, leaving the EIE cross section related to the radiative recombination cross section (which in turn is calculated to an accuracy of 3 %).

## 4.2 Experiment

Hydrogenlike iron ions were produced by a 35, 65, and 75 keV energy electron beam and the nickel ions were produced by a 65 and 85 keV energy electron beam in the SuperEBIT electron beam ion trap. The iron and nickel atoms were injected as metallo-organic gases (nickelocene and iron pentacarbonyl) by way of a ballistic gas injector. The hydrogenlike spectrum from the two elements was observed at  $90^\circ$  with a 6 mm thick coaxial EG&G IGLET-X high purity germanium detector and by the XRS/EBIT x-ray microcalorimeter spectrometer [53].

For iron and nickel, the K-shell radiative recombination spectrum sits roughly 10 keV higher in energy than the electron beam energy. The XRS/EBIT, which has a 6 eV full width half maximum resolution at 6 keV, has a low quantum efficiency (QE) at these high energies, and thus, cannot observe the RR spectrum (which is already 100 times less intense than the EIE emission). For that reason, the IGLET was used, as the QE of the Ge detector is above 85 % for photons under 100 keV<sup>1</sup>. On the other hand, the Ge detector cannot resolve the DE hydrogenlike emission because of its poor resolution (roughly 200 eV at 6 keV). Thus a hybrid measurement system was used, whereby the K-shell emission was recorded with both the Ge detector and the XRS/EBIT, but only the Ge detector recorded the RR spectrum, as shown in Figs. 4.1 and 4.2.

In the setup the XRS/EBIT is used to resolve the K-shell spectrum, and to relate the number of counts in the Lyman- $\alpha_1$  and Lyman- $\alpha_2$  lines to the intensity of the single spectral feature observed with the Ge detector, see Fig. 4.2. The Ge detector spectrum (as

---

<sup>1</sup>The absorption percentage was calculated using the mass attenuation coefficient taken from NIST <http://physics.nist.gov/PhysRefData/XrayMassCoef/cover.html>.

shown in Fig. 4.1), then, with the proper weightings of the lines, is used as the basis of the RR normalization. This allows for elimination of systematic error due to uncertainty in the geometry of the experimental setup. The spectral peaks recorded with both detectors are fit with Gaussian fitting functions. This procedure is similar to that employed in [62] except that we employ the XRS/EBIT instead of a crystal spectrometer.

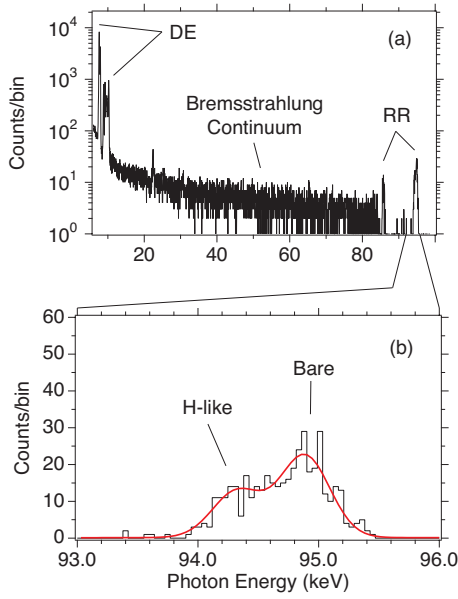


Figure 4.1: Graph (a) is the spectrum recorded with the IGLET for nickel at an electron beam energy of 85 keV. The DE spectrum as well as the L-shell and K-shell RR features are seen. Graph (b) is the K-shell RR peaks for hydrogenlike and bare nickel at 85 keV. The fit to the RR is shown in red.

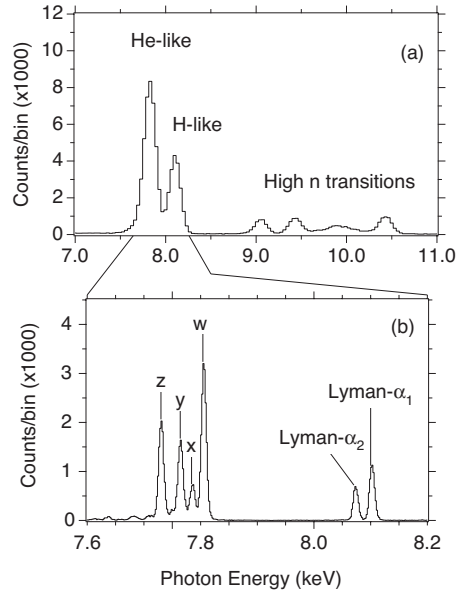


Figure 4.2: K-shell spectrum of nickel at an electron beam energy of 85 keV. Graph (a) is the spectrum recorded with the IGLET. Graph (b) is the spectrum recorded with the XRS/EBIT. The heliumlike charge state is labeled according to [63].

In EBIT there are several processes that modify the intensity of the observed Lyman- $\alpha$  lines. These processes are polarization, cascades from higher levels, and charge exchange<sup>2</sup>. Polarization, affects the geometric emission of photons for Lyman- $\alpha_1$ , which

<sup>2</sup>RR capture into the  $n=2$  shell can also affect the emission but the cross section is weaker as compared to the EIE cross sections by over a factor of 100, and thus, is not considered.

is important for relating the differential cross section (at  $90^\circ$ ) to the total cross section for comparison to theory. Cascades can produce extra Lyman- $\alpha_1$  photons by the decay of higher lying atomic levels (like the  $n=3$  level) down to the  $n=2$  level, which, if not taken into account would cause the experiment to measure a larger cross section. Charge exchange occurs when a neutral atom is stripped of one of its valence electrons. The electron is captured into a high lying level, which may cascade down, and possibly make a Lyman- $\alpha_1$  photon. To take into account polarization and cascades, calculations were made with the Flexible Atomic Code [64] (FAC) to adjust the data. Since the contribution to the Lyman- $\alpha_1$  line for cascades and polarization is less than 10 % (using an estimated uncertainty of 20 %) the effect of including calculations only minimally affects the end result. It is estimated that charge exchange affects the intensity of Lyman- $\alpha_1$  on the order of a few %<sup>3</sup>. Even with a possible order of magnitude uncertainty in the neutral density and the collision energy, the effect is still small, and as such, is not included in the analysis.

When taking into account the absorption percentage for RR photons, cascade, and polarization modifications to the DE, the formula for obtaining the EIE cross section takes the form,

$$\sigma_{EIE} = \frac{I_{DE}}{I_{RR}} \sigma_{RR} A_{RR} G(E), \quad (4.1)$$

where  $\sigma_{EIE}$  is the cross section for EIE,  $\sigma_{RR}$  is the calculated cross section for RR,  $I_{DE}$  is the number of counts in the DE line,  $I_{RR}$  is the number of counts observed in the RR peak,

---

<sup>3</sup>The cross section for charge exchange is estimated as the ion charge times  $10^{-15} \text{ cm}^2$ , the ion collision energy is estimated as 10 eV/amu, and the neutral density is around  $3 \cdot 10^6 \text{ cm}^{-3}$ . Compared with the EIE cross section for Lyman- $\alpha_1$  of  $10^{-22} \text{ cm}^2$ , the electron collision energy of 35 keV to 85 keV, and the electron density around  $5 \cdot 10^{11} \text{ cm}^{-3}$ .



$A_{RR}$  is the absorption percentage for the RR photon and  $G(E)$  is a factor that relates to the polarization and cascade contributions.

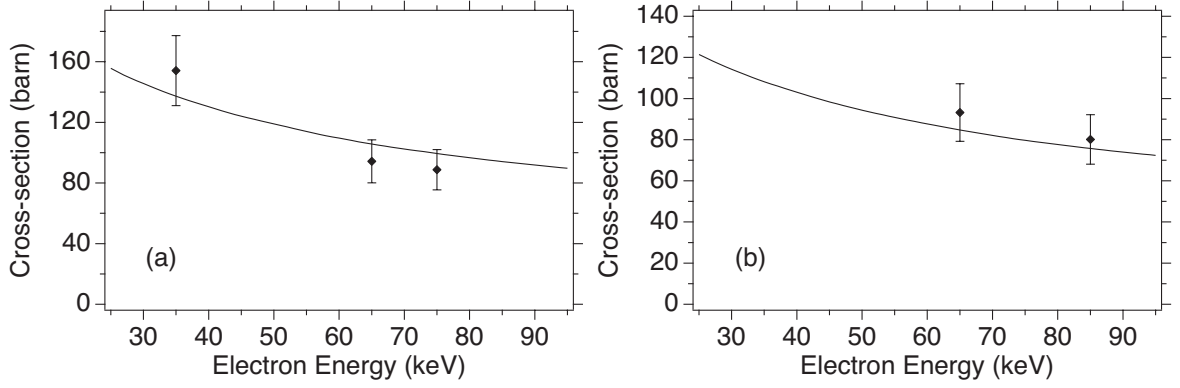


Figure 4.3: Experimental electron-impact excitation cross sections for the Lyman- $\alpha_1$  line in hydrogenlike iron and nickel. Graph (a) represents the measured cross sections for iron at energies of 35 keV, 65 keV and 75 keV. Graph (b) represents measured cross sections for nickel at energies of 65 keV and 85 keV. The solid line is calculated by FAC.

The EIE cross sections were obtained by dividing the number of counts recorded in the hydrogenlike Lyman- $\alpha_1$  line in the IGLET detector (with proper weightings as recorded in the XRS/EBIT) by the number of counts in the hydrogenlike RR peak, seen only in the IGLET. Figure 4.3 lists the cross sections for the various energies for both nickel and iron ions and compared to FAC calculations. Each point is the average of several measurements (except for the 35 keV and 75 keV measurements done with iron). The 15 % error bars are dominated by the approximately 10% statistical error associated with the determination of the number of counts in the RR spectrum and take into account the uncertainty in the calculation of the cascades, polarization and absorption percentage. Table 4.1 shows the results of the measurement.

EIE Cross Sections			
Element	Energy (keV)	Measurement (barn)	FAC (barn)
Fe	35	$154.1 \pm 23.1$	137.27
Fe	65	$94.3 \pm 14.1$	105.68
Fe	75	$88.8 \pm 13.3$	99.46
Ni	65	$93.2 \pm 14.0$	84.68
Ni	85	$80.1 \pm 12.0$	75.70

Table 4.1: Experimental cross sections for electron-impact-excitation of the Lyman- $\alpha_1$  line in hydrogenlike iron and nickel ions. Experimental values are compared to calculations by FAC.

### 4.3 Conclusion

The cross sections measured here are the highest-energy cross sections that have been measured for a high-Z hydrogenlike ion. The results show that for the hydrogenlike ion, theory at high electron energies agrees well with experiment to roughly the 15 % level. Future studies will include a focus on heliumlike ions and go to higher-Z elements where QED effects become significant in the calculations of electron-impact excitation cross sections [40]. Furthermore, it should be noted, that the use of the ECS to measure both the RR spectrum as well as the DE spectrum, negates the need for use of a Ge detector as it has good QE for photons under 100 keV [57].

## Chapter 5

# The First Results of High-Z K-shell Spectra Recorded with Calorimeters

As a first step towards making high-resolution measurements with high-Z ions, the K-shell spectrum of highly charged praseodymium was measured with the XRS/EBIT calorimeter array.

### 5.1 Praseodymium with Bismuth Absorbers

The XRS/EBIT quantum microcalorimeter (as described in Section 3.3) is an x-ray calorimeter spectrometer array consisting of thirty two  $624\text{ }\mu\text{m} \times 624\text{ }\mu\text{m} \times 8\text{ }\mu\text{m}$  mercury-telluride (HgTe) absorber pixels, and four  $624\text{ }\mu\text{m} \times 624\text{ }\mu\text{m} \times 30\text{ }\mu\text{m}$  bismuth absorber pixels attached to doped silicon thermistors [53]. The XRS/EBIT was originally designed

as a hybrid array, with both low energy x-ray spectroscopy work (under 10 keV), and high-energy work to be performed on the same array. The low energy work to be performed with the HgTe pixels and the high-energy work to be performed with the bismuth pixels. The four bismuth pixels, of which only three work, do not have as high of a resolving power as the HgTe pixels. The best bismuth pixel has a FWHM energy resolution of 75 eV and the other two have FWHM energy resolutions of 150 eV each. For the purpose of obtaining the best possible spectrum, only the data from the highest resolution bismuth pixel is considered.

The bismuth pixels have a higher quantum efficiency for hard x rays as compared to the 8  $\mu\text{m}$  HgTe pixels. Knowing the QE for the pixels is important for making estimates as to the length of time required to do a measurement as well as for when measuring line intensities as the absolute QE for the detector will affect the observed intensity. For this reason, an experimental determination of the quantum efficiency of the bismuth absorber pixel was made relative to the HPGe detector, which has a quantum efficiency of 100 percent at 37 keV. The measured quantum efficiency of the high energy pixel at 37 keV is close to 40 % as shown in Fig. 5.1. This agreed with the theoretical calculation based on the thickness of the bismuth. For comparison to theory we used the mass-energy absorption coefficient [65].

The measurement was carried out at the Livermore SuperEBIT electron beam ion trap [27]. Neutral Pr was injected into the trap using a laser ablation injection system [66]. The electron beam current was varied from 140-160 mA, and the electron beam energy was set at 116 keV. The beam and trapping conditions created a plasma of mainly heliumlike and lithiumlike praseodymium with a small amount of berylliumlike praseodymium.

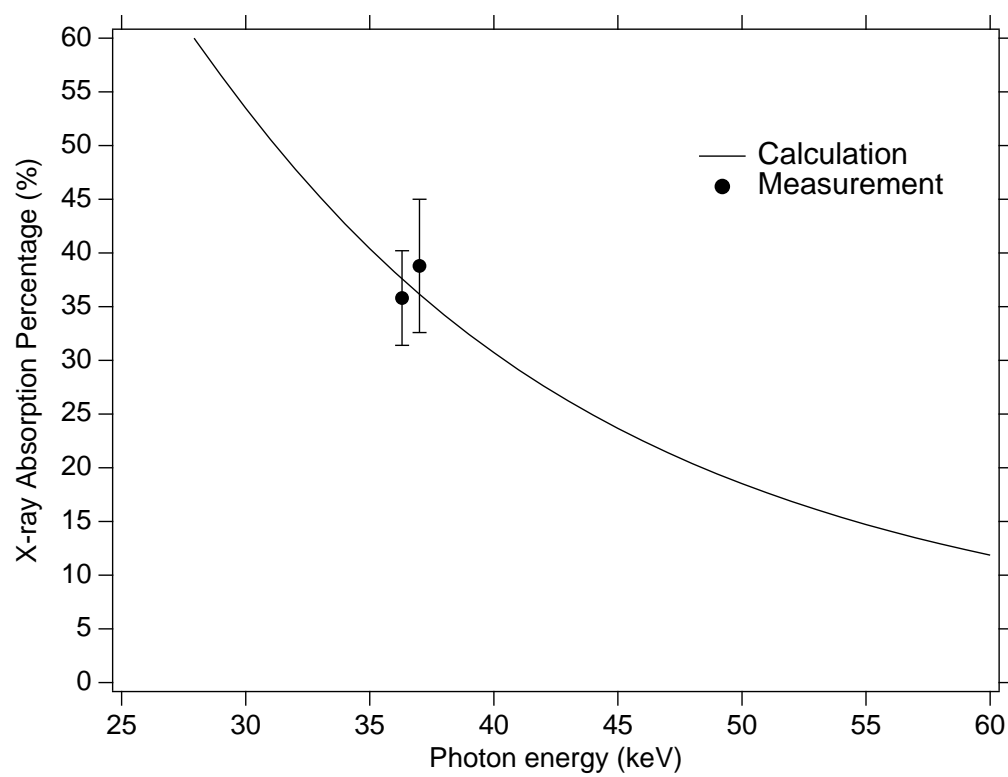


Figure 5.1: The quantum efficiency of a 30  $\mu m$  bismuth absorber .

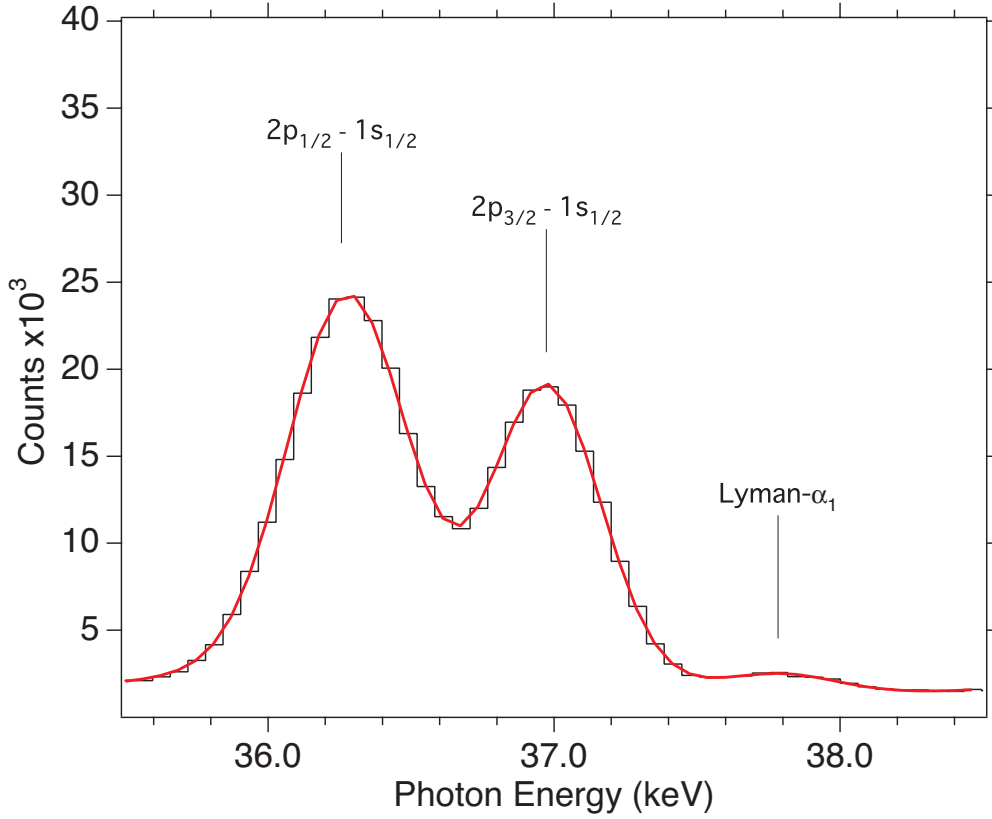


Figure 5.2: K-shell spectrum of highly charged Pr ions obtained with the IGLET-X detector.

Two detectors were used in the measurement: A High Purity Germanium detector (HPGe detector) and the XRS/EBIT. The HPGe detector used was an Ortec EG&G IGLET-X detector (IGLET). It was used to monitor the trap conditions, as the high QE makes for quick determination of the relative charge balances in the trap as well as other contaminant ions. From the analysis of the IGLET spectrum, a signature of hydrogenlike praseodymium was seen. The spectrum obtained with the Ge detector is shown in Fig. 5.2.

The data, from the highest resolving power bismuth pixel, was collected over a period of 40 hours, and was comprised of 4 individual data sets. Each data set was added together to obtain better statistics. The data, along with a fit produced by applying Gaus-

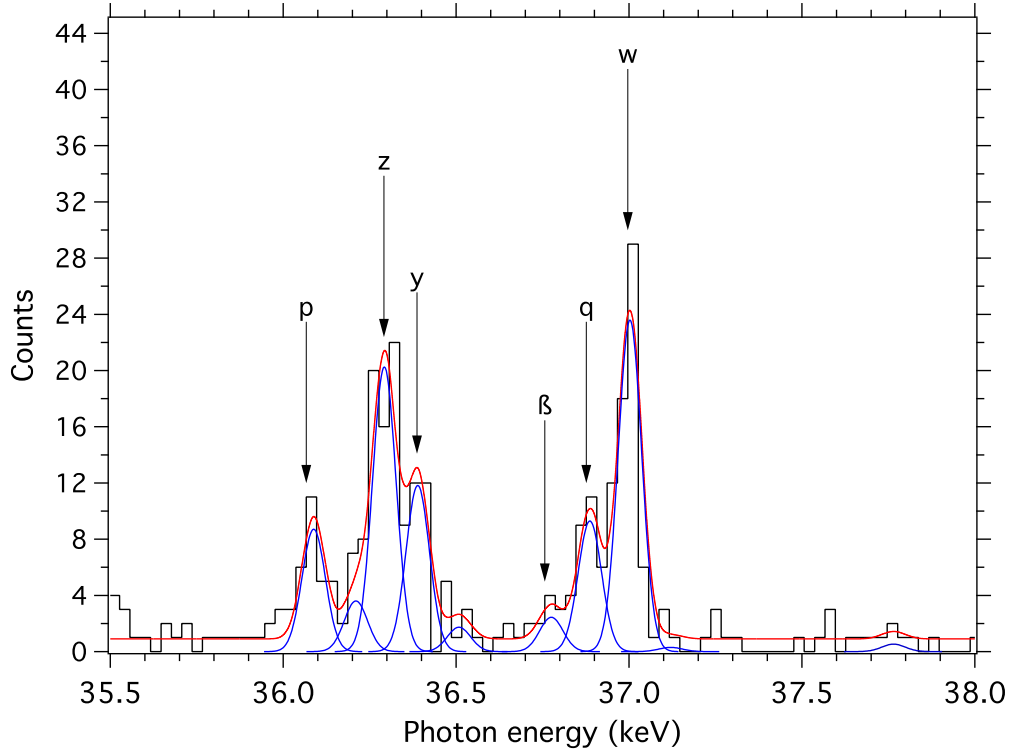


Figure 5.3: The first high-resolution spectrum of heliumlike through berylliumlike praseodymium. The heliumlike and lithiumlike lines w, q, y, z and p are labeled as according to [63]; the berylliumlike line  $\beta$  is labeled according to [68].

sian fitting functions to the data, is shown in Fig. 5.3. There was no external calibration (such as a radioactive source) for the microcalorimeter, so the strongest lines in the spectrum were used as an in-situ calibration. We took the theoretically accepted values of Drake's [67] calculations for the heliumlike system and used the resonance line, w at  $37002.7 \text{ eV}$ , and the forbidden line, z at  $36292.4 \text{ eV}$ , as the calibration. A linear fit of the line positions was used for establishing the energy scale.

As a test of the calibration, a measurement of the intercombination line, y, was made. The intercombination line, according to Drake, has a value of  $36390.4 \text{ eV}$ . Our measured value of  $36389.1 \pm 6.8 \text{ eV}$  agrees with the theoretical value within the limits of

the experimental uncertainty.

### 5.1.1 Transition Energies

The resolving power of the high energy pixel can be seen when compared with the spectrum taken with the Ge detector. In the Ge detector spectrum there are only 3 features visible. They are grouped into transitions to the ground state of heliumlike through berylliumlike praseodymium from the first excited levels where the total angular momentum,  $J$ , takes the values  $3/2 \hbar$  and  $1/2 \hbar$  and the Lyman- $\alpha_1$  transition in the hydrogenlike charge state is seen highest in energy. In the calorimeter spectrum the individual transitions of each charge state can clearly be seen.

The increased spectral resolution afforded by using the calorimeter allows a comparison to theory for the transition energies of the various charge states. Calculations for the heliumlike through berylliumlike charge states were provided by Mau Chen [69]. Calculations from the Flexible Atomic Code [64] were also made. Table 5.1 shows the experimental values obtained for the various spectral features by fitting the spectrum in reference to the calibration lines.

Transition energies of  $36886.8 \pm 8.5 \text{ eV}$  for the lithiumlike satellite q,  $1s2s2p \ ^2P_{3/2} \rightarrow 1s^22s \ ^1S_{1/2}$ ,  $36088.2 \pm 8.5 \text{ eV}$  for the lithiumlike satellite p,  $1s2s^2 \ ^2S_{1/2} \rightarrow 1s^22p \ ^2P_{1/2}$ , and  $36775 \pm 31 \text{ eV}$  for the berylliumlike satellite  $\beta$ ,  $1s2s^22p \ ^1P_1 \rightarrow 1s^22s^2 \ ^1S_0$  were obtained. As expected the best agreement was seen with the more highly charged heliumlike and lithiumlike species. The main source of error in the determination of the energies was due to statistics. This can be seen as the heliumlike line, y, is closer to the value<sup>1</sup> than the

---

<sup>1</sup>Since the calibration was done relative to Drake's w and z values, it is expected that line y be reproduced



K-shell Transition Energies of Highly Charged Pr Ions

Label	Transition	Energy (eV)	Chen <sup>a</sup> (eV)	FAC <sup>b</sup> (eV)	Drake <sup>c</sup>
w <sup>d</sup>	1s2p <sup>1</sup> P <sub>1</sub> → 1s <sup>2</sup> <sup>1</sup> S <sub>0</sub>	37002.7	-	-	37002.7
q	1s2s2p <sup>2</sup> P <sub>3/2</sub> → 1s <sup>2</sup> 2s <sup>1</sup> S <sub>1/2</sub>	36886.8 ± 8.5	36880.35	36877.39	-
β	1s2s <sup>2</sup> 2p <sup>1</sup> P <sub>1</sub> → 1s <sup>2</sup> 2s <sup>2</sup> <sup>1</sup> S <sub>0</sub>	36775 ± 31	36802.71	36798.39	-
y	1s2p <sup>3</sup> P <sub>1</sub> → 1s <sup>2</sup> <sup>1</sup> S <sub>0</sub>	36389.1 ± 6.8	-	-	36390.4
z <sup>d</sup>	1s2p <sup>3</sup> S <sub>1</sub> → 1s <sup>2</sup> <sup>1</sup> S <sub>0</sub>	36292.4	-	-	36292.4
p	1s2s <sup>2</sup> <sup>2</sup> S <sub>1/2</sub> → 1s <sup>2</sup> 2p <sup>2</sup> P <sub>1/2</sub>	36088.2 ± 8.5	36089.01	36085.80	-

<sup>a</sup> theoretical values from M. Chen [69]

<sup>b</sup> theoretical values from Flexible Atomic Code

<sup>c</sup> theoretical values from G. W. Drake [67]

<sup>d</sup> reference line from G. W. Drake [67]

Table 5.1: Measured transition energies of heliumlike through lithiumlike praseodymium. The experimental values are compared to several theories.

limits of uncertainty.

### 5.1.2 Discussion

The spectrum in Fig. 5.3 is striking when compared to the Ge detector spectrum in Fig. 5.2. Only three spectral features can be seen in the Ge detector spectrum versus the eight seen in the XRS/EBIT spectrum. This measurement is the first of its kind for such a high-Z ion to be measured with such high-resolution. The result highlights calorimeter's untapped potential to push forward to development of high-Z K-shell spectroscopy.

## 5.2 Praseodymium with Thin HgTe pixels

Although the quantum efficiency of a single  $8\ \mu\text{m}$  HgTe absorber pixel for 37 keV photons is under 10 %, if the K-shell spectrum of Pr is recorded with the entire array of  $8\ \mu\text{m}$  pixels, then the effective quantum efficiency of the spectrometer is large enough to be able to make a statistically relevant measurement. For 37 keV photons, the effective  $\text{QE}^2$  of one bismuth absorber pixel on the XRS/EBIT array is approximately equal to the effective QE of four  $8\ \mu\text{m}$  HgTe pixels. Thus by using a large number of  $8\ \mu\text{m}$  HgTe pixels on the XRS/EBIT array, the effective QE for a measurement of the K-shell spectrum of highly charge Pr ions would be able to be increased by a factor of five over the use of a single bismuth absorber.

However, when the XRS/EBIT array is operated at a temperature of 60 mK (as

---

by the measurement. This is because each theoretical calculation can contain shifts by including or missing a certain term in the theory. This will lead to a shift that, at first order, will simply shift all of the spectral lines, relative to the real value and other theories, by a linear amount. This can be seen in Table 5.1 as the values from FAC are similar to Drake's values but just shifted down in energy by roughly 3 eV.

<sup>2</sup>effective QE is defined as the total number of photons absorbed for a given detector.

was done for the measurement of the EIE cross sections in iron and nickel), 10 keV x rays produce voltage pulses on the order of 10 V (after the 20000 times amplification). For x rays with energy in excess of 10 keV, the voltage pulse that is recorded is clipped. Thus, when the XRS/EBIT array is operated at its nominal temperature (of 60 mK), a measurement of the K-shell spectrum of praseodymium cannot take place. However, if the temperature of the calorimeter is increased, the heat capacity also increases<sup>3</sup>, and the bandwidth with which the calorimeter can detect increases, as the voltage pulse resultant from an x-ray absorption event is proportional to the energy of the photon divided by the heat capacity of the calorimeter. Thus, to be able to detect 37 keV x rays, without having the voltage pulses from K-shell x-ray absorption events being clipped, the operating temperature of the XRS/EBIT array must be raised from 60 mK.

By raising the temperature that the array is operated at, the FWHM resolution is degraded. However at the operating temperature of 100 mK, the FWHM resolution is  $\sim 37$  eV, which is still a factor of two better than was seen with the bismuth absorber. This degradation in FWHM resolution is a consequence of increasing the heat capacity of the absorber, which creates a larger thermodynamic fluctuation term, as well as increasing the amount of time it takes for the weak thermal link to remove heat from the absorber (which means that the optimal filter will have fewer frequency bins to use<sup>4</sup>). Using this method (of raising the operating temperature of the XRS/EBIT array), a measurement of the K-shell spectrum of highly charged Pr ions was performed.

---

<sup>3</sup>As the heat capacity scales as  $T^3$  assuming only interacting phonons.

<sup>4</sup>see section 3.1.1 as well as section 3.2.3.

### 5.2.1 Measurement of K-shell Spectra from High-Z Highly Charged Ions

Each calorimeter pixel is a separate spectrometer. The data that are outputted from the calorimeter digital processor is in units of pulse height Volts, and each x-ray absorption event is time tagged so there is a time history of each photon. A spectrum is created by making a histogram, in time, of the pulse height data. This creates a spectrum which has y-axis units of counts and x-axis units of pulse height Volts. To measure the energy of a spectral line contained in a spectrum, the spectral line is fit with a fitting function (usually a Gaussian) and then the value of the centroid (in Volts) is converted into photon energy in eV. This conversion is done by finding a calibration curve for the histogram which relates the value of the Volts in the spectrum to a value in eV. If only one pixel is used, as in the measurement of the K-shell spectrum of Pr done with the bismuth pixel, then only one calibration curve needs to be found. If the spectrometer does not drift, so that the centroid of a spectral line taken at two different times have the same value in pulse height, then the calibration curve can be found once, and applied for all time. If the spectrometer does drift, then the calibration will have to be redone at regular intervals.

However, if many spectra are to be added together, then a calibration curve for each pixel needs to be found. Since, the pulse height values for the XRS/EBIT, and calorimeters in general, will drift over time, keeping the spectrometer in calibration over a long measurement time requires having strong spectral features recorded in each spectrum. Because of the weak K-shell x-ray flux from high-Z ions in SuperEBIT, no strong spectral features are able to be seen in each pixel's spectrum, and thus to make measurements of K-shell spectra from high-Z highly charged ions from SuperEBIT (or any low flux source), calibration lines

from some other x-ray source besides SuperEBIT needs to be seen in each spectrum. In the 10 to 60 keV x-ray range,  $^{241}\text{Am}$  is a common calibration source to use.  $^{241}\text{Am}$  has a plethora of nuclear decay  $\gamma$ -ray lines and neutral neptunium L-shell lines from 10 keV to 60 keV. If the measurement spans several days (as is often the case for measurements on SuperEBIT), then calibration is to take place usually in the morning and at night. The reason for this is that if there is a drift during the day when the K-shell data are being recorded, having a calibration spectrum before and after the drift occurred will allow the data to be adjusted. The addition of the spectra is then done with the aid of a computer algorithm, which also looks for any drifts in the centroids of the calibration lines. If any drifts are found, the data between the two points is corrected by a linear interpolation.

### 5.2.2 Experiment

The K-shell spectrum of praseodymium was recorded with the HgTe pixels on the XRS/EBIT array running at an operating temperature of 100 mK. The praseodymium was injected into SuperEBIT by a laser ablation system [66]. The electron beam energy was set to an energy of 127 keV. The photons emitted from SuperEBIT and recorded by the XRS/EBIT had to traverse two 5 mil beryllium windows that were used to hold off a 5 cm air gap. This air gap made it possible to insert a radioactive calibration source in front of the XRS/EBIT. The spectrum, which is the addition of  $\sim 80$  hours of data from twenty-two of the highest-FWHM-resolution HgTe pixels, from the XRS/EBIT microcalorimeter is shown in Fig. 5.4.

The spectrum in Fig. 5.4 is an addition of 8 days of data where Pr K-shell data was recorded for approximately 10 hours/day. The rest of the time was devoted to the

calibration of the calorimeter array using a radioactive  $^{241}\text{Am}$  source. For each day,  $^{241}\text{Am}$  calibration was done for 3 hours before Pr K-shell data was recorded. After the initial  $^{241}\text{Am}$  calibration, K-shell x-ray data were recorded for about 4 hours, and then another hour of  $^{241}\text{Am}$  calibration was performed. After the second calibration with  $^{241}\text{Am}$ , Pr K-shell data was recorded again until the day was over. The  $^{241}\text{Am}$  source was then placed in front of the XRS/EBIT and left in overnight to accumulate good statistics. The spectrum in Fig. 5.4 was also corrected for pulse height drift across any one day. Small intraday drifts in the pulse heights of the calibration lines were seen, and the Pr K-shell data was corrected accordingly. The drifts were associated with the temperature variation in the LHe tank<sup>5</sup>.

### 5.2.3 Transition Energies

To determine the transition energies for the lines shown in Fig. 5.4, the calibration curve for the spectrum must be found. As shown in Fig. 3.6, 8  $\mu\text{m}$  thick HgTe pixels start to exhibit marked non-linear pulse height response with increasing absorbed photon energy. This means that to determine the energy scale of the spectrum recorded with the 8  $\mu\text{m}$  pixels on the XRS/EBIT requires using a non-linear calibration function. Pr K-shell emission sits at roughly 37 keV, and the closest (in energy) calibration lines from the  $^{241}\text{Am}$  source are at 33 keV and 43 keV. Because of the non-linear calibration function, and the fact that there are no calibration lines in the vicinity of the Pr K-shell spectrum, there was a large uncertainty in the functional form of the calibration curve. Thus, precise determination of the transition energies of K-shell transitions in highly charged Pr was

---

<sup>5</sup>The thermometer that the ADR uses to keep track of the temperature of the array sits far away from the actual detector. Because of this drifts are possible. The ECS does not suffer from this at all and in fact no drifts have been seen with it.

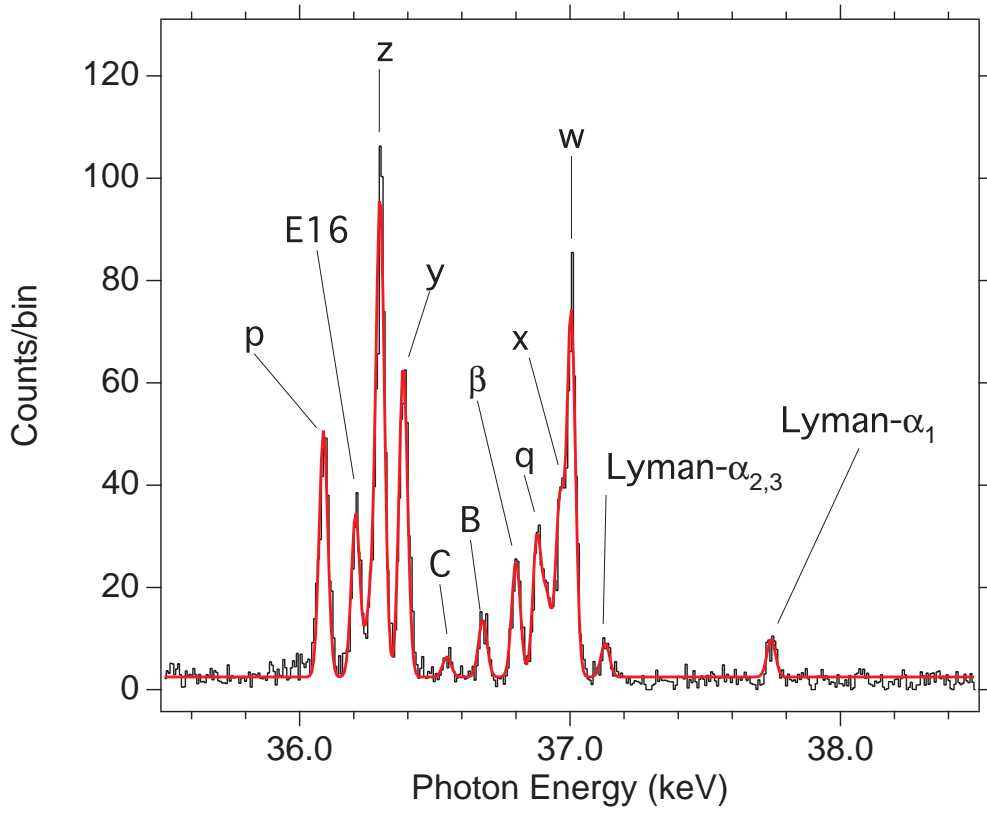


Figure 5.4: Quantum microcalorimeter spectrum of hydrogenlike through carbonlike praseodymium taken at an electron beam energy of 127 keV. Only the strongest lines are identified. The hydrogenlike lines are labeled as Lyman- $\alpha_{1-3}$ ; the heliumlike and lithiumlike lines w, s, t, q, r, y, z are labeled as according to [63]; the berylliumlike lines  $\beta$  and E16 are labeled according to [68] and [70] respectively; the boronlike and carbonlike resonance lines are labeled as B and C respectively.

difficult. However, by including the resonance line, w, in the heliumlike system,  $(1s2p_{3/2})_1 \rightarrow (1s^2)_0$ , as well as the Lyman- $\alpha_1$  line,  $(2p_{3/2})_{3/2} \rightarrow (1s)_{1/2}$ , in the hydrogenlike charge state in the determination of the calibration curve, the uncertainty can be reduced. Thus, like the measurement in section 5.1.1, the measured transition energies are referenced, in part, to calculated transition energies.

The transition energies were determined by fitting the spectral lines with Gaussian fitting functions. The list of measured transition energies, compared to the calculations of the transition energies done with the Flexible Atomic Code [64], are shown in Table 5.2. The measurement shows that overall the MCDF calculations of the Flexible Atomic Code are quite good in predicting the energies of high-Z highly charged ions. For most transitions the agreement between theory and experiment is roughly 5 eV.

### 5.3 Summary and Conclusion

The results from the praseodymium measurements are fantastic. These are the first measurements of its kind where the K-shell x-ray emission spectrum of such a high-Z highly charged ion has been this well resolved. It is important to realize that the results presented here are just the first attempts to use calorimeters for high-energy work. The measurements were able to, for the first time, make determinations of the energy of K-shell transitions from lower charge states like lithium and berylliumlike ions for such a high atomic number element, and have shown that MCDF calculations seem to be good to the 5 eV level.

These measurements, also, highlight the potential trap that using low-resolution



detectors presents. In the measurement with the bismuth pixel, the spectral composition is thought to be very simple with only a few lines. There is no indication that x, the  $(1s2p_{3/2})_1 \rightarrow (1s^2)_0$ , is a strong line in the spectrum. Yet, in the spectrum seen with the HgTe pixels, we see that x is quite strong. Thus measuring spectra with the highest resolution instrument is often needed, as the old adage says ‘out of sight, out of mind’.

Transition Energies of K-shell Pr

Label	Transition	Energy (eV)	
		Measurement	FAC <sup>a</sup>
Lyman- $\alpha_1$	$(2p_{3/2})_{3/2} \rightarrow (1s)_{1/2}$	ref. line <sup>b</sup>	37742.2
Lyman- $\alpha_3$	$(2s)_{1/2} \rightarrow (1s)_{1/2}$	$37129 \pm 12^d$	37129.9
Lyman- $\alpha_2$	$(2p_{1/2})_{1/2} \rightarrow (1s)_{1/2}$	$37129 \pm 12^d$	37120.0
w	$(1s2p_{3/2})_1 \rightarrow (1s^2)_0$	ref. line <sup>c</sup>	37000.2
x	$(1s2p_{3/2})_2 \rightarrow (1s^2)_0$	$36963 \pm 6$	36961.1
q	$(1s2s2p_{3/2})_{3/2} \rightarrow (1s^22s)_{1/2}$	$36878 \pm 6$	36877.3
$\beta$	$(1s2s^22p_{3/2})_1 \rightarrow (1s^22s^2)_0$	$36800 \pm 6$	36802.7
B	$(1s2s^22p_{1/2}2p_{3/2})_{3/2} \rightarrow (1s^22s^22p_{1/2})_0$	$36677 \pm 7$	36681.4
C	$(1s2s^22p_{1/2}^22p_{3/2})_1 \rightarrow (1s^22s^22p_{1/2}^2)_0$	$36545 \pm 12$	36548.3
y	$(1s2p_{1/2})_1 \rightarrow (1s^2)_0$	$36383 \pm 8$	36388.2
z	$(1s2s)_1 \rightarrow (1s^2)_0$	$36298 \pm 6$	36301.1
E16	$(1s2s^22p_{1/2})_1 \rightarrow (1s^22s^2)_0$	$36207 \pm 6$	36210.0
p	$(1s2s^2)_{1/2} \rightarrow (1s^22p_{1/2})_{1/2}$	$36088 \pm 6$	36085.8

<sup>a</sup> FAC [64]<sup>b</sup> Johnson and Soff [71]<sup>c</sup> Value from Drake [67]<sup>d</sup> blended

Table 5.2: Table of measured transition energies for K-shell praseodymium at an electron beam energy of 127 keV. The error bars are purely statistical. Measured transition energies are compared to calculations done by the Flexible Atomic Code. Good agreement is found for the measured energies and calculations.

## Chapter 6

# Transition Energy Measurement of Hydrogenlike and Heliumlike Xenon with the ECS

### 6.1 Introduction

The problem of calculating the energy levels in a hydrogenlike system is generally accepted to be completely solved. In principle, all-order calculations can be made that are accurate to the uncertainty in the size of the nucleus of the ions in question. In the heliumlike ion, the situation is more complex. The addition of the second electron means that the ‘classical’ wavefunction cannot be solved exactly like in the hydrogenlike case, and thus, approximations must be made. Because of this, there are several ways in which the heliumlike system is calculated. Beiersdorfer et al. [72] showed that there seems to be a

systematic discrepancy in the calculation for the energy levels in the heliumlike charge state. The systematic difference was seen over a wide range of lower-Z ions. The calculations that were compared in that paper, tended to be under-estimating the energy of the resonance transition.

Xenon is the perfect ion to measure with the ECS for a number of reasons. QED scales as  $Z^4$ , while the total transition energy scales as  $Z^2$ . Thus the QED effects are much stronger in xenon then, say, in iron. Yet the photon energy of K-shell transitions in xenon are still low enough so that the ECS has a sizeable quantum efficiency. This is important, as the flux of K-shell x-ray photons from EBIT is low from high-Z ions, and as such, to attain a sufficient statistical quality for a high precision measurement the detector using needs to have a high QE.

The choice of calibration of the energy scale in the spectrometer being used is an important consideration. This is because as the closer a calibration line is to the measured line the lower the uncertainty resultant from any non-linearity in the detector becomes<sup>1</sup>. The K-shell spectrum of xenon sits at approximately the same energy as the Cs  $K_\alpha$  lines produced by a  $^{133}\text{Ba}$  source, thus reducing the uncertainty from calibration.

## 6.2 Experiment

The EBIT Calorimeter Spectrometer, or ECS, as described in Section 3.6, was used to measure the K-shell spectrum from highly charged xenon ions. An electron beam of energy of 113 keV and current of 170 mA to 230 mA was used to collisionally ionize, excite,

---

<sup>1</sup>The measurement of the Pr with the XRS was affected by this uncertainty and minimizing it is best.

and trap the xenon ions in the trap region of SuperEBIT. The charge balance observed for the measurement was peaked at the heliumlike charge state with the hydrogenlike charge state second in intensity at around 20 %, and small amounts of the lithiumlike through boronlike charge states. Xenon was injected as a neutral gas via a ballistic gas injector that allowed for control of the pressure of the injected gas. The pressure of the injected xenon was kept at  $1 \cdot 10^{-8}$  Torr.

Radiation from the trap region was viewed by the ECS perpendicular to the electron beam direction and had to traverse a 1 foot air gap and two 5 mil beryllium windows to reach the microcalorimeter array. The Be windows allowed for a vacuum stand off where radioactive sources could be placed and used as calibration for the measurement. The measurement was comprised of 9 days, of which xenon data was taken for 10 hours each day and the rest of the each day used for calibration of the ECS. Figure 6.1 shows the spectrum of K-shell x-ray emission from highly charged xenon ions.

### 6.3 Calibration

The ECS is an array of calorimeters. To measure with high precision, the transition energies of xenon K-shell x-ray emission, there has to be a large enough number of counts in each spectral line so that the uncertainty in the determination of the centroids is low. However, the x-ray flux from SuperEBIT was too low to allow for a single pixel to have sufficient statistical quality to allow for a high-precision measurement, and thus, all of the spectra from the thick HgTe pixels needed to be added together.

The ECS digital signal processing unit outputs the pulse heights of the voltage

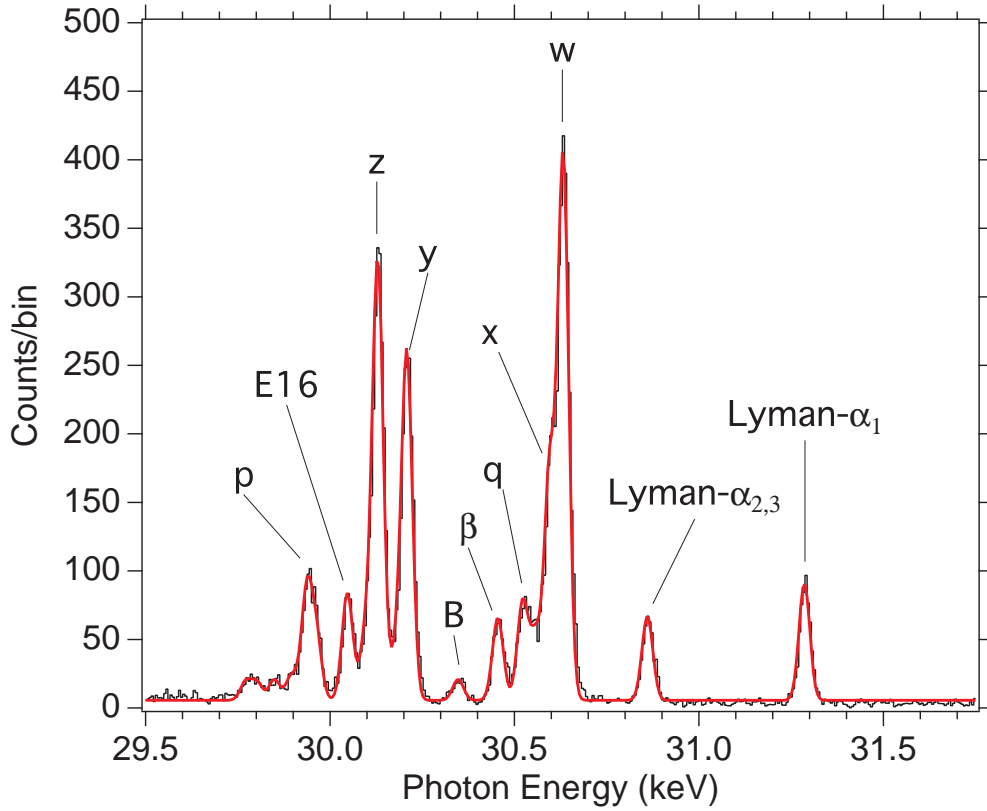


Figure 6.1: Quantum microcalorimeter spectrum of hydrogenlike through boronlike xenon taken at an electron beam energy of 114 keV. Only the strongest lines are identified. The hydrogenlike lines are labeled Lyman- $\alpha_{1-3}$ ; the heliumlike and lithiumlike lines w, q, y, and z are labeled as according to [63]; the berylliumlike lines  $\beta$  and E16 are labeled according to [68] and [70] respectively; the boronlike line is labeled as B.

pulses that are created by the absorption of an x ray in the absorber in units of volts and time tags them. A spectrum is created for each pixel by making a histogram of pulse heights for each day (over 90 individual spectra) and adding the histograms together. The histograms are added together by a computer algorithm (the same as the one used in Section 5.2.1) which sets a reference pixel and then rescales the values of the pulse heights in the other pixels to that of the reference pixel. The final result is a single spectrum from all pixels for all days.

As mentioned previously, the computer algorithm needs strong spectral lines in each histogram so that it can relate the same spectral lines in the reference histogram to the other histograms. This was accomplished by shining radioactive  $^{133}\text{Ba}$  and  $^{241}\text{Am}$  sources on the ECS calorimeter array to produce strong spectral lines in every histogram.

$^{133}\text{Ba}$  decays via electron capture to  $^{133}\text{Cs}$  and produces Cs  $K\alpha$  x rays which have energies of 30625.4 eV and 30973.1 eV respectively<sup>2</sup>. The predicted energy of the singlet transition,  $(1s2p_{3/2})_1 \rightarrow (1s^2)_0$ , in heliumlike xenon is  $\sim 30630$  eV and thus sits just above the  $K\alpha_2$  line of Cs, while the  $K\alpha_1$  line in Cs sits just above the predicted energy of the Lyman- $\alpha_2$  transition in hydrogenlike xenon. Figure 6.2 shows the spectrum obtained from the 9 days of calibration with Am and Ba.

If there was a drift in the operating temperature of the ECS, the pulse heights that the ECS was outputting would shift in value. This was seen with the XRS/EBIT to a small degree. If the temperature drifts colder, the pulse heights would be larger because the heat capacity is lowered. If the operating temperature drifts hotter, the pulse heights would be smaller because the heat capacity was raised. To account for this, the radioactive  $^{133}\text{Ba}$  source was placed in front of the ECS for 1 hour, before and after the xenon K-shell x-ray emission was recorded. If a shift in the temperature did happen, then the spectral lines from the Ba source would be shifted, and the data could be corrected accordingly. However, the centroids of the spectral lines from the  $^{133}\text{Ba}$  source, both before and after the xenon K-shell x-ray emission was observed, had the same value and thus no drifts in the operating temperature of the ECS was observed. To have calibration lines from  $^{241}\text{Am}$ , the radioactive  $^{241}\text{Am}$  source was placed in front of the ECS overnight after the completion

---

<sup>2</sup><http://physics.nist.gov/PhysRefData/ASD/index.html>

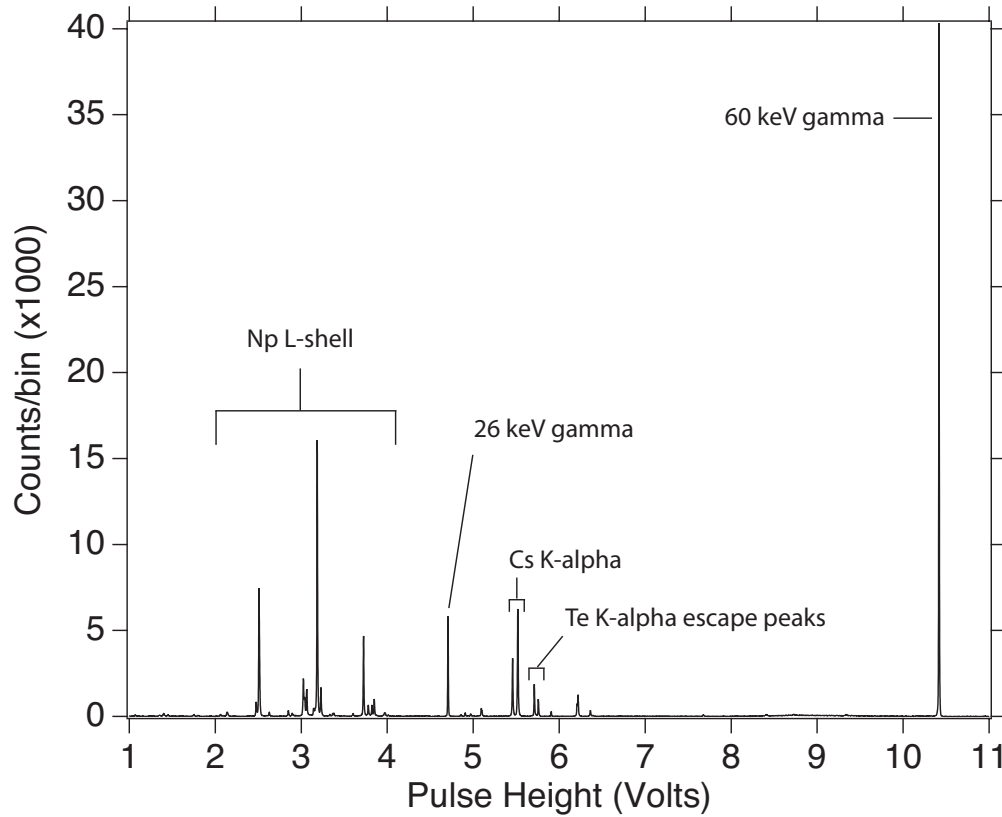


Figure 6.2: ECS spectrum of  $^{133}\text{Ba}$  and  $^{241}\text{Am}$  over 9 days. The centroids of the lines in this spectrum were used in the energy scale for the experiment.

of each measurement day. Figure 6.3 shows a representative day of time resolved events in the ECS, which shows calibration as well as data.

The energy scale that was used to determine the transition energies of the xenon K-shell x-ray emission was set using a linear fit to the centroids of the Cs  $K\alpha$  lines. As a check of the accuracy of using a linear fit in the region of interest, a quadratic fit was done with the lines from the Am and the Ba sources. The list of lines used in the quadratic fit is shown in Table 6.1. When the two fits were compared, and the energy values of the various lines measured, the discrepancy between the two fits was found to be 0.6 eV. This 0.6 eV difference in the centroids of the lines due to the type of polynomial used to set the energy



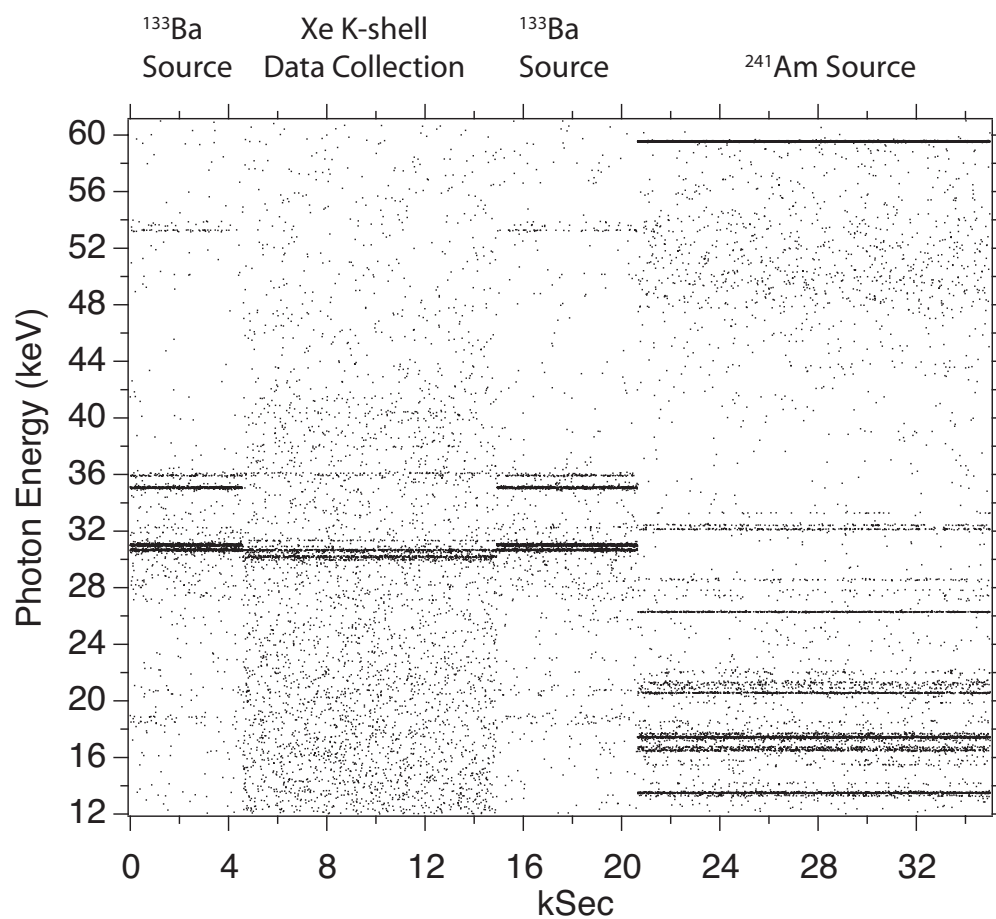


Figure 6.3: Time resolved spectrum from the ECS. The  $^{133}\text{Ba}$  source was placed in at the beginning and end of xenon data being recorded followed by the  $^{241}\text{Am}$  being placed in front.

Calibration Line Energies	
Label	Energy (eV)
$^{241}\text{Am}$ gamma	26344.8
Cs $K\alpha_2$	30625.40
Cs $K\alpha_1$	30973.13
Te $K\alpha_1$ escape peak	32068.9
Te $K\alpha_2$ escape peak	32339.5

Table 6.1: List of lines used in the determination of the energy scale. The energies of the Cs  $K\alpha$  lines and the Te  $K\alpha$  lines are referenced from the NIST online x-ray database [73], whereas, the Te  $K\alpha$  escape peaks are computed by subtracting the energy of the Te  $K\alpha$  lines from the energy of the 59.54 keV gamma-ray from  $^{241}\text{Am}$ . The value of the gamma rays emitted from  $^{241}\text{Am}$  are taken from the LBL/Lund online database of the table of isotopes [74]

scale for the measurement of xenon K-shell x-ray emission was taken as the uncertainty in the calibration. The statistical error in the determination of the centroids of the Cs  $K\alpha$  lines is 0.15 eV.

## 6.4 Power shift

In order to add the histograms of the pixels together, strong spectral features from calibration sources needed to be seen in each pixel's histogram for each day. To achieve strong calibration spectral features in each histogram, the count rate from the calibration sources need to be much higher than observed from xenon K-shell x-ray emission. This is because the low K-shell x-ray flux from SuperEBIT was too low to see a strong spectral

feature in each pixel's histogram for each day.

The temperature rise in the x-ray calorimeter spectrometer is proportional to the energy of the photon divided by the heat capacity of the calorimeter. Because the calorimeter is a device for measuring heat, the power incident on the calorimeter can affect the measured centroids of the spectral lines. If more power is incident on the array, then the heat capacity will increase (as it is dependent on the temperature) and the temperature rise of an x-ray absorption event will be lower, which results in a systematic shift in the centroids of the lines being measured.

Since the calibration lines were taken at a higher count rate (and thus power), then the value of the centroids of the Cs  $K\alpha$  lines used to set the energy scale for the measurement are shifted lower. This causes the measured values of the K-shell transitions to appear higher in energy than they actually are. Ge detectors suffer from similar pulse height shifts due to count-rate/power [75, 76]. The observed shift in the Cs  $K\alpha$  peaks is taken as a multiplicative factor,  $A$ , which is used to relate the centroid of the Cs  $K\alpha$  peak under high power conditions versus low power conditions. This is written as,

$$V_{new} = A \times V_{old}, \quad (6.1)$$

where  $V_{new}$  is the centroid of the Cs  $K\alpha$  peak under the low count-rate setting,  $V_{old}$  is centroid of the Cs  $K\alpha$  peak under the high count-rate setting, and  $A$  is the power shift coefficient. Once  $A$  is found, the value of the centroid measured under calibration conditions is multiplied by  $A$ , and a new linear energy scale is set using the shifted calibration peaks.

Under calibration conditions, the Ba source produced a power of  $\sim 50$  keV/sec/pixel

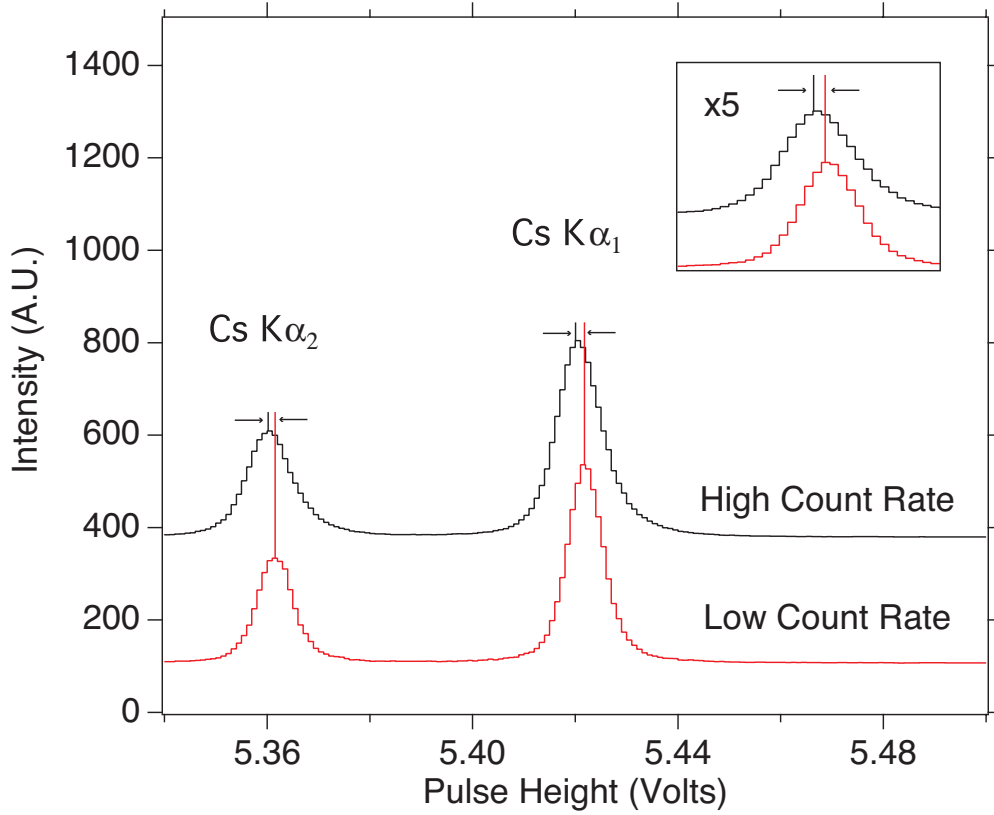


Figure 6.4: The shift in centroid of the calibration peaks for the low and high count rate settings. The difference in the FWHM resolutions of the peaks for the two different count rates can be seen. The FWHM for the peak from the high count rate is roughly 50 % larger. The high count rate is from the calibration count rate of 2 counts/sec/pixel and the low count rate is .15 counts/sec/pixel. The high count rate trace has been offset for clarity.

versus the under 3 keV/sec/pixel seen when xenon K-shell data were being recorded. In addition, the FWHM resolution of the calorimeter is dependent on the power incident on the detector. Figure 6.4 shows the difference in the centroid and FWHM resolution of the Cs K $\alpha$  lines for the high- and low-power/count rate settings.

To measure the shift coefficient,  $A$ , the Cs K $\alpha$  x rays from the radioactive  $^{133}\text{Ba}$  calibration source were recorded under various incident power settings. The power incident on the ECS from the  $^{133}\text{Ba}$  calibration source was reduced by placing thick pieces of tanta-

lum ( $Z=73$ ), which acted as a filter, in front of the source. A hole was drilled through the Ta, and the size of the hole through the filter was varied so as to reduce the emission solid angle of the radioactive source. Figure 6.5 shows the set of data points where the shift in the centroid is plotted as a function of the power.

To do the measurement, first, the unshielded source was placed in front of the ECS, for roughly 4 hours. Then a filter with a certain sized hole would be placed in front of the source to reduce the amount of x rays incident on the ECS. The data for the filter would accumulate until the number of counts in the Cs  $K\alpha_1$  line was roughly equal to the number of counts seen in the Cs  $K\alpha_1$  for the unshielded case. The power shift coefficient was determined by dividing the value of the centroid obtained for the shielded case by the value of the centroid obtained for the unshielded case. The uncertainty in the determination of the power shift coefficient is the quadrature sum of the statistical errors for the determination of the centroids of the lines for the shielded case and the unshielded case.

The FWHM of the ECS is also a function of the power incident on the array. It was found that for low incident power, the measured FWHM resolution of the Cs lines was roughly 45 eV. This is much larger than the  $\sim 30$  eV seen with the ECS when using a  $^{241}\text{Am}$  and fitting to the gamma rays it emits. The resolution of the Cs  $K\alpha$  lines are larger than the  $\sim 30$  eV found for the ECS, because neutral  $K\alpha$  transitions of high- $Z$  atoms have large transition rates and thus large natural line widths. Because of this, Voigt fitting functions were used to determine the centroids of the Cs  $K\alpha$  lines. The error in determination of the FWHM was roughly 2 % and is purely statistical. Figure 6.6 shows the set of data points where the FWHM resolution is plotted versus the incident power from the radioactive  $^{133}\text{Ba}$

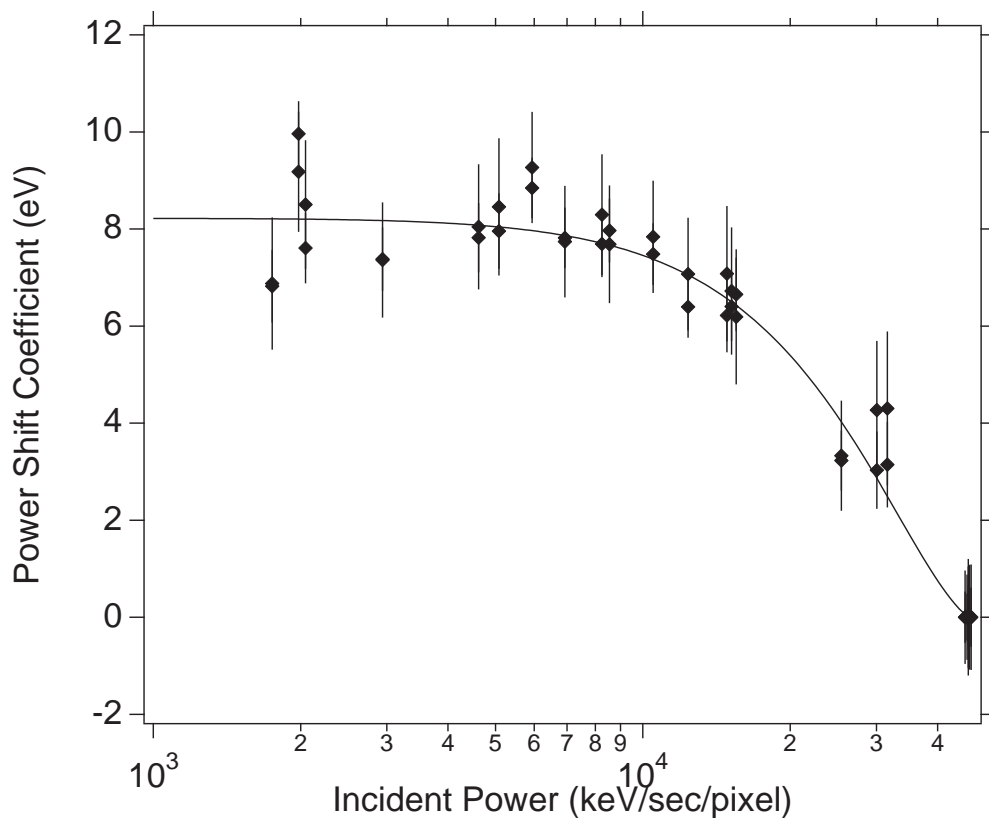


Figure 6.5: The power shift coefficient of the Cs  $K\alpha$  calibration lines as function of power. Xenon K-shell data were taken at a power under 3 keV/pixel/sec, whereas the calibration with  $^{133}\text{Ba}$  was at 50 keV/pixel/sec. Since the power shift is a multiplicative factor, the value in eV is shown as referenced from an energy of 30630 eV, which is the predicted energy of the singlet line in heliumlike xenon. The solid line shown here is a cubic fit to the data, which is approximately linear as the values of the non-linear terms are several orders of magnitude smaller. The error bars shown here are purely statistical.

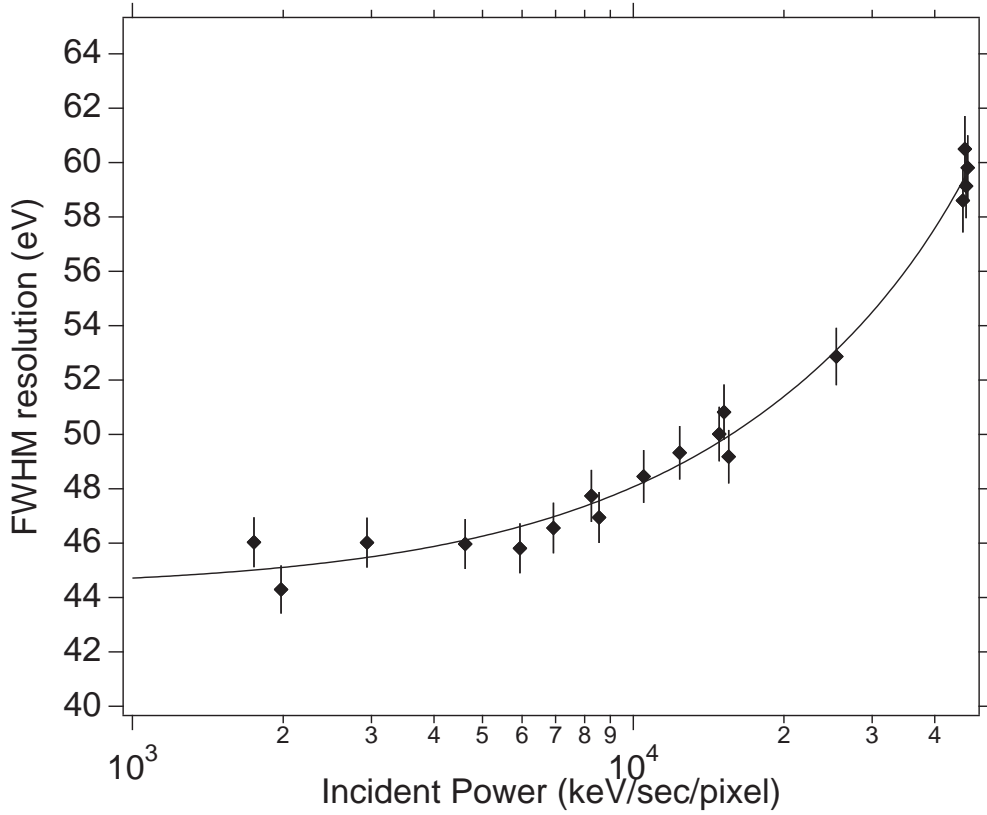


Figure 6.6: The FWHM resolution of the ECS as a function of incident power. Fit shown is a cubic fit which is approximately linear. The error bars shown here are purely statistical.

source.

For powers under 9 keV/sec/pixel, the value of the power shift coefficient is essentially flat. Since xenon K-shell data were recorded with powers under 3 keV/sec/pixel, the average value of the power shift coefficient for powers under 9 keV/sec/pixel, was used. The value of the shift for each line is dependent on the energy of the photon being measured. For the singlet line in the heliumlike system, which is approximately 30630 eV in energy, the value of the power shift is  $8.12 \pm 0.76$  eV. The error of 0.76 eV is the standard deviation around the average value of the data points for incident powers under 9 keV/sec/pixel.

Figure 6.7 shows the power coefficient for photons at 30630 eV.

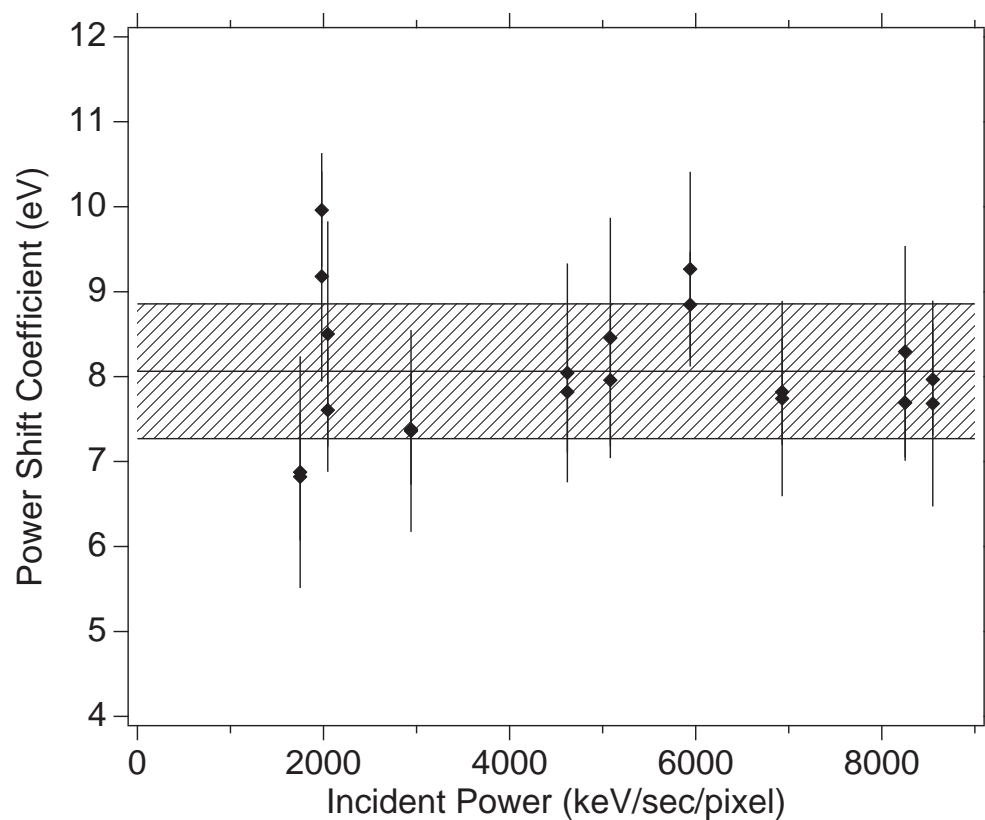


Figure 6.7: The power shift coefficient of the Cs  $K\alpha$  calibration lines as a function of power for powers under 9 keV/sec/pixel. The hashed area represents the standard deviation of the data points. The error bars shown here are purely statistical.



## 6.5 Transition Energies of Hydrogenlike Xenon

With the energy scale and power-shift determined, the energies of the atomic transitions can be assigned. The centroids of the spectral lines (and thus transition energies) were determined by applying Gaussian fitting functions to the spectrum shown in Fig. 6.1. Table 6.2 shows the results for the measured transition energies for the hydrogenlike system. The data are compared to the calculations of Johnson and Soff [71] and show excellent agreement with theory. It should be noted that this value is five times more precise than the previous value obtained by Briand et al [77].

The uncertainty in the determination of the hydrogenlike lines is the quadrature sum of the power shift uncertainty of 0.76 eV, the statistical error of 1.65 eV for Lyman- $\alpha_1$  and 2.00 eV for the blend of Lyman- $\alpha_2$  and Lyman- $\alpha_3$  line<sup>3</sup>, the uncertainty in the energy scale of 0.6 eV, and the 0.15 eV uncertainty in the determination of the Cs K $\alpha$  lines used for calibration. All uncertainties are rounded to the nearest tenth of an eV.

## 6.6 Transition Energies of Heliumlike Xenon

If progress (in terms of accuracy) is to be made in measuring the transition energies of any transition in a high-Z ion other than the Lyman- $\alpha_1$  transition, line blends (which almost always affect a measurement) must be taken into account. This is because the position of the line will shift with the energy of the blended line as well as with the excitation conditions.

An example is the measurement of the  $(1s2p_{3/2})_1 \rightarrow (1s^2)_0$  singlet line w. Line x,  $(1s2p_{3/2})_2$

---

<sup>3</sup>The statistical uncertainty in finding the centroid of a line is found by dividing the FWHM of the spectral line by the square root of the number of counts in the line. In the case of the spectrum shown in Fig. 6.1 that means dividing 34 by the square root of the number of counts.

Transition Energies of Hydrogenlike Xenon

Label	Transition	Energy (eV)	
		Measurement	Theory <sup>a</sup>
Lyman- $\alpha_1$	$(2p_{3/2})_{3/2} \rightarrow (1s)_{1/2}$	$31284.9 \pm 1.8$	31283.77
Lyman- $\alpha_3$	$(2s)_{1/2} \rightarrow (1s)_{1/2}$	$30859.3 \pm 2.0$	30863.49
Lyman- $\alpha_2$	$(2p_{1/2})_{1/2} \rightarrow (1s)_{1/2}$		30856.36

<sup>a</sup> Johnson and Soff [71]

Table 6.2: Experimental and theoretical K-shell transition energies for hydrogenlike xenon.

$\rightarrow (1s^2)_0$ , sits roughly 35 eV lower in energy than w, and as such, if the resolving power of the detector used to measure the heliumlike spectrum is not on the order of 1000, then x will blend with w.

In the paper by Briand et al. [77], a measurement of the singlet line in heliumlike xenon was presented. However the authors did not discuss any blending of the singlet line with the triplet line. As such, their error bar of 3.5 eV associated with the measured value for line w is in doubt. In the present measurement, all of the heliumlike lines are resolved from each other, and so the problem that affected the Briand et al. measurement is not relevant here<sup>4</sup>. However, because there is some emission from the lithiumlike system, two of the triplet lines, x and y, blend with lithiumlike lines. The intensities of the lithiumlike lines are estimated from the size of the lithiumlike resonance line q,  $(1s2s2p_{3/2})_{3/2} \rightarrow (1s^22s)_{1/2}$ , to be small and are estimated to only affect the measured intensities of the heliumlike system

<sup>4</sup>There is the possibility of the  $^3P_0$  level (which blends with line y) decaying to the ground state by way of the hyperfine interaction. However, it is estimated to be on the order of 1 % and is neglected in the present analysis

by roughly 0.5 eV. The line blends are as follows: line y,  $(1s2p_{1/2})_1 \rightarrow (1s^2)_0$ , blends with line r,  $(1s2s2p_{1/2})_{1/2} \rightarrow (1s^22s)_{1/2}$ ; line x blends with line s,  $(1s2s2p_{3/2})_{3/2} \rightarrow (1s^22s)_{1/2}$ .

Table 6.3 shows the experimentally determined transitions energies for heliumlike xenon, which are compared to the theories of Drake [67], Plante et al. [78], Chen et al. [79], Cheng et al. [80], and Artemyev et al. [81]. The theory of Drake uses a non-relativistic approach to solve for the wavefunctions and an approximate solution to the QED shifts, which is based on one electron QED. The other theories use all order relativistic configuration interaction methods taken from the no-pair hamiltonian from QED [82] and differ from each other in the ways in which they treat the QED corrections. Plante et al. and Chen et al. use the approach of Drake for the QED shifts, whereas Cheng et al. uses an *ab initio* approach to solve for the QED shifts to 1st order in QED, and Artemyev et al. use an *ab initio* approach to 2nd order in QED.

In comparing the calculation of the energy of the singlet line in the heliumlike system to the experimental value, we see that only the calculations by Artemyev et al. and Cheng et al., which use an *ab initio* approach to solve for the QED shifts as well as an all order fully relativistic approach to solve for the wavefunctions, agree with experiment. The 0.6 eV difference between the calculations of Artemyev et al. and Cheng et al. is due to the addition of the 2nd order QED terms which raise the energy of the ground state.

The uncertainty in the measurement of the singlet line, w, of 1.2 eV is found by adding, in quadrature, the power shift uncertainty of 0.76 eV, the statistical uncertainty of 0.67 eV, the uncertainty in the determination of the energy scale of 0.6 eV, and the 0.15 eV uncertainty in the determination of the Cs  $K\alpha$  lines used for calibration. The uncertainties

Transition Energies of Heliumlike Xenon

Label	Transition	Energy (eV)				
		Measurement	Theory			
			a	b	c	d
w	$(1s2p_{3/2})_1 \rightarrow (1s^2)_0$	$30631.2 \pm 1.2$	30630.64	30630.05	30629.68	30629.28
x	$(1s2p_{3/2})_2 \rightarrow (1s^2)_0$	$30594.5 \pm 1.7$	30594.96	30594.36	30593.93	30593.54
y	$(1s2p_{1/2})_1 \rightarrow (1s^2)_0$	$30207.1 \pm 1.4$	30206.90	30206.27	30205.87	30205.58
z	$(1s2s)_1 \rightarrow (1s^2)_0$	$30128.6 \pm 1.3$	30129.79	30129.14	30128.78	30128.40

<sup>a</sup> Cheng et al. [80] for lines y and w and Chen et al. [79] for lines z and x

<sup>b</sup> Artemyev et al.[81]

<sup>c</sup> Plante et al. [78]

<sup>d</sup> Drake [67]

Table 6.3: Experimental and theoretical transition energies of heliumlike xenon.

in the measurements of the triplet lines, x, y, and z, are found by adding the power shift uncertainty of 0.76 eV, the statistical error of 0.85 eV (for line y), 1.01 eV (for line x), and 0.76 eV (for line z), the energy scale uncertainty of 0.6 eV, the uncertainty of 0.5 eV from lithiumlike blends (only for line x and line y) in quadrature. In addition, for line z and line x there is an uncertainty of 0.3 eV and 0.8 eV, respectively, associated with the uncertainty in the fitting of lithiumlike lines to the low energy side of the lines. All uncertainties are rounded to the nearest tenth of an eV.

To find the theory with the best overall agreement with experiment, the average

absolute deviation was determined. The average absolute deviation for each theory, was calculated by taking the difference between experiment and theory for each of the heliumlike transitions, as shown in Fig. 6.8. From these average absolute differences, it is found that the calculations of Cheng et al. [79, 80] and Artemyev et al. [81] have the smallest average difference from experiment: 0.38 eV and 0.665 eV, respectively. For the calculations of Chen et al. [79], Plante et al. [78] and Drake [67] the average deviation from experiment is 0.825 eV, 0.875 eV and 1.15 eV respectively.

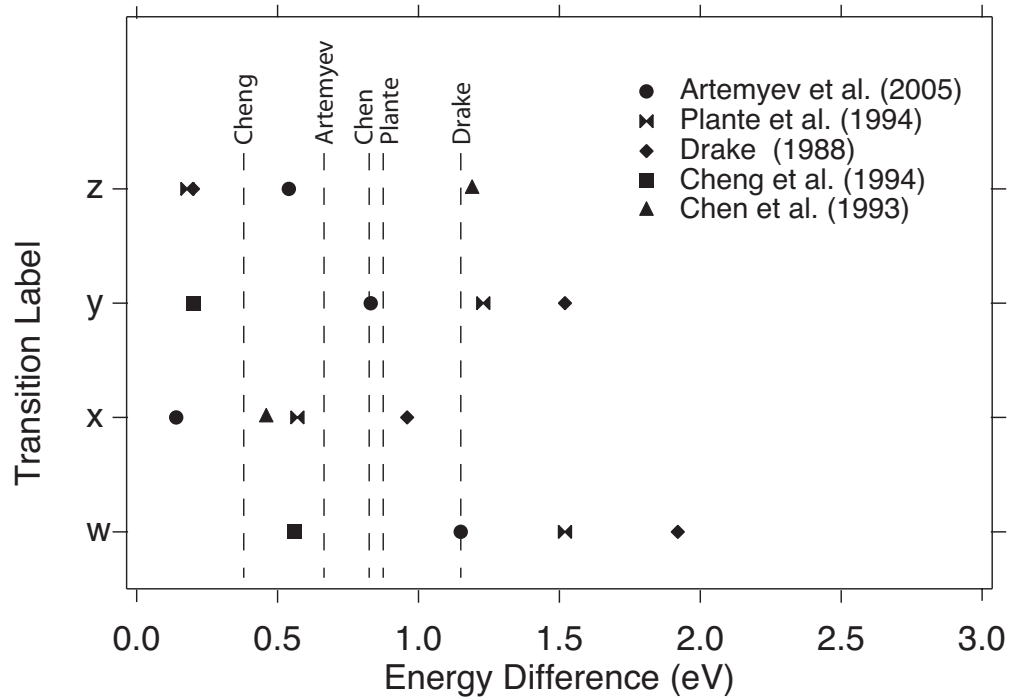


Figure 6.8: The absolute difference in the experimental transition energy and the theoretical transition energy is plotted for each transition. The different theories are labeled according to the legend. The average absolute difference from experiment for each theory is shown as the dashed line.

## 6.7 Transition Energies from Lower Charge States

In addition to the K-shell x-ray emission from hydrogenlike and heliumlike charge states, there is K-shell x-ray emission from lower charge states present. Using the same energy scale as used in the determination of the energies of the heliumlike and hydrogenlike spectral lines, the values for the resonance line in the lithiumlike charge state as well as for the resonance and intercombination line in the berylliumlike charge state have been determined. The results are shown in Table 6.4.

Transition Energies of Lithiumlike and Berylliumlike Xenon				
Label	Transition	Energy (eV)		
		Measurement	FAC <sup>a</sup>	Chen <sup>b</sup>
q	$(1s2s2p_{3/2})_{3/2} \rightarrow (1s^22s)_{1/2}$	$30522.0 \pm 2.7$	30520.40	30522.83
$\beta$	$(1s2s^22p_{3/2})_1 \rightarrow (1s^22s^2)_0$	$30454.0 \pm 2.8$	30450.68	30449.12
E16	$(1s2s^22p_{1/2})_1 \rightarrow (1s^22s^2)_0$	$30046.5 \pm 1.9$	30044.75	30042.80

<sup>a</sup> FAC [64]

<sup>b</sup> Provided by Mau Chen [69]

Table 6.4: Experimental and theoretical transition energy values for select lithiumlike and berylliumlike spectral lines.

The uncertainty for line q of 2.7 eV is a quadrature addition of the statistical uncertainty of 1.59 eV, uncertainty in the placement of line t<sup>5</sup> of 2 eV, the power shift uncertainty of 0.77 eV, the energy scale uncertainty of 0.6 eV, and the uncertainty in the

<sup>5</sup>Line t,  $(1s2s2p_{3/2})_{1/2} \rightarrow (1s^22s)_{1/2}$ , is to the high energy side of line q. Because it is smaller in intensity, assigning the position of line t was difficult. The position of line t was found to affect the position of line q by 2 eV.

determination of the centroids of the calibration lines of 0.15 eV. The uncertainty for the berylliumlike system is given by the quadrature sum of the statistical uncertainty of 1.55 eV for E16 and 1.77 eV for  $\beta$ , the power shift uncertainty of 0.75 eV, the energy scale uncertainty of 0.6 eV, the centroid determination of the calibration lines and for  $\beta$  an error from line t of 0.1 eV and for E16 an error from the placement of the u,v lithiumlike line of 0.4 eV. For line  $\beta$  there is an additional 2 eV uncertainty, that is added in quadrature, from the blending of the M2 line  $((1s2s2p_{3/2})_{5/2} \rightarrow (1s^22s)_{1/2})$  in the lithiumlike charge state. All uncertainties are rounded to the nearest tenth of an eV.

## 6.8 Summary

Given, that a first step in the use of high-QE calorimeters produced a result as awesome<sup>6</sup> as a 1.2 eV error bar, the future of such measurements are certainly bright. The ECS was used to record the K-shell x-ray spectrum of highly charged xenon. The measurement was not affected by line blending problems as previous experiments were. For the hydrogenlike system the error bar of 2 eV, is five times smaller than previously reported [77]. The measurement of the heliumlike system was able to distinguish between the theoretical treatments of the heliumlike system. It was found that theories that calculated the QED corrections in an *ab initio* way agree with experiment better than those that do not. The measurement of the lithiumlike and berylliumlike transitions showed that MCDF calculations are good to roughly 3 eV. The difference between the two MCDF calculations given in Table 6.4 are indicative of the uncertainty with MCDF codes.

---

<sup>6</sup>Yes, I wrote awesome. Yes, I was advised not too.

## Chapter 7

# Generalized Breit Interaction and Absolute K-shell Electron-Impact Excitation Cross Sections in Highly Charged Xenon Ions

When doing a measurement of electron-impact excitation (EIE) cross sections of K-shell transitions from high-Z ions (by relating the intensity of a given spectral line to the electron-impact excitation cross section), care has to be taken to properly account for the various x-ray emission processes which produce K-shell x-ray radiation and add intensity to the line being measured. If not taken into account, then the cross section that is measured will be larger than predicted, as there will be photons counted that were not formed from the electron-impact excitation process. The processes that can contribute



intensity to spectral lines are innershell ionization, radiative recombination, and charge exchange recombination<sup>1</sup>.

Innershell ionization can produce K-shell transitions by ionizing a 1s electron from an ion and leaving the ion in the excited state of the next higher charge state. An example of this, is the innershell ionization of the lithiumlike ground state,  $1s^22s$ , to produce the excited state in the heliumlike charge state,  $1s2s$ , which can radiative decay down to the ground state and produce line z.

Radiative recombination can produce K-shell transitions in heliumlike and hydrogenlike ions by capturing electrons into the  $n \geq 2$  shells of bare and hydrogenlike ions and then radiatively decaying to the 1s shell. For low-Z ions like Fe and Ni, this is a negligible amount as the RR cross sections, for capture into the  $n \geq 2$  shell, are roughly 100 times weaker than the EIE cross sections. However, because EIE cross sections scale as  $Z^{-4}$  and RR cross sections scale as  $Z^{-2}$ , the RR cross sections in high-Z ions can become comparable to the EIE cross sections.

Charge exchange recombination produces K-shell transitions of heliumlike and hydrogenlike ions in the same way as the RR process does (electrons are captured into excited levels and decay down to the 1s level). For the measurement of the EIE cross sections of hydrogenlike Fe and Ni, charge exchange was neglected because it would only amount to a few % of the EIE produced line. However, because the cross section of electron-impact excitation for K-shell transitions in highly charged xenon ions is much lower than for Fe and Ni, the rate for charge exchange is comparable to that of K-shell EIE.

---

<sup>1</sup>Dielectronic recombination can also produce K-shell transitions, however for all work in this dissertation, the electron beam energy did not fall on any DR resonance.

When taking into account the contributions to the intensity of a spectral line from innershell ionization and charge exchange, large uncertainties are involved. Thus, to measure EIE cross sections with the smallest error, it is desired to have spectra emitted from EBIT be purely from EIE processes. This is accomplished by controlling the energy of the electron beam so that no hydrogenlike ions can be created. If this happens, innershell ionization cannot take place because the energy of the electrons in the beam are not high enough to ionize a 1s electron, and K-shell x-ray emission from RR and charge exchange cannot happen because the captured electron will only be able to decay to the  $n=2$  shell as the 1s shell will be filled.

The ionization potential to remove a 1s electron from xenon is 40-42 keV (depending on the charge state). Thus to remove the uncertainty in measuring electron-impact excitation cross sections the energy of the electron beam was set at 39 keV for the measurements discussed in this chapter.

## 7.1 Test of the Generalized Breit Interaction with Highly Charged Xenon Ions

### 7.1.1 Introduction

The generalized Breit interaction<sup>2</sup> is the first QED correction to the process of a free electron scattering off of a bound electron in an atom or ion. The effect the GBI has is to modify the EIE cross section, thereby changing the observed intensity of spectral lines produced by the EIE process [40]. This effect is calculated by adding the GBI term found in

---

<sup>2</sup>see section 2.3

Section 2.3 to the distorted wave approximation method for calculating EIE cross sections described by Zhang et al. [30].

In measurements of electron-impact ionization cross sections, the theoretical calculations have agreed with experiment when the GBI was included [28, 42]. However, there have been no measurements done to verify the theoretical treatment of including the effect in EIE cross section calculations. The magnitude of the effect that the GBI has on the EIE cross section scales with the energy of the virtual photon exchanged between the free electron and the bound electron, and to maximize this effect, a high electron energy is needed. For heliumlike xenon, at an electron energy of 39 keV, the effect of the change in the line ratio of the calculated EIE cross sections for the singlet line, w, and the intercombination line, y, by including the GBI, is around 20 %.

### 7.1.2 Experiment

Heliumlike xenon was produced with a 39 keV, 200-240 mA electron beam, so as to ensure that the K-shell spectrum produced was only from EIE. The xenon, as with the experiment at higher energy (see section 6.2), was injected into the trap via a ballistic gas injector. The ECS was used to record the K-shell x-ray emission from highly charged xenon ions and viewed the SuperEBIT trap region perpendicular to the beam. Calibration was done in the same manner as for the higher-energy experiment (see section 6.3), and as such there was an air gap to allow radioactive calibration sources to be inserted in front of the ECS. Figure 7.1 shows the spectrum recorded with the ECS. The figure shows the region from the direct excitation (DE) of the K-shell spectrum of xenon to the L-shell radiative recombination part of the spectrum. The K-shell x-ray spectrum of highly charged xenon

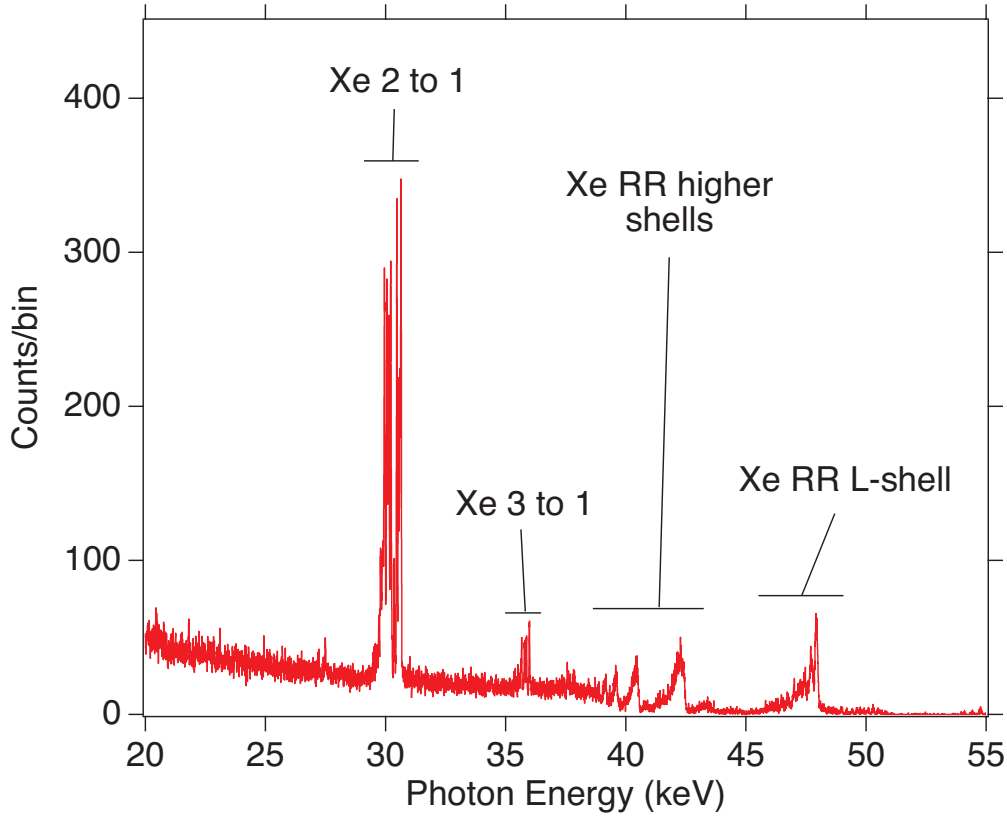


Figure 7.1: Spectrum of xenon taken with the ECS at an electron beam energy of 39 keV. Both the DE and RR parts of the spectrum can be seen, as well as the higher  $n$  to  $n=1$  transitions.

ions shown in Fig. 7.2 is produced exclusively by the EIE process.

When the GBI is included in the calculation of the cross section for electron-impact excitation in heliumlike ions, the EIE cross section for the resonance line,  $w$ , decreases compared to the ‘classically’ calculated EIE cross section, and the EIE cross section for the intercombination/forbidden transitions  $x$ ,  $y$ , and  $z$  increases compared to the ‘classically’ calculated EIE cross section. Since the emitted intensity of a direct excitation (DE) spectral line is proportional to the electron-impact excitation cross section,  $I \propto \sigma_{EIE}$ , a measurement of the intensity ratios of the spectral lines in the heliumlike charge state produces a test of

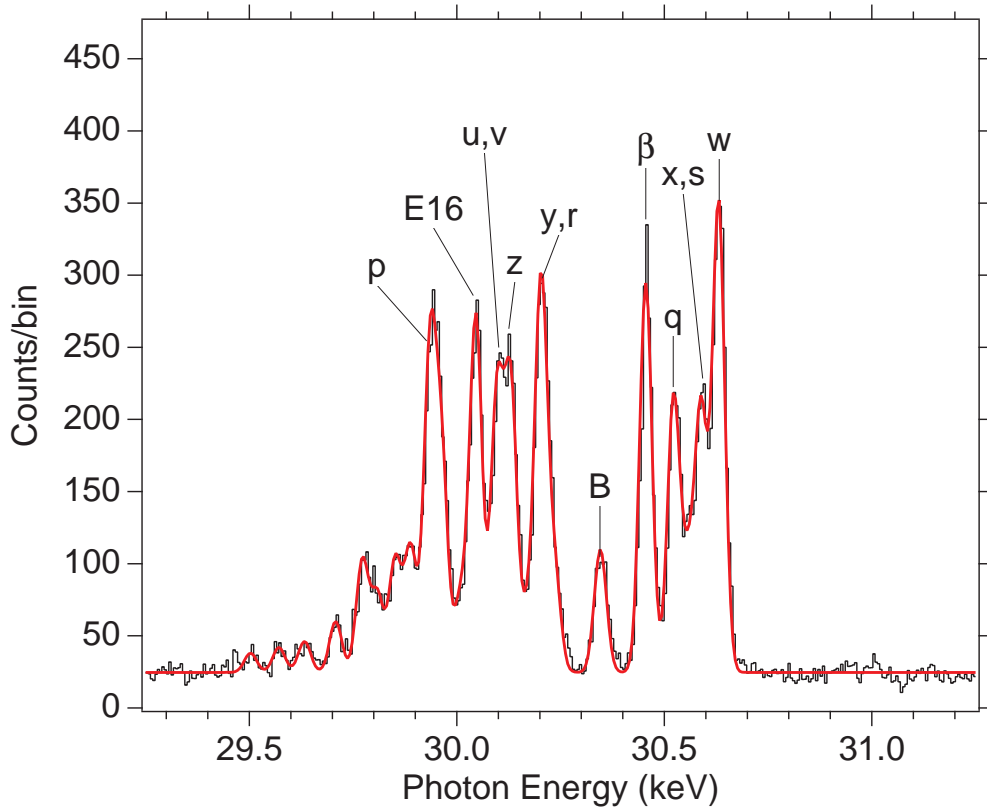


Figure 7.2: K-shell spectrum of xenon taken with the ECS at an electron beam energy of 39 keV. Only the strongest lines in the spectrum are labeled. The labeling scheme is the same as Fig. 6.1. The solid line is the fit to the spectrum.

the GBI effect by comparing the ratios of the EIE cross sections.

### 7.1.3 Measurement

With the FWHM energy resolution of 34 eV, the ECS does not have the resolving power to fully resolve the heliumlike transitions from the lithiumlike transitions. Because of this, line y from the heliumlike charge state blends with line  $r^3$ ,  $(1s2p_{1/2})_1 \rightarrow (1s^2)_0$ , from

---

<sup>3</sup>In addition to the blending of line y and line r, there is the possibility of having a contribution from the  $^3P_0$  level decaying directly to the ground state via the hyperfine interaction, because the elemental composition of xenon contains roughly 50 % odd number neutron nuclei [83]. However, a calculation done with FAC shows that the  $^3P_0$  level will have a small population in relation to line y, and that most of the population in the  $^3P_0$  level will decay to the  $^3S_1$  level and produce line z. As such, the contribution from

the lithiumlike charge state, and line x from the heliumlike charge state blends with line s,  $(1s2p_{3/2})_1 \rightarrow (1s^2)_0$ , from the lithiumlike charge state. Line w remains unblended.

Since there is blending of the lithiumlike spectral lines with the heliumlike spectral lines, the ratio of lines  $(y+r)/w$  and  $(x+s)/w$  are used to test the inclusion of the GBI in the calculation of EIE cross sections. The algebraic expression for the ratio of the spectral features becomes,

$$R = \frac{G(P_{He})C_{He}\sigma_{He} + BG(P_{Li})C_{Li}\sigma_{Li}}{G(P_w)C_w\sigma_w}, \quad (7.1)$$

where  $G(P_{He})$  denotes the polarization modification to the intensity of the heliumlike spectral lines x or y with  $G(P_w)$  for line w,  $G(P_{Li})$  denotes the polarization modification to the intensity of the lithiumlike spectral lines r or s,  $C_{He}$  denotes the cascade contribution to the intensity of the heliumlike spectral lines x or y with  $C_w$  for line w,  $C_{Li}$  denotes the cascade contribution to the intensity of the lithiumlike spectral lines r or s,  $B$  is the relative charge balance of the lithiumlike and heliumlike charge states,  $\sigma_{He}$  is the theoretical EIE cross section for the heliumlike spectral lines x or y with  $\sigma_w$  for line w, and  $\sigma_{Li}$  is the theoretical EIE cross section for the lithiumlike spectral lines.

To ascertain the experimental ratio,  $R$ , the number of counts in the spectral features labeled y,r and x,s are divided by the number of counts in the spectral line labeled w shown in Fig. 7.2. However to calculate the theoretical ratios, the cross sections for EIE with and without the GBI included, the cascade contributions, polarization of the spectral lines, and the charge balance in the trap need to be determined.

---

the  $^3P_0$  level decaying to ground and affecting the intensity of the spectral feature seen in Fig. 7.2 labeled line  $(y+r)$  is not included in the analysis.

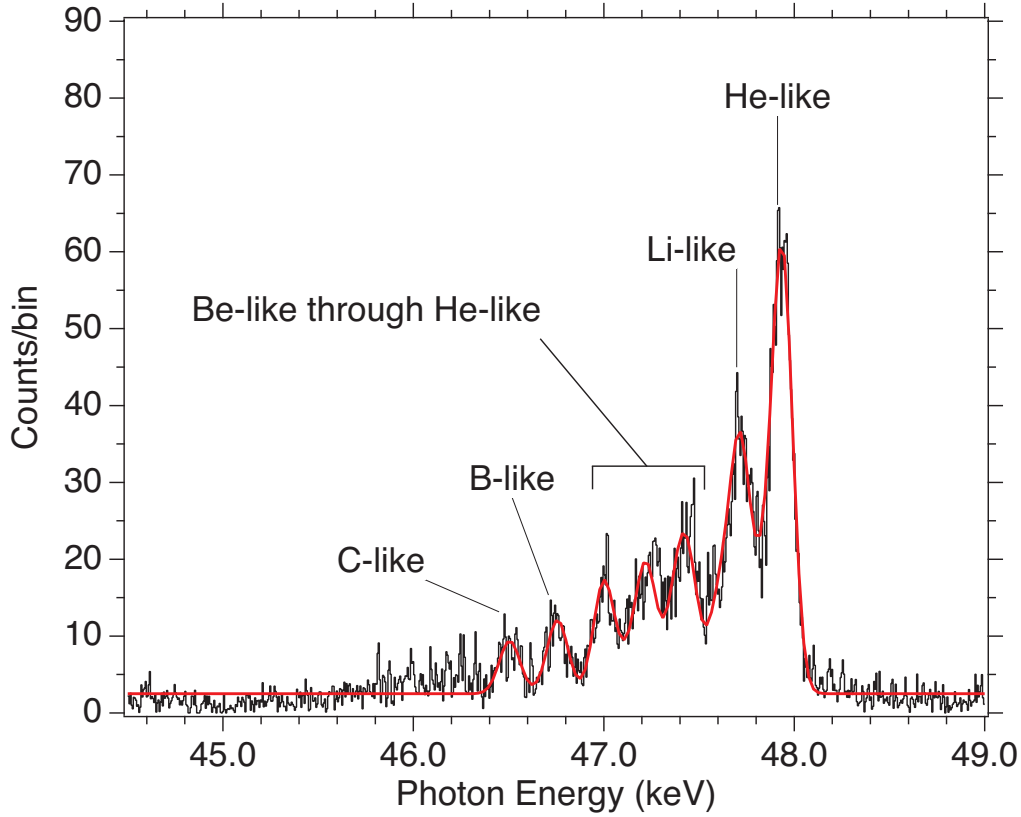


Figure 7.3: Microcalorimeter spectrum of L-shell RR radiation taken at an electron beam energy of 39 keV.

Table 7.1 shows the EIE cross sections with and without the GBI included as well as the polarization term,  $\frac{3}{3-P}$ , and cascade contributions to the spectral lines. The calculated cross sections for electron-impact excitation for heliumlike through berylliumlike xenon including the GBI were done using the method of Fontes et al. [40] and the EIE cross sections for heliumlike through berylliumlike xenon not including the GBI were done using the method Zhang et al. [30]. Both the EIE cross sections that included the GBI, and did not, were provided by Hong Lin Zhang [84]. The polarization term and the cascade contributions to the intensities of the spectral lines were provided by Ming Feng Gu [85] using FAC [64].

EIE Cross Sections, Polarization and Cascades

label	Transition	$\frac{3}{3-P}$	Cascades (%)	$\sigma_{ZS}$ (barn)	$\sigma_{GBI}$ (barn)
w	$(1s2p_{3/2})_1 \rightarrow (1s^2)_0$	1.217	8	17.02	15.91
x	$(1s2p_{3/2})_2 \rightarrow (1s^2)_0$	0.8607	27	4.798	5.528
y	$(1s2p_{1/2})_1 \rightarrow (1s^2)_0$	1.14	9	9.729	10.11
z	$(1s2s)_1 \rightarrow (1s^2)_0$	1.014	117	2.260	2.548
q	$(1s2s2p_{3/2})_{3/2} \rightarrow (1s^22s)_{1/2}$	1.103	4	10.34	9.725
s	$(1s2s2p_{3/2})_{3/2} \rightarrow (1s^22s)_{1/2}$	1.127	6	3.155	3.289
r	$(1s2s2p_{1/2})_{1/2} \rightarrow (1s^22s)_{1/2}$	1	8	3.015	2.931
$\beta$	$(1s2s^22p_{3/2})_1 \rightarrow (1s^22s^2)_0$	1.215	.5	16.50	15.44
E16	$(1s2s^22p_{1/2})_1 \rightarrow (1s^22s^2)_0$	1.136	1	9.324	9.704

Table 7.1: Calculated atomic data for selected K-shell spectral lines for heliumlike through berylliumlike xenon at an electron beam energy of 39 keV.  $\sigma_{GBI}$  is the EIE cross section including the GBI calculated using the method in Fontes et al. [40], and  $\sigma_{ZS}$  is the EIE cross section without the GBI included calculated in the method of Zhang et al. [30]. The EIE cross sections were provided by Hong Lin Zhang [84]. Calculations for the contribution from polarization and cascades for heliumlike through berylliumlike transitions were provided by Ming F. Gu [85] using the FAC code [64].



RR Cross-Sections for Xe at 39 keV Electron Energy

Charge State	Total $\sigma$	Diff $\sigma$ at $90^\circ$	Capture Level
heliumlike	14.017	1.4304	$2s_{1/2}$
heliumlike	3.9522	0.25222	$2p_{1/2}$
heliumlike	5.7036	0.36875	$2p_{3/2}$
lithiumlike	6.9672	0.71215	$2s_{1/2}$
lithiumlike	3.9463	0.25234	$2p_{1/2}$
lithiumlike	5.6946	0.3689	$2p_{3/2}$
berylliumlike	3.9054	0.25016	$2p_{1/2}$
berylliumlike	5.6327	0.36543	$2p_{3/2}$
boronlike	1.9258	0.12375	$2p_{1/2}$
boronlike	5.5515	0.3613	$2p_{3/2}$
carbonlike	5.4708	0.35734	$2p_{3/2}$

Table 7.2: Total and differential cross sections calculated for heliumlike through carbonlike xenon. Differential cross sections are calculated at  $90^\circ$ . All data is provided by J. Scofield [86].

Charge Balance	
Charge State	Charge Balance (%)
heliumlike	23.5
lithiumlike	26.1
berylliumlike	23.5
boronlike	15.6
carbonlike	11.3

Table 7.3: Charge balance of xenon ions in SuperEBIT at an electron beam energy of 39 keV.

The RR spectrum for L-shell capture, shown in Fig. 7.3, lies roughly 10 keV above the beam energy of 39 keV and is used to find the charge balance of the measurement. The charge balance was found by fitting the RR spectrum with Gaussian fitting functions constrained by the RR cross sections provided by Jim Scofield [86]. Table 7.2 shows the differential cross sections for all the levels used in the RR fit. The only free parameter in the fit to the RR was the relative intensity of each charge state as well as an overall linear term in the positions of the entire fit which was used to relate any deviation in the expected beam energy and the true beam energy. From this, it was found that the energy of the beam was in fact 38.13 keV and not 39 keV as expected. Table 7.3 shows the experimentally determined charge balance. This difference of 2% in the energy of the beam versus the energy that the RR cross sections were calculated at does not affect the charge balance determination, because all of the RR cross sections scale in the same way, and as such, the effect is canceled.

From the experimentally determined charge balance, the electron impact excitation cross sections for the heliumlike and lithiumlike charge states calculated by Hong Lin Zhang, and the polarization and cascade contributions to the intensities of the spectral lines the amount of spectral line blending between the heliumlike and lithiumlike charge states can be determined. For the line labeled y,r in Fig. 7.2, the intensity of the heliumlike spectral line y is  $\sim 75\%$  and the intensity of the lithiumlike spectral line r is  $\sim 25\%$ . For the line labeled x,s in Fig. 7.2, the intensity of the heliumlike spectral line x is  $\sim 60\%$  and the intensity of the lithiumlike spectral line s is  $\sim 40\%$ .

Line Ratios in K-shell Xe			
Measurement		Theory*	
ratio label		GBI <sup>a</sup>	no GBI <sup>b</sup>
(x+s)/w	$0.55 \pm 0.03$	$0.498 \pm 0.025$	$0.422 \pm 0.021$
(y+r)/w	$0.83 \pm 0.06$	$0.769 \pm 0.023$	$0.702 \pm 0.023$

\* error bars are from experimentally determined charge balance.

<sup>a</sup> Code of Zhang and Sampson including GBI

<sup>b</sup> Code of Zhang and Sampson

Table 7.4: Table of measured and predicted ratio of intensities of selected transitions in heliumlike and lithiumlike xenon. The theory ratios take into account polarization, cascades, and the experimentally determined charge balance.

Table 7.4 shows the comparison of the experiment with theory for the line ratios of (y+r)/w and (s+x)/w. The theoretical ratio values have error bars from the experimentally determined charge balance being used. The experimental values are purely statistical. The

values that theory predicts for the given ratios are from the code of Zhang and Sampson with the GBI included or not. When the GBI is included, the theoretical calculations agree with experiment within the error bars. But without the GBI, the results do not agree. Thus the inclusion of the GBI into the calculation of the GBI interaction is important.

#### 7.1.4 Conclusion

The Generalized Breit Interaction is most pronounced when looking at ratios of lines. That is because the GBI reduces the cross section for electron excitation for the singlet states and increases the cross section for the triplet states. In the measurement of the ratio of the intercombination lines, x and y, to the resonance line, w, it is seen that without the GBI effect added to the theoretical cross section calculations the theory numbers do not match experiment. This is the first time this has been seen in electron-impact excitation.

## 7.2 Absolute Electron-Impact Cross Sections of K-shell Transitions in Highly Charged Xenon Ions

### 7.2.1 Introduction

Electron-impact excitation (EIE) cross sections of highly charged ions are used in interpreting the spectra from laboratory-produced high-temperature plasmas<sup>4</sup>. From measurements of EIE cross sections of K-shell transitions from low-Z ions the theoretical approach of Zhang et al. [30] has been verified for K-shell transitions in hydrogenlike

---

<sup>4</sup>For a wonderful review of EIE cross section measurements please see Hui Chen's and Peter Beiersdorfer's article [32]. For the first EIE cross section measurement done with an electron beam ion trap see Marrs et al. [87].

through lithiumlike ions for Ti through Ni and a wide range of electron-impact energies [88, 62]. However there has been no work to measure the K-shell EIE cross sections with ions of  $Z$  higher than 28 to guide theory.

To recap the EIE cross section measurement procedure on SuperEBIT, the emitted intensity of a direct excitation (DE) spectral line can be written as  $I = n_e n_i \langle v_e \sigma_{EIE} \rangle$ , where  $n_e$  is the density of electrons,  $n_i$  is the density of the ions,  $v_e$  is the velocity of the electrons, and  $\sigma_{EIE}$  is the electron-impact excitation cross section. Radiative recombination (RR) is produced by the capture of an electron into a vacant atomic level. The photon that is produced has the energy of the binding energy of the atomic level plus the energy of the free electron. The mathematical expression for the intensity of a RR spectral feature has the same form as for EIE,  $I = n_e n_i \langle v_e \sigma_{RR} \rangle$ . Dividing the intensity of a given line from the EIE spectrum by that of a feature produced by RR forms a ratio of the two cross sections (RR and EIE), which leaves the EIE cross section related to the radiative recombination cross section.

### 7.2.2 Measurement

Using the same data as recorded by the ECS for the test of the GBI, the absolute cross sections for heliumlike through berylliumlike xenon can be found. The expression for the EIE cross section, taking into account the absorption of the photons in the detector at the RR and DE parts of the spectrum as shown in Fig. 7.1, the polarization modification for the spectral line in question, and cascade contributions to the spectral line, takes the form

$$\sigma_{DE} = \frac{I_{DE}}{I_{RR}} \sigma_{RR} \frac{A_{RR}}{P_{DE} C_{DE} A_{DE}}, \quad (7.2)$$

where  $\sigma_{DE}$  is the EIE cross section,  $I_{DE}$  is the number of counts in line w,  $I_{RR}$  is the number of counts in the 2s peak in the RR spectrum,  $\sigma_{RR}$  is the differential cross section at  $90^\circ$  for radiative electron capture onto the 2s shell,  $A_{RR}$  is the absorption percentage at the RR, and  $P_{DE}$ ,  $C_{DE}$  and  $A_{DE}$  are the polarization, cascade contributions and absorption percentage for the line in question, respectively.

The quantum efficiency as a function of energy of the ECS is important to know, as the ratio of the QE at the photon energy of the DE spectral lines and the RR features directly affects the measured value of the EIE cross section. As discussed in Section 3.7, the value of the QE for the ECS used is the QE calculated by the ITS code. The plot of the QE of 114  $\mu\text{m}$  thick HgTe absorbers versus photon energy is shown in Fig. 7.4. From this plot, the ratio of the absorption percentage at the 2s capture peak in the RR, which is at an energy of  $\sim 48$  keV, and the heliumlike singlet transition, which sits at an energy of 30.63 keV, is  $\sim 0.72$ .

In fitting the RR spectrum to the cross section data that was provided by Jim Scofield [86], it was found that the total beam energy was actually 38.125 keV instead of the 39 keV as inferred from the power supplies which regulate the high-voltage in SuperEBIT. Because the RR cross sections were calculated for an electron beam energy of 39 keV, the RR cross section values need to be scaled to take the difference in beam energy into account<sup>5</sup>. According to Cowan's equations 18.47 and 18.95 [89] the radiative recombination

---

<sup>5</sup>This does not affect the measurement charge balance as all of the cross sections scale in the same way.

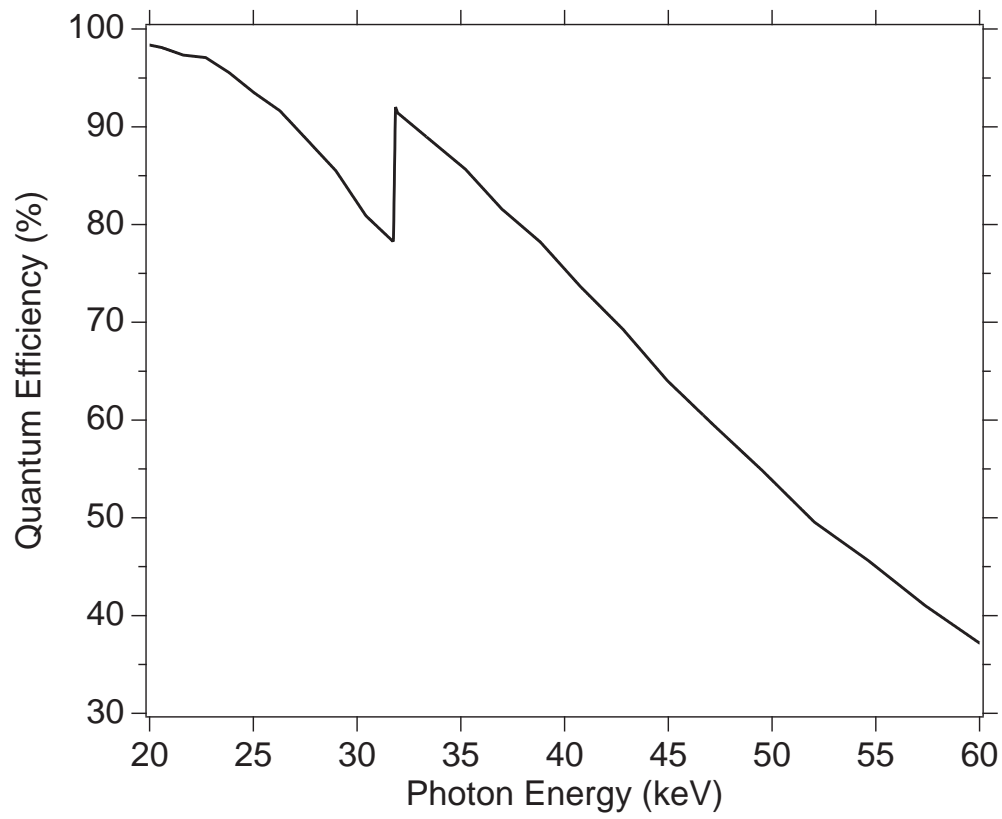


Figure 7.4: Plot of Quantum Efficiency for the ECS vs photon energy as calculated by the ITS code. Data provided by Daniel Hey [60].

cross sections scale as,

$$\frac{1}{E_e E_\gamma}, \quad (7.3)$$

where  $E_e$  is the energy of electron and  $E_\gamma$  is the energy of the photon. This energy scaling increases the calculated RR cross sections by  $\sim 4$  %.

### **Line w and Line y**

With the absorption percentages as well as the cascade contributions and polarizations of the lines known (seen in Table 7.1), the absolute electron-impact excitation cross sections for the spectral lines can be determined. The experimental values obtained for the EIE cross section for the heliumlike resonance line, w, and intercombination line, y, are shown in Table 7.5. The calculated values of the EIE cross sections for both lines w and y are consistent with experiment.

For the measurement of line y the contribution from the lithiumlike line r has to be taken into account. For the line labeled y,r in Fig. 7.2, the intensity of the heliumlike spectral line y is  $\sim 75$  % and the intensity of the lithiumlike spectral line r is  $\sim 25$  %. Thus the intensity of the y,r line is reduced by  $\sim 25$  % by removing the contribution of line r.

The uncertainty for the measurement of the EIE cross section of line w is dominated by the 10 % uncertainty in the QE of the ECS that stems from the spread of thicknesses of the HgTe pixels. The uncertainty in the calculations for the polarization and cascade contributions are taken at 20 %, but given the relatively small contributions they make on line w they are limited to about 5 % for polarization and 1.5 % for the cascades. The



EIE Cross Sections for Heliumlike Xenon				
Label	Transition	Measurement	Theory	
			GBI <sup>a</sup>	no GBI <sup>b</sup>
w	$(1s^2)_0 \rightarrow (1s2p_{3/2})_1$	$16.3 \pm 1.9$	15.59	16.68
y	$(1s^2)_0 \rightarrow (1s2p_{1/2})_1$	$11.2 \pm 1.5$	10.11	9.729

<sup>a</sup> Code of Zhang and Sampson including GBI

<sup>b</sup> Code of Zhang and Sampson

Table 7.5: Measured and calculated electron impact-excitation cross sections, in units of barn, for the resonance and intercombination transitions in heliumlike xenon at a beam energy of 39 keV.

statistical error for line w is 2 % and for the RR is 3 %. The uncertainty in the RR is taken as 3 %. With all of the uncertainty contributions summed together in quadrature, a total error bar of 12 % is found.

For line y, the uncertainty in the measurement of the EIE cross section is dominated by the QE of the ECS, as was the case for line w, and the uncertainty for the cascades, polarization and statistics are the same as for line w. However, there is an additional 5 % uncertainty (on top of those described above) that is added as a consequence of removing the blending with line r.

With the absolute EIE cross section for line y and line w determined, the ratio (w/y) that would be obtained if the intercombination line, y, were unblended, is determined to be  $0.69 \pm 0.06$  as shown in Table 7.6. When the ratio is calculated without the inclusion of the GBI, experiment does not agree with it. However, when the GBI is included in the

Line Ratio of y/w in Heliumlike Xenon			
Measurement		Theory*	
ratio label		GBI <sup>a</sup>	no GBI <sup>b</sup>
y/w	$.69 \pm 0.06$	0.648	0.583

\* error bars are from experimentally determined charge balance.

<sup>a</sup> Code of Zhang and Sampson including GBI

<sup>b</sup> Code of Zhang and Sampson

Table 7.6: Cross-section ratio for heliumlike charge states w and y. Ratio is based on experimentally determined cross sections. The uncertainty of 0.06 is the quadrature sum of the statistical error and the uncertainty from removing the contribution of line r from the blend with line y.

calculation of the ratio, experiment does agree. This is consistent with the results of the previous section.

## Line z

Table 7.7 shows the experimental value of the EIE cross section obtained for line z and compared to the theoretical value calculated by Hong Lin Zhang. The contributions to the intensity from cascades as well as polarization are taken into account. The theoretical value for the EIE cross section does not agree with the experimental value and is low by roughly a factor of 2, even if the GBI is included.

The uncertainty in the measurement of the EIE cross section of line z is dominated by the error associated with using calculated values for the cascade contributions of 117 % as calculated with the Flexible Atomic Code. The error in using calculated values for the

cascades is estimated as 20 % and added in quadrature with the uncertainty in statistics, polarization, RR, and QE of the ECS to give a total uncertainty on the EIE cross-section measurement of 30 %.

EIE Cross Section for Heliumlike Xenon				
		Measurement	Theory	
Label	Transition		GBI <sup>a</sup>	no GBI <sup>b</sup>
z	$(1s^2)_0 \rightarrow (1s2s_{1/2})_1$	$5.69 \pm 1.7$	2.548	2.260

<sup>a</sup> Code of Zhang and Sampson including GBI

<sup>b</sup> Code of Zhang and Sampson

Table 7.7: Measured and calculated electron impact-excitation cross section, in units of barn, for the forbidden transition in heliumlike xenon at a beam energy of 39 keV.

### Lithiumlike and Berylliumlike Transitions

The resonance line in the lithiumlike charge state, q, is unblended and following the same method as for the above transitions the absolute cross section for electron-impact excitation can be determined. The cascade contributions and polarization are similar for line q as for line w. This is not surprising given the similarity of the two transitions (line q is the lithiumlike equivalent of line w). Table 7.8 shows the measured EIE cross section as compared with theory for line q in the lithiumlike charge state of xenon.

As seen with line w and y, the theoretical values of the EIE cross section including the GBI and not including the GBI agree with the experimental value. The uncertainty in the measurement of the EIE cross section of line q is dominated by the uncertainty in the

EIE Cross Section for Lithiumlike Xenon

Label	Transition	Measurement	Theory	
			GBI <sup>a</sup>	no GBI <sup>b</sup>
q	$(1s^2 2s)_{1/2} \rightarrow (1s 2s^2 p_{3/2})_{3/2}$	$9.9 \pm 1.2$ barn	9.556	10.13

<sup>a</sup> Code of Zhang and Sampson including GBI

<sup>b</sup> Code of Zhang and Sampson

Table 7.8: Measured and calculated electron impact-excitation cross section, in units of barn, for the resonance transition in lithiumlike xenon at a beam energy of 39 keV.

QE of the ECS. The total uncertainty is a quadrature sum of the uncertainty in the RR, polarization, cascades, and statistics.

The berylliumlike charge state has two lines which have significant intensity. Those two lines are the resonance line  $\beta$ ,  $(1s 2s^2 2p_{3/2})_1 \rightarrow (1s^2 2s^2)_0$  and the intercombination line E16,  $(1s 2s^2 2p_{1/2})_1 \rightarrow (1s^2 2s^2)_0$ . E16 is unblended, however  $\beta$  blends with the M2 transition,  $(1s 2s^2 2p_{3/2})_{5/2} \rightarrow (1s^2 2s^2)_{1/2}$ , in the lithiumlike system. From the calculated cross sections, observed charge balance, and the calculations for cascades and polarization the M2 line contributes around 18 % to the intensity of the  $\beta$  line. From this, the M2 contribution to the intensity of the observed blend can be removed. Table 7.9 shows the results of the berylliumlike lines of  $\beta$  and E16 with the M2 line from the lithiumlike charge state removed.

### 7.2.3 Discussion

The calculated EIE values for the resonance and intercombination lines in helium-like and lithiumlike xenon agree well with experiment. This verifies the theory of Zhang

EIE Cross Sections for Berylliumlike Xenon

Label	Transition	Measurement	Theory	
			GBI <sup>a</sup>	no GBI <sup>b</sup>
$\beta$	$(1s^2 2s^2)_0 \rightarrow (1s 2s^2 2p_{3/2})_1$	$11.4 \pm 1.5$	15.14	16.17
E16	$(1s^2 2s^2)_0 \rightarrow (1s 2s^2 2p_{1/2})_1$	$13.4 \pm 1.6$	9.5	9.13

<sup>a</sup> Code of Zhang and Sampson including GBI

<sup>b</sup> Code of Zhang and Sampson

Table 7.9: Measured and calculated electron impact-excitation cross sections, in units of barn, for the resonance and intercombination transition in berylliumlike xenon at a beam energy of 39 keV.

et al. for calculating EIE cross sections for the resonance line and intercombination line in the heliumlike charge state and the resonance line in the lithiumlike charge state. However, the theoretical calculations of the EIE cross sections for line z in the heliumlike system as well as  $\beta$  and E16 in the berylliumlike system do not agree with experiment. There are no innershell ionization process or dielectronic recombination processes that can affect lines E16 and z, and as such, the deviation that theory has with experiment cannot be explained.

Figure 7.5 shows the experimental cross sections compared to the calculated values for line w, line y, and line z in the heliumlike system and line q in the lithiumlike system, and lines  $\beta$  and E16 in the berylliumlike system.

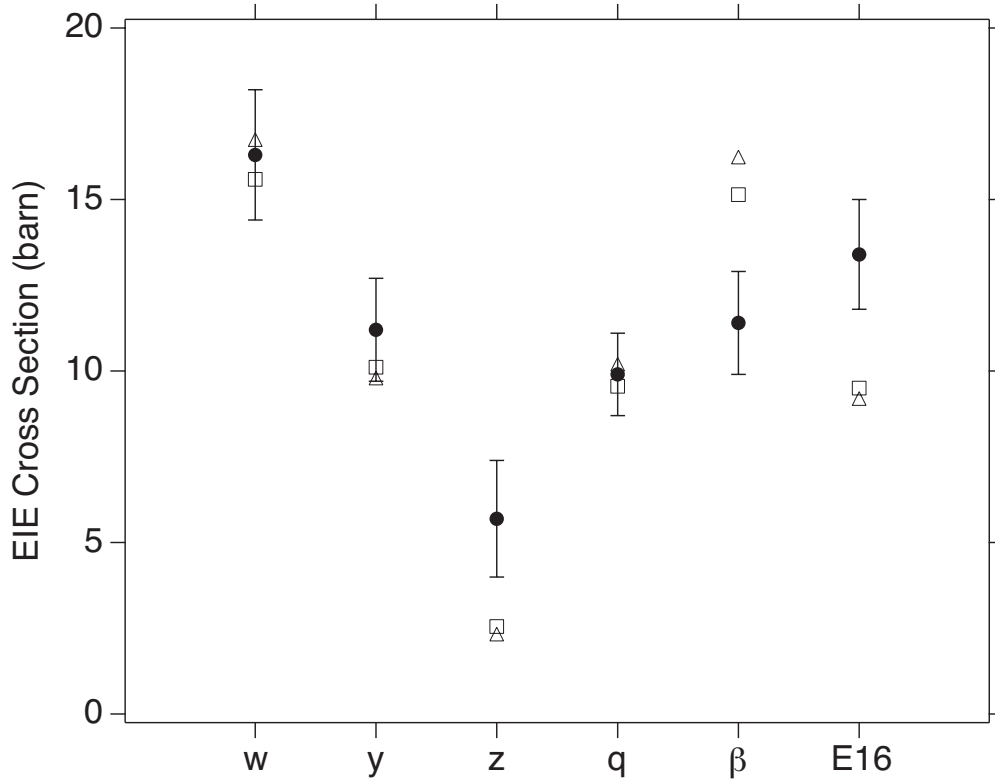


Figure 7.5: Plot of the experimental and theoretical values of EIE cross sections for K-shell transitions in heliumlike through berylliumlike xenon. Solid circles represent the experimental values, whereas open triangles represent the theoretical values without the GBI included and open squares represent the theoretical values with the GBI included.

### 7.3 Conclusion

For the first time, the generalized Breit interaction has been experimentally determined to be an important effect to include when calculating the EIE cross sections of K-shell transitions from high-Z ions. Furthermore, the distorted wave approximation method of calculating the EIE cross sections has been verified for the  $(1s2p_{3/2})_1 \rightarrow (1s^2)_0$ ,  $(1s2p_{1/2})_1 \rightarrow (1s^2)_0$ , and  $(1s2s2p_{3/2})_{3/2} \rightarrow (1s^22s)_{1/2}$ , transitions in heliumlike and lithiumlike xenon. However, the theoretical treatment of the EIE cross sections for the  $(1s2s)_1$

$\rightarrow (1s^2)_0$ ,  $(1s2s^22p_{1/2})_1 \rightarrow (1s^22s^2)_0$ , and  $(1s2s^22p_{3/2})_1 \rightarrow (1s^22s^2)_0$  transitions has been found to be incorrect for heliumlike and berylliumlike xenon. To investigate this mystery further, the isoelectronic sequence needs to be followed and the same transitions measured in higher-Z ions to check that the discrepancy seen is not a problem with calculating the EIE cross sections in xenon alone or some, as of yet unknown, artifact of the measurement.

## Chapter 8

# Summary and Future Work

This work successfully demonstrated that x-ray calorimeters can be used in detecting K-shell spectra from high-Z highly charged ions with high resolution. Calorimeters were shown to be far superior to Ge detectors, provided a large enough array of calorimeter spectrometers is used to achieve a good effective quantum efficiency. This work represents the first step towards making a measurement of the energy of the Lyman- $\alpha_1$  transition in hydrogenlike uranium with 1 eV accuracy, which would represent achieving the ‘holy grail’ in atomic spectroscopy.

For iron and nickel, the K-shell spectrum of hydrogenlike and helium ions were recorded. By using the process, by which the radiative recombination spectrum is used to ‘normalize’ the direct excitation spectrum to a measurement of the electron-impact excitation, cross sections were made at the highest electron-impact energies to date. This measurement was compared to calculations done in the distorted wave approximation method and good agreement was found.



The XRS/EBIT calorimeter array was used for recording the first high-resolution K-shell spectrum from a high-Z ion. Measurements were made using both a single bismuth absorber pixel as well as the entire array of thin  $8\text{ }\mu\text{m}$  HgTe absorber pixels. The measurement with the bismuth absorber pixel had a resolving power of roughly 5 times that of Ge detector, while the measurement using the HgTe pixels had a resolving power of a factor of 10 higher than Ge detectors. The high resolving power allowed for the spectral lines from the individual charge states to be resolved. Furthermore, the measurement with the HgTe pixels was able to test MCDF atomic structure calculations and found that, on average, the transition energies calculated by the MCDF method is good to within 5 eV.

As a stepping stone for producing high quantum-efficiency x-ray calorimeter spectrometers, thick,  $114\text{ }\mu\text{m}$  HgTe absorbers were placed on a new calorimeter spectrometer array installed at SuperEBIT. The high-energy sub-array on the ECS consists of fourteen  $114\text{ }\mu\text{m}$  thick HgTe absorber pixels and was used for recording the K-shell spectrum of highly charged xenon ions. With the ECS the K-shell transition energies of hydrogenlike through berylliumlike xenon were measured and compared to theory. For the hydrogenlike transitions no discrepancies with theory were found. For the case of transitions from heliumlike ions, it was found that theories that include QED shifts *ab initio* fit to the experimental data better than those which did not. In addition, the absolute and relative electron-impact excitation cross sections were measured. From this, it was found that for theory to recreate experimental results the generalized Breit interaction needed to be included. Also for the electric dipole transitions in heliumlike and lithiumlike xenon (line w, line y, and line q), theoretical calculations of the electron-impact excitation cross sections agree with experi-

ment. However, for the forbidden transition, line z, theory is low by roughly a factor of two. In the case of the berylliumlike system, it was found that theory is off by a large margin for both line  $\beta$  and for E16.

Future work should follow the isoelectronic sequence for heliumlike through berylliumlike ions to higher-Z elements to see if the results presented here for the GBI and for the EIE cross sections are confirmed. As the atomic number increases so should the effect of the GBI which should make the measurements easier. Ultimately a measurement of the K-shell emission of highly charged uranium should be performed.

For future detectors the resolving power of 114  $\mu\text{m}$  HgTe absorber pixels calorimeter spectrometers can be increased, if the weak thermal link from the absorber to the heat bath is increased in size. This will result in faster heat transport out of the calorimeter, which has the effect of increasing the number of frequency bins used in the determination of the pulse height of the voltage pulses resultant from an x-ray absorption event. Since the FWHM resolution is dependent on the number of ‘good’ frequency bins this is expected to result in a lower FWHM resolution.

# Bibliography

- [1] D. J. Berkeland, E. A. Hinds, and M. G. Boshier, “Precise Optical Measurement of Lamb Shifts in Atomic Hydrogen,” *Phys. Rev. Lett.* **75**, 2470–2473 (1995).
- [2] A. Huber, B. Gross, M. Weitz, and T. W. Hänsch, “High-resolution spectroscopy of the  $1S - 2S$  transition in atomic hydrogen,” *Phys. Rev. A* **59**, 1844–1851 (1999).
- [3] R. S. Van Dyck, P. B. Schwinberg, and H. G. Dehmelt, “New high-precision comparison of electron and positron  $g$  factors,” *Phys. Rev. Lett.* **59**, 26–29 (1987).
- [4] J. P. Briand, J. P. Moss, P. Indelicato, P. Chevallier, D. Girard-Vernhet, A. Chetioui, M. T. Ramos, and J. P. Desclaux, “Spectroscopy of hydrogenlike and heliumlike argon,” *Phys. Rev. A* **28**, 1413 (1983).
- [5] L. Schleinkofer, F. Bell, H.-D. Betz, G. Trollmann, and J. Rothermel, “Precision Wavelength Determination of  $2^1P_1-1^1S_0$  and  $2^3P_1-1^1S_0$  Transitions in Helium-Like Sulfur Ions,” *Phys. Scripta* **25**, 917 (1983).
- [6] R. D. Deslattes, R. Schuch, and E. Justiniano, “Application of decelerated bare nuclei to precision spectroscopy of one-electron ions,” *Phys. Rev. A* **32**, 1911 (1985).

- [7] M. Leventhal, D. E. Murnick, and H. W. Kugel, “Lamb-Shift Measurement for the  $n=2$  state of Hydrogenic  $^{16}\text{O}$ ,” *Physical Review Letters* **28**, 1609 (1972).
- [8] J. P. Briand, P. Chevallier, P. Indelicato, K. P. Ziock, and D. Dietrich, “Observation and measurement of  $n=2 \rightarrow n=1$  transitions of hydrogenlike and heliumlike uranium,” *Phys. Rev. Lett.* **65**, 2761 (1990).
- [9] T. Stöhlker, P. H. Mokler, F. Bosch, R. W. Dunford, F. Franzke, O. Klepper, C. Kozhuharov, T. Ludziejewski, F. Nolden, H. Reich, P. Rymuza, Z. Stachura, M. Steck, P. Swiat, and A. Warczak, “ $1s$  Lamb Shift in Hydrogenlike Uranium Measured on Cooled, Decelerated Ion Beams,” *Phys. Rev. Lett.* **85**, 3109–3112 (2000).
- [10] T. Stöhlker, P. H. Mokler, K. Beckert, F. Bosch, H. Eickhoff, B. Franzke, M. Jung, Y. Kandler, O. Klepper, C. Kozhuharov, R. Moshhammer, F. Nolden, H. Reich, P. Rymuza, P. Spädtke, and M. Steck, “Ground-state Lamb shift for hydrogenlike uranium measured at the ESR storage ring,” *Phys. Rev. Lett.* **71**, 2184–2187 (1993).
- [11] A. Gumberidze, T. Stöhlker, D. Banás, K. Beckert, P. Beller, H. F. Beyer, F. Bosch, S. Hagmann, C. Kozhuharov, D. Liesen, F. Nolden, X. Ma, P. H. Mokler, M. Steck, D. Sierpowski, and S. Tashenov, “Quantum electrodynamics in strong electric fields: The ground-state lamb shift in hydrogenic uranium,” *Phys. Rev. Lett.* **94**, 223001 (2005).
- [12] J. P. Briand, P. Indelicato, M. Tavernier, O. Gorceix, D. L. H. F. Beyer, B. Liu, A. Warczak, and J. P. Desclaux, “Experimental study of relativistic correlations and QED effects in heliumlike Krypton ions,” *Z. Phys. A* **318**, 1 (1986).

- [13] C. T. Munger and H. Gould, “Lamb Shift in Heliumlike Uranium ( $U90+$ ),” *Phys. Rev. Lett.* **57**, 2927–2930 (1986).
- [14] V. A. Yerokhin and V. M. Shabaev, “Two-loop self-energy correction in H-like ions,” *Phys. Rev. A* **64**, 062507 (2001).
- [15] V. A. Yerokhin, P. Indelicato, and V. M. Shabaev, “Two-Loop Self-Energy Correction in High- $Z$  Hydrogenlike Ions,” *Phys. Rev. Lett.* **91**, 073001 (2003).
- [16] M. S. Pindzola, “Parity-violation effects on the Auger-electron emission from highly charges atomic ions,” *Phys. Rev. A* **47**, 4856–4859 (1993).
- [17] A. Schäfer, G. Soff, and P. Indelicato, “Prospects for an atomic parity-violation experiment in Uranium  $90+$ ,” *Phys. Rev. A* **40**, 7362–7365 (1989).
- [18] L. N. Labzowsky, A. V. Nefiodov, G. Plunien, G. Soff, R. Marrus, and D. Liesen, “Parity-violation effect in heliumlike gadolinium and europium,” *Phys. Rev. A* **63**, 054105 (2001).
- [19] P. Beiersdorfer, H. Chen, D. B. Thorn, and E. Trabert, “Measurement of the Two-Loop Lamb Shift in Lithiumlike  $U^{89+}$ ,” *Physical Review Letters* **95**, 233003 (2005).
- [20] C. K. Stahle, D. McCammon, and K. D. Irwin, “Quantum Calorimetry,” *Physics Today* pp. 32–37 (1999).
- [21] D. McCammon, K. Barger, D. Brandl, R. Brekosky, S. Crowder, J. Gyax, R. Kelley, C. Kilbourne, M. Lindeman, F. Porter, L. Rocks, and A. Szymkowiak, “The X-

- ray Quantum Calorimeter Sounding Rocket Experiment: Improvements for the Next Flight,” *J. of Low Temp. Phys.* **151**, 715 (2008).
- [22] P. Beiersdorfer, K. R. Boyce, G. V. Brown, H. Chen, S. M. Kahn, R. L. Kelley, M. May, R. E. Olson, F. S. Porter, C. K. Stahle, and W. A. Tillotson, “Laboratory Simulation of Charge Exchange-Produced X-ray Emission from Comets,” *Science* **300**, 1558–1559 (2003).
- [23] R. L. Kelley, K. Mitsuda, C. A. Allen, P. Arsenovic, M. D. Audley, T. G. Bialas, K. R. Boyce, R. F. Boyle, S. R. Breon, G. V. Brown, J. Cottam, M. J. DiPirro, R. Fujimoto, T. Furusho, K. C. Gendreau, G. G. Gochar, O. Gonzalez, M. Hirabayashi, S. S. Holt, H. Inoue, M. Ishida, Y. Ishisaki, C. S. Jones, R. Keski-Kuha, C. A. Kilbourne, D. McCammon, U. Morita, S. H. Moseley, B. Mott, K. Narasaki, Y. Ogawara, T. Ohashi, N. Ota, J. S. Panek, F. S. Porter, A. Serlemitsos, P. J. Shirron, G. A. Sneiderman, A. E. Szymkowiak, Y. Takei, J. L. Tveekrem, S. M. Volz, M. Yamamoto, , and N. Y. Yamasaki, “The Suzaku High Resolution X-Ray Spectrometer,” *Astron. Soc. Japan* **59**, 77 (2007).
- [24] G. V. Brown, P. Beiersdorfer, H. Chen, J. H. Scofield, K. R. Boyce, R. L. Kelley, C. A. Kilbourne, F. S. Porter, M. F. Gu, S. M. Kahn, and A. E. Szymkowiak, “Energy-Dependent Excitation Cross Section Measurements of the Diagnostic Lines of Fe XVII,” *Physical Review Letters* **96**, 253201 (2006).
- [25] K. L. Wong, M. J. May, P. Beiersdorfer, K. B. Fournier, B. Wilson, G. V. Brown,

- P. Springer, P. A. Neill, and C. L. Harris, “Determination of the Charge State Distribution of a Highly Ionized Coronal Au Plasma,” *Phys. Rev. Lett.* **90**, 235001 (2003).
- [26] M. A. Levine, R. E. Marrs, J. N. Bardsley, P. Beiersdorfer, C. L. Bennett, M. H. Chen, T. Cowan, D. Dietrich, J. R. Henderson, D. A. Knapp, A. Osterheld, B. M. Penetrante, M. B. Schneider, and J. H. Scofield, “The use of an electron beam ion trap in the study of highly charged ions,” *Nuclear Instruments and Methods in Physics Research Section B: Beam Interactions with Materials and Atoms* **43**, 431–440 (1989).
- [27] D. A. Knapp, R. E. Marrs, S. R. Elliot, and et. al., “A high-energy electron beam ion trap for production of high-charge high-Z ions ,” *Nucl. Instrum. Methods A* **334** (1993).
- [28] R. E. Marrs, S. R. Elliott, and D. A. Knapp, “Production and trapping of hydrogenlike and bare uranium ions in an electron beam ion trap,” *Physical Review Letters* **72**, 4082–4085 (1994).
- [29] I. C. Percival and M. J. Seaton, “The Polarization of Atomic Line Radiation Excited by Electron Impact,” *Philos. Trans. R. Soc. London* **251**, 113 (1958).
- [30] H. L. Zhang, D. H. Sampson, and A. K. Mohanty, “Fully relativistic and quasirelativistic distorted-wave methods for calculating collision strengths for highly charged ions,” *Phys. Rev. A* **40**, 616–632 (1989).
- [31] D. L. Robbins, P. Beiersdorfer, A. Y. Faenov, T. A. Pikuz, D. B. Thorn, H. Chen, K. J. Reed, A. J. Smith, K. R. Boyce, G. V. Brown, R. L. Kelley, C. A. Kilbourne, and F. S. Porter, “Polarization measurements of the Lyman- $\alpha_1$  x-ray emission lines of

- hydrogenlike  $\text{Ar}^{17+}$  and  $\text{Fe}^{25+}$  at high electron-impact energies,” *Physical Review A* (Atomic, Molecular, and Optical Physics) **74**, 022713 (2006).
- [32] H. Chen and P. Beiersdorfer, “Electron-impact excitation cross-section measurements at EBITs from 1986 to 2006,” *Canadian Journal of Physics* **86**, 55 (2008).
- [33] J. A. Gaunt, “The Triplets of Helium,” *Proc. Roy. Soc. A* **122**, 513 (1929).
- [34] J. B. Mann and W. R. Johnson, “Breit Interaction in Multielectron Atoms,” *Phys. Rev. A* **4**, 41–51 (1971).
- [35] G. Breit, “The Effect of Retardation on the Interaction of Two Electrons,” *Phys. Rev.* **34**, 553–573 (1929).
- [36] G. Breit, “The Fine Structure of He as a Test of the Spin Interactions of Two Electrons,” *Phys. Rev.* **36**, 383–397 (1930).
- [37] G. Breit, “Dirac’s Equation and the Spin-Spin Interactions of Two Electrons,” *Phys. Rev.* **39**, 616–624 (1932).
- [38] M. Born, “Zur Quantenmechanik der Stoßvorgänge,” *Zs. Phys.* **37**, 863 (1926).
- [39] C. Møller, “Über den Stoß zweier Teilchen unter Berücksichtigung der Retardation der Kräfte,” *Zs. Phys.* **70**, 786 (1931).
- [40] C. J. Fontes, D. H. Sampson, and H. L. Zhang, “Inclusion of the generalized Breit interaction in excitation of highly charged ions by electron impact,” *Phys. Rev. A* **47**, 1009–1022 (1993).



- [41] H. L. Zhang and D. H. Sampson, “Rapid relativistic distorted-wave approach for calculating cross sections for ionization of highly charged ions,” *Phys. Rev. A* **42**, 5378–5383 (1990).
- [42] C. J. Fontes, D. H. Sampson, and H. L. Zhang, “Relativistic calculations of cross sections for ionization of  $U^{90+}$  and  $U^{91+}$  ions by electron impact,” *Phys. Rev. A* **51**, 51 (1995).
- [43] N. Nakamura, A. P. Kavanagh, H. Watanabe, H. A. Sakaue, Y. Li, D. Kato, F. J. Currell, and S. Ohtani, “Evidence for Strong Breit Interaction in Dielectronic Recombination of Highly Charged Heavy Ions,” *Physical Review Letters* **100**, 073203 (2008).
- [44] F. Mandl, *Statistical Physics* (Wiley, New York, 1971).
- [45] R. L. Kelley, M. D. Audley, K. R. Boyce, S. R. Breon, R. Fujimoto, K. C. Gendreau, S. S. Holt, Y. Ishisaki, D. McCammon, T. Mihara, K. Mitsuda, S. H. Moseley, D. B. Mott, F. S. Porter, C. K. Stahle, and A. E. Szymkowiak, “ASTRO-E high-resolution x-ray spectrometer,” in “Proc. SPIE Vol. 3765, p. 114-127, EUV, X-Ray, and Gamma-Ray Instrumentation for Astronomy X, Oswald H. Siegmund; Kathryn A. Flanagan; Eds.”, , vol. 3765 of *Presented at the Society of Photo-Optical Instrumentation Engineers (SPIE) Conference*, O. H. Siegmund and K. A. Flanagan, eds. (1999), vol. 3765 of *Presented at the Society of Photo-Optical Instrumentation Engineers (SPIE) Conference*, pp. 114–127.
- [46] C. K. Stahle, M. D. Audley, K. R. Boyce, R. P. Brekosky, R. Fujimoto, K. C. Gendreau, J. D. Gygas, Y. Ishisaki, R. L. Kelley, R. A. McClanahan, T. Mihara, K. Mitsuda, S. H.

- Moseley, D. B. Mott, F. S. Porter, C. M. Stahle, and A. E. Szymkowiak, “Design and performance of the ASTRO-E/XRS microcalorimeter array and anticoincidence detector,” in “Proc. SPIE Vol. 3765, p. 128-136, EUV, X-Ray, and Gamma-Ray Instrumentation for Astronomy X, Oswald H. Siegmund; Kathryn A. Flanagan; Eds.”, , vol. 3765 of *Presented at the Society of Photo-Optical Instrumentation Engineers (SPIE) Conference*, O. H. Siegmund and K. A. Flanagan, eds. (1999), vol. 3765 of *Presented at the Society of Photo-Optical Instrumentation Engineers (SPIE) Conference*, pp. 128–136.
- [47] R. L. Kelley, S. H. Moseley, C. K. Stahle, A. E. Szymkowiak, M. Juda, D. McCammon, and J. Zhang, “Development of microcalorimeters for high-resolution X-ray spectroscopy,” *Journal of Low Temperature Physics* **93**, 225 (1993).
- [48] A. L. Erfos, “Coulomb Gap in Disordered Systems,” *J. Phys. C* **9**, 2021–2030 (1976).
- [49] C. K. Stahle, R. P. Brekosky, S. B. Dutta, K. C. Gendreau, R. L. Kelley, D. McCammon, R. A. McClanahan, S. H. Moseley, D. B. Mott, F. S. Porter, and A. E. Szymkowiak, “The physics and the optimization of the XRS calorimeters on Astro-E,” *Nuclear Instruments and Methods in Physics Research Section A: Accelerators, Spectrometers, Detectors and Associated Equipment* **436**, 218–225 (1999).
- [50] C. Enss, ed., *Cyrogenic Particle Detection* (Springer, 2005), chap. 1 - 2, pp. 1 – 61, Topics In Applied Physics.
- [51] J. C. Mather, “Bolometer noise: nonequilibrium theory,” *Applied Optics* **21**, 1125 (1982).

- [52] A. E. Szymkowiak, R. L. Kelley, S. H. Moseley, and C. K. Stahle, “Signal processing for microcalorimeters,” *Journal of Low Temperature Physics* **93**, 281–285 (1993).
- [53] F. S. Porter, G. V. Brown, K. R. Boyce, R. L. Kelley, C. A. Kilbourne, P. Beiersdorfer, H. Chen, S. Terracol, S. M. Kahn, and A. E. Szymkowiak, “The Astro-E2 X-ray spectrometer/EBIT microcalorimeter x-ray spectrometer,” *Rev. Sci. Instrum.* **75**, 3772 (2004).
- [54] R. L. Kelley, M. D. Audley, K. R. Boyce, S. R. Breon, R. Fujimotoe, K. C. Gendreau, S. S. Holta, Y. Ishisaki, D. McCammon, T. Mihara, K. Mitsuda, S. H. Moseley, D. B. Motta, F. S. Porter, C. K. Stahle, and A. E. Szymkowiak, “The Astro-E High Resolution X-ray Spectrometer,” *SPIE Conference on EUV, X-Ray, and Gamma-Ray Instrumentation for Astronomy X Denver, Colorado* **SPIE Vol. 3765** (July 1999).
- [55] F. S. Porter, M. D. Audley, R. P. Brekosky, R. J. Derro, M. J. DiPirro, K. C. Gendreau, J. D. Gygax, R. L. Kelley, D. McCammon, A. Morrel, S. D. Murphy, R. J. Paulos, T. Pham, C. K. Stahle, A. E. Szymkowiak, and J. G. Tuttle, “Detector assembly and the ultralow-temperature refrigerator for XRS,” in “*Proc. SPIE Vol. 3765*, p. 114-127, *EUV, X-Ray, and Gamma-Ray Instrumentation for Astronomy X*, Oswald H. Siegmund; Kathryn A. Flanagan; Eds.”, , vol. 3765 of *Presented at the Society of Photo-Optical Instrumentation Engineers (SPIE) Conference*, O. H. Siegmund and K. A. Flanagan, eds. (1999), vol. 3765 of *Presented at the Society of Photo-Optical Instrumentation Engineers (SPIE) Conference*, pp. 729–740.
- [56] E. F. Feliciano, “Theory and Development of Position-Sensitive Quantum Calorime-

- ters,” Ph.D. thesis, Stanford (2001).
- [57] F. S. Porter, J. D. Gygax, R. L. Kelley, C. A. Kilbourne, P. Beiersdorfer, G. V. Brown, D. B. Thorn, and S. M. Kahn, “Performance of the EBIT Calorimeter Spectrometer,” *Review of Scientific Instruments* **79**, in press (2008).
- [58] C. A. Kilbourne, private communication (2008).
- [59] J. A. Halbleib, P. A. Kensek, T. A. Mehlhorn, G. D. Vadez, S. M. Seltzer, and M. J. Berger, “ITS: The Integrated TIGER Series of Electron/Photon Codes - Version 3.0,” *IEEE Trans. Nucl/ Sci.* **39**, 1025 (1992).
- [60] D. S. Hey, private communication (2008).
- [61] R. Bartiromo, F. Bombarda, and R. Giannella, “Spectroscopic study of nonthermal plasmas,” *Phys. Rev. A* **32**, 531–537 (1985).
- [62] K. L. Wong, P. Beiersdorfer, K. J. Reed, and D. A. Vogel, “Electron-impact excitation cross-section measurements of highly charged heliumlike and lithiumlike ions,” *Phys. Rev. A* **51**, 1214–1220 (1995).
- [63] A. H. Gabriel, “Dielectronic Satellite Spectra for Highly-charged Heliumlike Ion Lines,” *Mon. Not. R. Astr. Soc.* **160**, 99 (1972).
- [64] M. F. Gu, “The flexible atomic code,” *Can. J. Phys.* **86**, 675 (2008).
- [65] S. M. Seltzer, “Calculation of Photon Mass Energy-Transfer and Mass Energy-Absorption Coefficients,” *Rad. Res.* **136** (1993).

- [66] A. M. Niles, E. W. Magee, D. B. Thorn, G. V. Brown, H. Chen, and P. Beiersdorfer, “Laser ablation system for the injection of neutral materials into an electron beam ion trap,” *Rev. Sci. Instrum.* **77**, 10F106 (2006).
- [67] G. W. F. Drake, “Theoretical energies for the  $n = 1$  and 2 states of the helium isoelectronic sequence up to  $Z = 100$ ,” *Can. J. Phys.* **66**, 586 (1988).
- [68] M. Bitter, K. W. Hill, N. R. Sauthoff, P. C. Efthimion, E. Meservey, W. Roney, S. von Goeler, R. Horton, M. Goldman, and W. Stodiek, “Dielectronic Satellite Spectrum of Heliumlike Iron (Fe XXV),” *Phys. Rev. Lett.* **43**, 129–132 (1979).
- [69] M. Chen, private communication (2008).
- [70] P. Beiersdorfer, T. Phillips, V. L. Jacobs, K. W. Hill, M. Bitter, S. von Goeler, and S. M. Kahn, “High-resolution measurements, line identification, and spectral modeling of K-alpha transitions in Fe XVIII-Fe XXV,” *Astro. Phys. J.* **409**, 846–859 (1993).
- [71] W. R. Johnson and G. Soff, “The lamb shift in hydrogen-like atoms,  $1 \leq Z \leq 110$ ,” *Atomic Data and Nuclear Data Tables* **33**, 405–446 (1985).
- [72] P. Beiersdorfer, M. Bitter, S. von Goeler, and K. W. Hill, “Experimental study of x-ray transitions in the heliumlike isoelectronic sequence,” *Phys. Rev. A* **40**, 150 (1989).
- [73] <http://physics.nist.gov/PhysRefData/XrayTrans/Html/search.html> .
- [74] <http://nucleardata.nuclear.lu.se/nucleardata/toi/> .
- [75] K. Hansen and C. Reckleben, “Spectral Peak Shift of Si-Drift Detectors With Integrated JFETs,” *IEEE Transactions On Nuclear Science* **51**, 1283 (2004).

- [76] L. Wielopolski and R. P. Gardner, “Prediction of the pulse-height spectral distribution caused by the peak pile-up effect,” *Nucl. Instrum. and Meth.* **133**, 303 (1976).
- [77] J. P. Briand, P. Indelicato, A. Simionovici, V. S. Vicente, D. Liesen, and D. Dietrich, “Spectroscopic study of hydrogenlike and heliumlike xenon ions,” *Europhys. Lett.* **9**, 225 (1989).
- [78] D. R. Plante, W. R. Johnson, and J. Sapirstein, “Relativistic all-order many-body calculations of the  $n=1$  and  $n=2$  states of heliumlike ions,” *Phys. Rev. A* **49**, 3519–3530 (1994).
- [79] M. H. Chen, K. T. Cheng, and W. R. Johnson, “Relativistic configuration-interaction calculations of  $n=2$  triplet states of heliumlike ions,” *Phys. Rev. A* **47**, 3692–3703 (1993).
- [80] K. T. Cheng, M. H. Chen, W. R. Johnson, and J. Sapirstein, “Relativistic configuration-interaction calculations for the ground state and  $n=2$  singlet states of heliumlike ions,” *Phys. Rev. A* **50**, 247–255 (1994).
- [81] A. N. Artemyev, V. M. Shabaev, V. A. Yerokhin, G. Plunien, and G. Soff, “QED calculation of the  $n = 1$  and  $n = 2$  energy levels in He-like ions,” *Physical Review A* **71**, 062104 (2005).
- [82] J. Sapirstein, “Quantum electrodynamics of many-electron atoms,” *Phys. Scr.* **36**, 801 (1987).
- [83] A. H. W. Aten, “The Isotopic Composition of Xenon,” *Phys. Rev.* **73**, 1206–1207 (1948).

- [84] H. L. Zhang, private communication (2008).
- [85] M. F. Gu, private communication (2008).
- [86] J. Scofield, private communication (2008).
- [87] R. E. Marrs, M. A. Levine, D. A. Knapp, and J. R. Henderson, “Measurement of electron-impact excitation cross sections for very highly charged ions,” *Phys. Rev. Lett.* **60**, 1715–1718 (1988).
- [88] S. Chantrenne, P. Beiersdorfer, R. Cauble, and M. B. Schneider, “Measurement of electron impact excitation cross sections for heliumlike titanium,” *Phys. Rev. Lett.* **69**, 265–268 (1992).
- [89] R. D. Cowan, *The Theory of Atomic Structure and Spectra* (University Of California Press, 1981).
- [90] M. E. Peskin and D. V. Schroeder, *An Introduction to Quantum Field Theory* (Westview Press, 1995).
- [91] C. Itzykson and J.-B. Zuber, *Quantum Field Theory* (Dover Publications, 2006).

## Appendix A

# List of K-shell Transitions from Highly Charged Ions Used in this Thesis

This appendix gives a list for reference for the transitions used in this dissertation.

I am following the labeling designation of Gabriel [63], Bitter et al. [68], and Beiersdorfer et al. [70] for the labels used here.



Label	Transition
Lyman- $\alpha_1$	$(2p_{3/2})_{3/2} \rightarrow (1s)_{1/2}$
Lyman- $\alpha_3$	$(2s)_{1/2} \rightarrow (1s)_{1/2}$
Lyman- $\alpha_2$	$(2p_{1/2})_{1/2} \rightarrow (1s)_{1/2}$
w	$(1s2p_{3/2})_1 \rightarrow (1s^2)_0$
x	$(1s2p_{3/2})_2 \rightarrow (1s^2)_0$
s	$(1s2s2p_{3/2})_{3/2} \rightarrow (1s^22s)_{1/2}$
t	$(1s2s2p_{3/2})_{1/2} \rightarrow (1s^22s)_{1/2}$
q	$(1s2s2p_{3/2})_{3/2} \rightarrow (1s^22s)_{1/2}$
$\beta$	$(1s2s^22p_{3/2})_1 \rightarrow (1s^22s^2)_0$
M2	$(1s2s2p_{3/2})_{5/2} \rightarrow (1s^22s)_{1/2}$
B	$(1s2s^22p_{1/2}2p_{3/2})_{3/2} \rightarrow (1s^22s^22p_{1/2})_{1/2}$
C	$(1s2s^22p_{1/2}^22p_{3/2})_1 \rightarrow (1s^22s^22p_{1/2}^2)_0$
y	$(1s2p_{1/2})_1 \rightarrow (1s^2)_0$
r	$(1s2s2p_{1/2})_{1/2} \rightarrow (1s^22s)_{1/2}$
z	$(1s2s)_1 \rightarrow (1s^2)_0$
u	$(1s2s2p_{1/2})_{3/2} \rightarrow (1s^22s)_{1/2}$
v	$(1s2s2p_{1/2})_{1/2} \rightarrow (1s^22s)_{1/2}$
E16	$(1s2s^22p_{1/2})_1 \rightarrow (1s^22s^2)_0$
p	$(1s2s^2)_{1/2} \rightarrow (1s^22p_{1/2})_{1/2}$

Table A.1: List of transition used in this dissertation.

## Appendix B

# QED and Feynman Calculus

Feynman, as stated in his Nobel Lecture, developed the path integral formulation of quantum mechanics in an attempt to quantize the action-at-a-distance theory of classical electrodynamics and thus to try and avoid the problems with self energy that plagued earlier theories. Instead of using the Hamiltonian form that Heisenberg, Schödinger, and Dirac used, he went from the Lagrangian formalism. Feynman described how an infinitesimal time development operator, first used by Dirac, could be applied successively to the wavefunction to cause it to move. To find out where the particle was at any time, a path integral had to be done across all paths the particle could take. That is all QED is, a path integral formulation of quantum mechanics in which you allow particles to be created or destroyed.

To calculate processes in QED usually one starts with a Feynman diagram. A Feynman diagram is a set of lines and vertices that represent a physical process. For each type of line or vertex a mathematical expression is written down. There is usually an integration over all internal particles and at each place where particles come together,

conservation of energy and momentum is done.

To use a Feynman diagram to calculate a QED process is easy once the rules are known. It is important to note that each Feynman diagram can be done completely abstractly in the path integral formalism<sup>1</sup>. The diagram allows for a simple expression to be written down that is mathematically equivalent to the scattering amplitude that can be squared to give the scattering probability and thus be related into a cross section. For more information I recommend the text of Peskin and Schroeder [90], the text by Itzykson and Zuber [91], and Feynman's own "QED: The strange theory of light and matter" book.

The Feynman diagrams for first order Møller scattering are shown in Fig. B.1. The straight lines represent the electrons and the arrows indicate the propagation time direction. The wiggly line is a photon. However, it is a 'virtual' or 'transverse' photon, as we do not measure it.

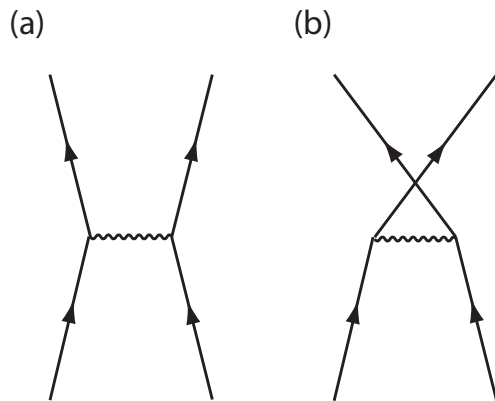


Figure B.1: Feynman diagram for the scattering process of two free electrons. Solid lines represent electrons, and wavy line is a virtual photon. (a) denotes the scattering process where the two electrons do not exchange places and (b) represents the diagram where by the two electrons exchange places. The diagram (b) is necessary as electrons are fermions.

---

<sup>1</sup>if one wanted to have an exercise in algebraic hell

To find the amplitude for this process, assign  $-ig_e\gamma^\mu$  to each vertex. For Møller scattering there are two electrons. You then assign for each external electron wavefunction: For incoming electrons (electrons pointing to a vertex) assign  $u(p_i)$  as the wavefunction; For electrons pointing away from a vertex (this represents an electron leaving the point of interaction) assign a different wavefunction  $\bar{u}(p_j)$ . For the internal ‘virtual photon’ assign the photon propagator,  $\frac{-ig_{\mu\nu}}{q^2}$ , where  $q$  is the unknown internal momentum of the photon. At each vertex apply energy and momentum conservation by using the 4 vector delta function  $(2\pi)^4\delta^4(k_1 + k_2 + k_3)$ , where  $k$  is a tensor that includes the energy and momentum. Then for each internal line integrate over the momentum  $q$ ,  $\frac{d^4q}{(2\pi)^4}$ . Take away one of the delta functions and a factor of  $-i$  and what is left is the scattering amplitude. Since in Møller scattering electrons are identical, the two diagrams shown in Fig. B.1 need to be subtracted from each other. The result of working out the Feynman diagram is then written down as,

$$\frac{g_e^2}{p_1 - p_4} [\bar{u}(4)\gamma^\mu u(1)][\bar{u}(3)\gamma_\mu u(2)] - \frac{g_e^2}{p_1 - p_3} [\bar{u}(3)\gamma^\mu u(1)][\bar{u}(4)\gamma_\mu u(2)], \quad (\text{B.1})$$

All of this is applied from the ‘top’ down meaning that you start with the electrons that are leaving. From here to calculate anything useful you would have to plug in proper wavefunctions (the bound state functions for the target atom and the free functions for the incoming electrons) and momenta and figure out all of the 4 vectors.